Université de Sherbrooke

Development of Multispectral Scatter Correction Techniques for High Resolution Positron Emission Tomography

Par

Rutao Yao

Département de Médecine Nucléaire et Radiobiologie

Thèse présentée à la Faculté de Médecine en vue de l'obtention du grade de Philosophiae Doctor (Ph.D.)

20 Mai 1997

ABSTRACT

PET images acquired with a high resolution scanner based on arrays of small discrete detectors are obtained at the cost of low sensitivity and increased detector scatter. It has been postulated that these limitations can be overcome by using multispectral acquisition whereby the energy information is registered together with the spatial coordinates of detected events. This work is an investigation of multispectral data processing methods for high resolution PET.

A photon spectral degradation model is proposed to provide theoretical support for energy-based scatter correction methods. This analytical model supplies a complete physical description of the photon propagation and detection processes in both the spatial and spectral domain. It also helps to bridge the gap between a number of heuristic scatter correction approaches and the underlying physical assumptions. In particular, it is shown that such methods as the dual energy window and multispectral frame-by-frame scatter correction techniques have intrinsic deficiencies which may be responsible for their limited success.

The potential of multispectral acquisition for developing energy-dependent scatter correction methods is severely impeded by stochastic fluctuations. Two approaches were investigated to overcome this drawback. In the first one, spectral smoothing is attempted in combination with multispectral normalization of detector efficiency and optimal data pre-processing sequence in order to allow truly energy-dependent data processing on a frame-by-frame basis. In the second approach, a global analysis of the multispectral data set is performed by the principal component analysis for reducing both the variance and

dimensionality of the multispectral data. Both approaches provide improved data for further processing.

The multispectral frame-by-frame convolution scatter correction protocol is shown to yield inferior performance to that of the convolution scatter correction in one broad window. It is concluded that the approximations made in each energy frame to implement the frame-by-frame approach accumulates errors in the final result. Consequently, the spectral smoothing technique and the implementation of the degradation model in the multiple window approach will have to be revisited to overcome this deficiency.

A data processing protocol which combines the use of both spatial and spectral information into one scatter correction method is proposed to exploit multispectral data optimally. The method consists of two consecutive steps: first, optimal noise and data dimensionality reduction, as well as partial suppression of scatter, is achieved by performing the global analysis of the multispectral data set; second, a spatial scatter correction technique, the object scatter subtraction and detector scatter restoration algorithm in this study, is used to correct for the residual scatter contribution in the output of the first step. The relevance of such a correction scheme for multispectral data is demonstrated by its superior performance as compared to conventional spatial scatter correction methods. This global scatter correction approach is promising to fulfill the need for high resolution, high sensitivity and quantitative nuclear medicine imaging.

All the techniques developed in this work are readily applicable to multiple energy window acquisition in scintigraphic or SPECT imaging.

Résumé

En tomographie d'émission par positrons (TEP), les images de très haute résolution spatiale acquises à l'aide d'une caméra basée sur de petits détecteurs discrets sont obtenues au prix d'une faible sensibilité et d'une fraction élevée d'événements diffusés dans les détecteurs. Il est proposé que ces limitations peuvent être surmontées à l'aide de l'acquisition multispectrale des événements où l'énergie des photons est enregistrée de concert avec leurs coordonnées spatiales. Cette étude porte donc sur l'établissement des outils nécessaires à l'exploitation de cette information et sur l'exploration de différentes méthodes de traitement des données multispectrales pour la TEP à haute résolution.

Un modèle de dégradation spectrale des photons est proposé pour fournir un support théorique applicable aux méthodes de correction du diffusé basées sur l'énergie. Ce modèle analytique fourni une description physique complète de la propagation de photon et des processus de la détection tant dans le domaine spatial que spectral. Il permet aussi de faire le lien entre certaines approches heuristiques de correction du diffusé et les hypothèses physiques sous-jacentes. En particulier, il est démontré que les méthodes de correction du diffusé à double fenêtre d'énergie et à fenêtres multiples sont toutes deux affligées de limites inhérentes qui expliquent probablement leur succès mitigé.

L'acquisition multispectrale offre la possibilité de développer des méthodes de correction du diffusé dépendante de l'énergie. Deux approches ont été évaluées pour solutionner ce problème. Dans la première, un lissage spectral des données est utilisé en combinaison avec l'équilibrage multispectral de l'efficacité des détecteurs, dans une séquence de pré-traitement optimale, de façon à permettre une véritable analyse dépendante de l'énergie, fenêtre par fenêtre, des données multispectrale. Dans la seconde approche, un traitement global de l'ensemble multispectral est effectué a l'aide de l'analyse des composantes principales pour à la fois réduire la variance et la dimensionalité des données. Les deux

approches fournissent un ensemble de donnés adéquates pour le traitement ultérieur du rayonnement diffusé.

Le protocole de correction du diffusé par convolution dans chaque fenêtre d'énergie conduit à des performance inférieures à une correction effectuée dans une seule fenêtre d'énergie étendue. Nous concluons que les approximations faites dans chaque fenêtre pour implanter une approche dépendante de l'énergie cumulent les erreurs dans le résultat final. En conséquence, les techniques de lissage spectral et l'implantation du modèle de dégradation dans le contexte de fenêtres d'énergie multiples devront être revus pour surmonter cette déficience.

Une méthode globale de correction du diffusé qui combine les analyses spatiale et spectrale en une seule est proposée pour exploiter au maximum les données multispectrales. Cette méthode se compose de deux étapes consécutives: premièrement, réduction optimale des dimensions, du bruit des données, de même que suppression partielle du diffusé, le tout obtenu en ne conservant que la première composante de l'analyse des composantes principales des données multispectrales; deuxièmement, un modèle spatial de correction du diffusé, l'algorithme de soustraction du diffusé-objet et de restauration du diffusé-détecteur dans cette étude, est employé pour corriger le résidu de la composante de diffusé présent dans la composante principale issue de la première étape. La pertinence de ce schéma de correction pour les données multispectrales est démontrée par un meilleur rendement que les méthodes conventionnelles d'analyse spatiale. Cette méthode globale semble une avenue prometteuse pour atteindre les objectifs de haute résolution, grande sensibilité et de quantification précise des images de médecine nucléaire.

Toutes les techniques développées dans cette étude peuvent être directement étendues aux acquisitions à fenêtres d'énergie multiples des modalités d'imagerie scintigraphique et de tomographie monophotonique (SPECT).

Acknowledgments

I wish to express my cordial gratitude to:

Dr. Roger Lecomte, for his lenient scientific spirit which allows me to experience the quintessence of research: discovering, for his stimulating instructions through numerous pleasant discussions and for his consistently honest, direct and warm personality.

Dr. Peter Msaki, for helping me making the first step on the road of research, for our fruitful collaboration and sincere friendship.

Jules Cadorette, Serge Rodrigue and Daniel Rouleau for developing the tomograph, which made this work possible, for providing the friendly work environment, for the numerous technical support and the personal help in life.

David Lapointe, Gervais Edou Mbo Edou and Catherine Pépin for teaching me and tolerating my French, and for all the delightful conversations we had.

Dr. Michael Barette, Dr. Darel Hunting, Dr. Benoit Paquette, Dr. Daniel Houde and other professors of the department, for teaching me and giving me their sympathy and kind encouragement.

The Canadian International Development Agency, for providing a studentship to support the first phase of this work.

My wife and son, I do not need a theory to explain their importance in my life.

Acronyms used

2D	2 Dimensional
3D	3 Dimensional
AAW	Average Auto-correlation Width
APD	Avalanche Photo Diode
BGO	Bismuth Germanate ($Bi_4Ge_3O_{12}$)
BW	Broad Window
CW	Conventional Window
DEW	Dual Energy Window
FA	Factor Analysis
FAMIS-TAS	Factor analysis of Medical Image Sequences - Target Apex Seeking
FBP	Filtered Back Projection
FDG	^{18}F-deoxyglucose
FOV	Field Of View
FT	Fourier Transform
FWHM	Full-Width-Half-Maximum
FWTM	Full-Width-Tenth-Maximum
HI	Holospectral Imaging
GSC	Global Scatter Correction
ILF	Ideal Low-pass Filter
LOR	Line Of Response
LSF	Line Spread Function
LSO	Ce-doped lutetium oxyorthosilicate, $Lu_2SiO_4(Ce)$
MF	Multispectral Frame-by-frame
MM	Mean Medium filter
MSPET	MultiSpectral Positron Emission Tomography

NEW	Notched Energy Window
NMSE	Normalized Mean Square Error
OFOV	Outside Field Of View
OSDR	Object scatter Subtraction and Detector scatter Restoration
PC	Prior Constrained smoothing
PCA	Principal Component Analysis
PET	Position Emission Tomography
PSF	Point Spread Function
RNS	Random-subtraction Normalization Smoothing preprocessing protocol
ROI	Region Of Interest
S/N	Signal to Noise ratio
SPECT	Single Photon Emission Computed Tomography
SRF	Scatter Response Function
SVD	Single Value Decomposition
TEW	Triple Energy Window
WPD	Weighted Projection Deviation
WS	Weighted Smoothing

List of Tables

Table 4.6. Comparing the effect of GSC and conventional scatter correction methods on resolution, sensitivity and noise characteristics. Resolution (in mm) were measured from the reconstructed images of the line source at 10 mm from the center. The line source was in a scattering media of 110 mm diameter. The Relative sensitivity (%Sen, in percent) were obtained by comparing the hot spot phantom image of each data processing protocol with that of the corresponding CW protocol. The relative standard deviation (%STD) is calculated from the second largest hot spot (H) and the background ROI (C) of the hot spot phantom image.

List of Figures

transform of the 2D energy spectrum; *ILF* filtered Fourier spectrum using v $_{cut}$=3 *window*$^{-1}$; *ILF* smoothed 2D energy spectrum obtained by inverse 2D Fourier transform.

Figure 4.1 Normalized mean-square error (*NMSE*) as a function of statistics for different smoothing algorithms. The emission and random data from the flood source measured by detector pair (5,5) were used. The high statistics emission and random spectra were taken as the expected distributions in computing *NMSE*.

Figure 4.2. Variation of spectral shape and texture of the measured (*left*) and *MM*-smoothed (*right*) emission data acquired from the flood source by detector pair (5,5) in low (*above*), intermediate (*middle*) and high statistics (*bottom*).

Figure 4.3. Same as figure 4.2 for random data.

Figure 4.4. Energy spectra acquired from a line source by detector pair (4,4) whose LOR passes through the source and detector pair (4,3) which misses the source. *Left:* Distributions obtained from high statistics measurement (24 hours) and normalized to a 20-minute acquisition time. *Right*: *PC*-smoothed distributions of the 20-minute measurement obtained using the plane source measurement as the ideal distributions.

Figure 4.5. Comparison of spectral shape and texture for selected data pre-processing sequences. The data are from low (*2.5 min*) and high statistics (*12 hours*) measurements of the flood source. *WS* smoothing was used. The high statistics RN corrected distribution (*top right*) was used as the expected distribution for computing the *NMSE* values reported in figure 4.6.

Figure 4.6. Normalized mean-square error (*NMSE*) as a function of statistics for different data pre-processing sequences. Results for the energy data measured from the flood source by detector pair (5,5) and smoothed by the *WS* technique are shown.

Figure 4.7. Relative standard deviation (*%SD*) of the projection space distributions for emission and random data acquired from the flood source in window pair (11,11) as a function of average counts/LOR for the four smoothing algorithms.

Figure 4.8. Comparison of projection space distributions from a flood source for different data pre-processing sequences. Low (*2.5 min*) and high (*12 hours*) statistics data acquired by window pair (11,11) are displayed. *ILF* smoothing was used.

Figure 4.9. Relative standard deviation (*%SD*) of the projection space data from the flood source in window pair (11,11) as a function of average counts/LOR for different pre-processing protocols.

Figure 4.10. Multispectral projection data acquired from the line source processed by RN and RNS for a low statistics (*2.5 min*) measurement. Projections are shown as a function of the window pair number $w = 13*(k-3)+(l-3)$ for $k,l \geq 3$.

Figure 4.11. Average Autocorrelation Width (*AAW*) of the line source projection distributions as a function of total counts for the RN and RNS processed data. Only windows k,l=9~14 were used to avoid *AAW* from being dominated by low energy profiles.

Figure 4.12. Same as figure 15 for Weighted Projection Deviation (*WPD*) index ($k,l \geq 3$).

Figure 4.13. Images of hot spot phantom acquired in selected energy frames and processed by the RN and RNS sequences. Windows 6 and 11 correspond to the energy ranges [252 - 293] and [462 - 503] keV, respectively.

Figure 4.14. Hot spot images comparing the effect of Multispectral Frame-by-frame Object scatter Subtraction and Detector scatter Restoration (MF OSDR) with that of Conventional Window (CW) and Broad Window (BW) modes. All protocols except the one indicated RNS used conventional

data pre-processing technique (RN). S in RNS is the ILF energy space smoothing algorithm. The CW and BW data without scatter correction (orig) are shown as references.

Figure 4.15. Profiles through the 15.8, 13.0 and 9.7 mm hot spots in the images of figure 4.14. The position of the profile is indicated in the top-left image of figure 4.14.

Figure 4.16. Comparison of contrast as a function of hot-spot diameter for images processed by the various stationary and nonstationary scatter correction protocols described in figure 4.14.

Figure 4.17. Same as figure 4.16 for the relative activity recovery factor.

Figure 4.18. The images of the first six principal components of the Multispectral hot spot phantom data obtained by Singular Value Decomposition (SVD).

Figure 4.19. Variances (or eigenvalues) of the principal components obtained by decomposing the hot spot phantom multispectral data with Singular Value Decomposition (SVD).

Figure 4.20. The transformation coefficient matrices for the first six principal components plotted as the function of 2D energy variables.

Figure 4.21. Comparing the original off-centered line source projection (BW orig) with its ϕ_{1pc} obtained by decomposing the original data by SVD. Both projections are from a incidence angle randomly selected.

Figure 4.22. Comparing the projections of the Broad Window original (BW orig) data with the first principal component (ϕ_{1pc}) of the hot spot phantom measurement. The incidence angle was selected arbitrarily.

Figure 4.23. Comparison of the effects of various spectral and spatial scatter correction protocols on hot spot phantom data. Nonstationary kernel extracted from BW (instead of ϕ_{1pc}) line source data was used for GSC. Normal BW and CW scatter kernels were used respectively for BW and CW OSDR

algorithms. The original Conventional Window (CW) and Broad Window (BW) images are shown as references. The image of the first principal component (ϕ_{1pc}) is also presented to show the effect of spectral processing by SVD.

Figure 4.24. Image profiles through the 22.7 and 13.0 mm hot spots in the images of figure 4.23.

Figure 4.25. Comparison of contrast as a function of hot-spot diameter for images processed by the various stationary and nonstationary scatter correction protocols indicated in figure 4.23.

Figure 4.26. Same as figure 4.25 for the relative activity recovery factor.

Table of Contents

Chapter 1 Introduction

In brief, this work aims to improve the image quality of high resolution PET by developing more efficient data processing, i.e. multispectral data pre-processing and scatter correction, methods.

Principles of Positron Emission Tomography (PET)

In contrast with most of the other medical imaging techniques which provide anatomical details of body organs, PET is a nuclear medicine imaging modality which provides information about the metabolic and physiological functions in living subjects such as human body or animal. Compared to Single Photon Emission Computed Tomography (SPECT) which is a competing modality, PET has higher sensitivity, higher resolution, higher quantitative accuracy (Sorensen and Phelps 1987), and most importantly, it uses isotopes of the most prevalent elements (carbon, oxygen and nitrogen) found in living systems. While there are many excellent textbooks and articles introducing this technology (Brooks *et al* 1981, Derenzo 1986a, Eriksson *et al* 1990, Koeppe and Hutchins 1992, Mandelkern 1995, Sorensen and Phelps 1987, Ter-Pogossian *et al* 1980), the principles of PET is briefly described below.

Shown in figure 1.1 is a schematic diagram of a conventional PET scanner which consists of one or more rings of detectors, data acquisition electronics, image formation and display computer system. The positron emitting isotopes required for imaging are produced by small cyclotrons and are currently synthesized into highly specific chemical agents by automated system. These biologically active compounds are localized in patients or other experimental subjects by injection or inhalation and enters the bloodstream. The

annihilation of the positron, which is emitted by the radioisotope, with an electron gives rise to a back-to-back 511 keV photon pair which are detected by the PET scanner. By sequencely relocating the detected events according to their projection direction and position, the acquired data is rebinned into a data matrix called sinogram which is used for image reconstruction. Visual display of tomographic images provides qualitative information for subjective diagnosis while modeling provides metabolic parameters from these images for quantitative diagnosis (Huang*et al* 1986).

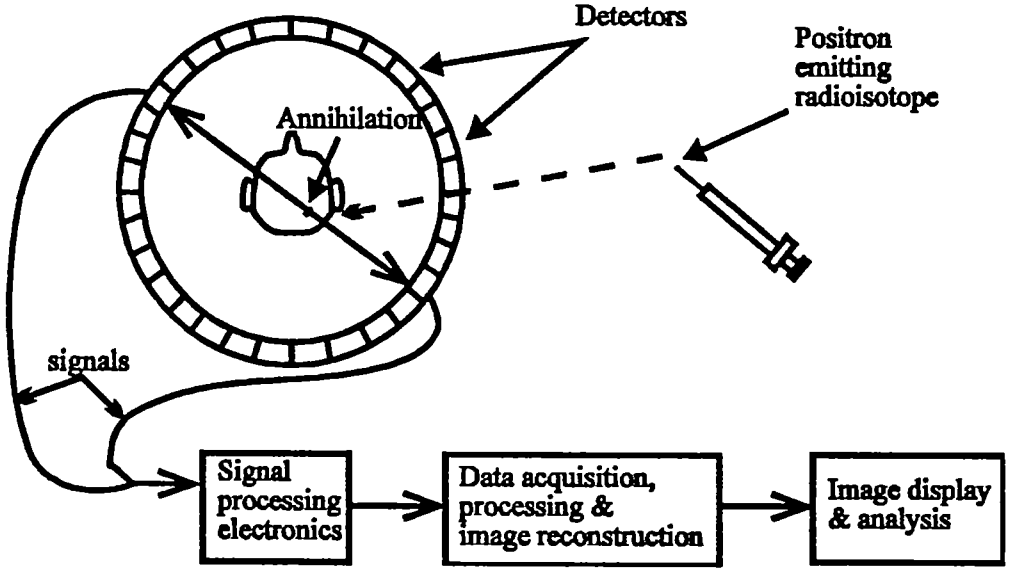

Figure 1.1. Schematic diagram showing the principle of PET scanner.

Constraint factors on PET imaging

In the last four decades, the enormous achievements in multi-disciplinary fields related with PET technology have evolved from the initial concept of forming images using annihilation γ-rays (Sweet 1951, Brownell and Sweet 1953) to clinical instruments with high resolution, high sensitivity and whole body scanning capabilities (GE Advance, Siemens CTI ECAT HR+). Nowadays, PET is being increasingly used in medical clinics and research laboratories all over the world. However, the relatively short history and

high complexity of PET make it a still developing technology. Qualitative and quantitative PET imaging are subject to many limiting factors related to image acquisition and reconstruction, such as spatial resolution, system sensitivity, attenuation, scatter, reconstruction and detector dead time. These factors affect image quality and impose constraints on PET performance (Mandelkern 1995, Mazoyer *et al* 1985, Phelps *et al* 1979, 1986, Snyder *et al* 1987, Wilson and Tsui, 1993). Although most of the factors have been studied in the past and many techniques have been implemented with the aim of minimizing or correcting for their effects, novel data processing techniques and new system design concepts need to be fully investigated to achieve best PET imaging performance. Below, six major factors influencing PET performance are described and discussed.

Spatial resolution

Increasing the spatial resolution in order to more accurately image small structures has always been a critical issue of PET scanner (Ingvar *et al* 1991, Marriott *et al* 1994). An empirical formula given by Derenzo *et al* (1993) summarizes the various components contributing to spatial resolution degradation:

$$\Gamma = 1.25\sqrt{(d/2)^2 + (0.0022D)^2 + r^2 + b^2} \qquad (1.1)$$

where, Γ is the overall reconstructed image spatial resolution, d is the scintillator crystal width, D is the scanner ring diameter with which the acollinearity of annihilation photon pair is related, r represents the full-width-half-maximum (FWHM) of the positron range and b the extra uncertainty when block decoding scheme is used. The factor 1.25 accounts for the degradation of resolution due to tomographic reconstruction.

Figure 1.2 illustrates the effects of the various components in equation (1.1). According to this figure, it is evident that the width of the scintillation crystal is the most determinant component of spatial resolution. Most importantly, this factor is directly controlled by the designer. Considering the high energy of the photons to be detected (511 keV), a high stopping power material such as Bismuth Germanate ($Bi_4Ge_3O_{12}$, BGO), with the linear attenuation coefficient of about 0.9 compared to 0.33 for Sodium Iodide (NaI), must be used to allow high detection efficiency with narrow crystals (Cho and Farukhi 1978). When the scintillators are made narrower, the penetration of obliquely incident gamma rays through the crystals becomes the main factor degrading the resolution off the center of the scanner field-of-view. So there is a certain limit for scintillator crystal width d even with the state-of-art materials.

The loss of accuracy introduced by two intrinsic physical phenomena, the full-width-at-half-maximum (FWHM) of the positron range r in tissues before annihilation (Derenzo *et al* 1986b) and the acollinearity of the annihilation gamma rays, $0.0022D$ (Debenedetti *et al* 1950), also degrade spatial resolution. The blurring due to the finite positron range can be reduced by selection of appropriate emitters. For example, the most widely used isotope ^{18}F has a relatively short range ($r = 0.54\ mm$) because of its lower positron energy. Using small detector ring diameters can reduce the effect due to acollinearity; the cost of doing so is the undermined resolution uniformity across the field of view(Carrier *et al* 1988).

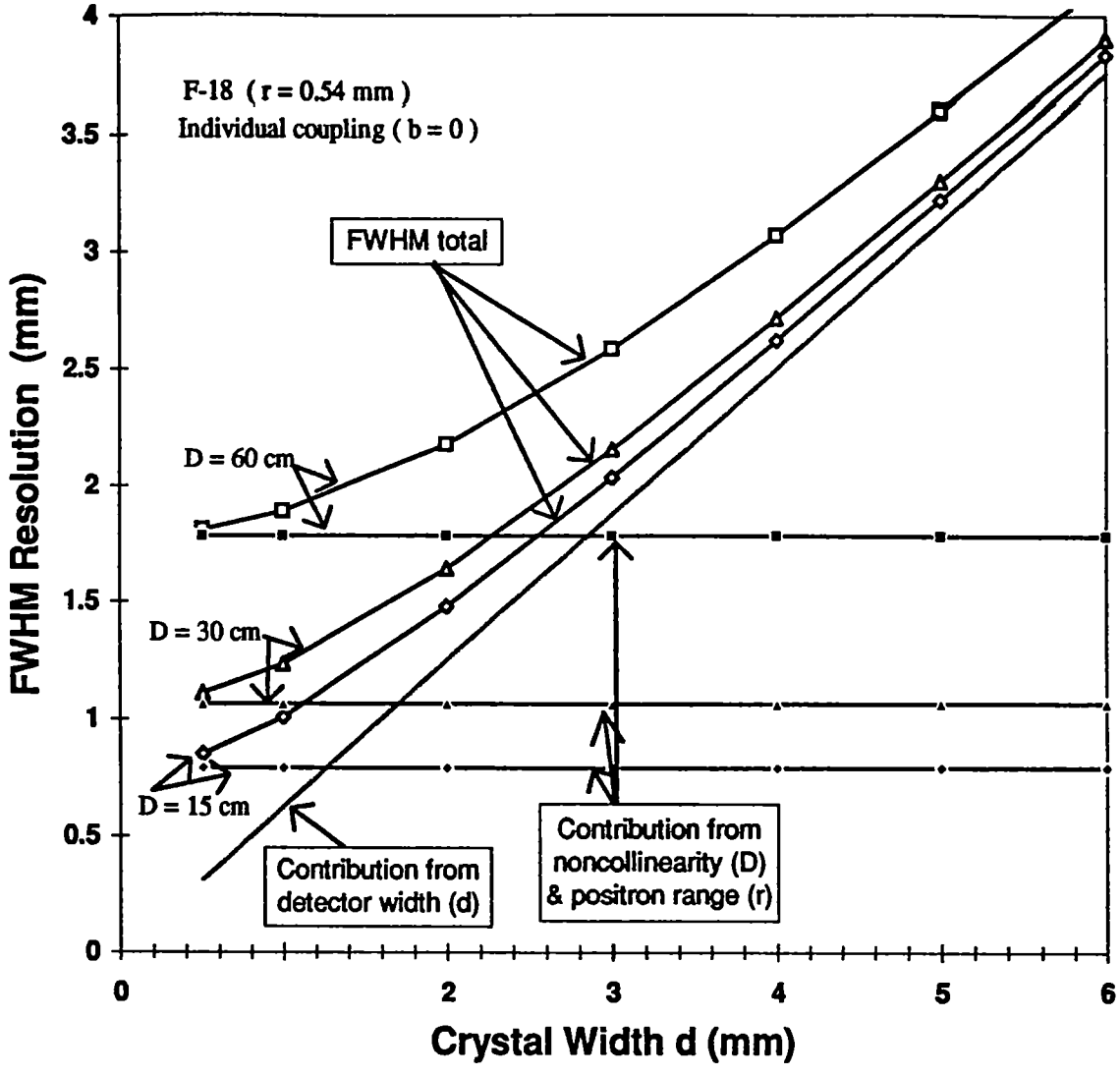

Figure 1.2. Plot of the spatial resolution as a function (equation 1.1) of crystal width (d), scanner ring diameter (D) and FWHM of the positron range (r). The contribution from detector width is 1.25*(d/2). The contribution from noncollinearity and positron range is $1.25\sqrt{(0.0022D)^2 + (r)^2}$.

System sensitivity

The ultimate goal of a PET scanner designer is to optimize the signal-to-noise ratio (S/N) in images. The signal is determined by the spatial resolution and detection efficiency of the tomograph, and by the interaction of the annihilation photons within the objects being imaged (attenuation and scatter, to be discussed in subsequent paragraphs). The primary

source of noise is the statistical variance which results from limited counts. As long acquisition times and/or strong radioactive sources are not feasible in clinical practice, increasing the scanner sensitivity is an important way to increase signal, reduce stochastic noise, and therefore maximize S/N.

As scanner sensitivity depends primarily on the detector efficiency and effective solid-angle of radiation detection, the state-of-the art PET systems employ detectors optimized for these factors (Derenzo *et al* 1993, Lecomte *et al* 1984) and acquire data in 3D mode (Michel *et al* 1991, Spinks *et al* 1992, Thompson 1988). In spite of sub-optimal light output and long photofluorescent decay time, the most common detector material used in PET scanners today is BGO, because it has the highest stopping power among available scintillator materials. However, the advent of LSO ($Lu_2SiO_4(Ce)$, Melcher and Schweitzer 1992), which has a slightly lower stopping power but about 5 times more light output, is likely to change this situation soon. As using smaller scintillators would improve spatial resolution but at the cost of detection efficiency, some trade-off has to be made to balance these two requirements. 3D acquisition significantly increases the overall efficiency as well as the fractions of the scattered events and random coincident events besides the increased system complexity and the cost of the system. These two undesired events have to be corrected correspondingly under the new situation.

Non-uniformity of detector efficiency

Detection efficiency depends on the properties of detector (crystal size, scintillation efficiency, coupling scheme, etc.) and, to some extent, on its operating condition (detector bias, noise threshold, conversion gain, etc.). For a PET scanner consisting of hundreds to thousands of detectors, the detector responses are generally non-uniform. The adverse effects of this phenomenon on images must be rectified by normalization of detector efficiency. This is usually realized by measuring an ideal uniform geometry source or a

rotating line source and adjusting the count of all detector pairs in proportion to their efficiency (Casey and Hoffman 1986).

Except for some refinement in adapting the existing method to 3D PET (Defrise *et al* 1991, Hoffman *et al* 1989, Stazyk *et al* 1994), efficiency normalization has been used as a standard data pre-processing step. Recent developments in this subject include more sophisticated normalization procedures with special considerations about: 1) simultaneous spectral and spatial non-uniformity correction for multiple energy PET acquisition (Msaki *et al* 1993a); 2) the difference in efficiencies between the scattered and non-scattered events resulting from their different energy and incident angle in fully 3D PET (Ollinger 1994).

Random coincidence

A distinct feature of PET is electronic collimation, which is realized by measuring coincidence events (Casey and Hoffman 1986). While two photons of an annihilation event (scattered or not) induce a true coincidence, two photons originating from two simultaneous but different annihilation events can also contribute to coincidence counts. Such accidental or random coincidences should be removed, as they do not convey any useful information about the source distribution.

The count rate of random coincidences is proportional to the duration of the coincidence time window and to the singles count rates of each coincident detector (Evans 1955). To minimize the random coincidences, the time window should be as small as possible. But it must be wide enough, for example, larger than twice the FWHM of the system time resolution, to detect most of the true coincidences. So, the choice of the time window is a compromise between these two requirements. Ideally, the time window should vary,

depending on the count rate load on the scanner, to provide optimal S/N (Bohm *et al* 1986, Kouris *et al* 1982).

Two widely used correction methods for random coincidence events are: 1) measuring the time window and count rates of singles in each detector to calculate the random counts; 2) measuring the random coincidences directly by delaying the signals from one of the two detectors to avoid the true events. The first method requires extra circuits to measure the singles count rates in each detector and the time window width of each coincidence pair must be known with high accuracy to avoid systematic errors. Its advantage is less statistical noise because of the high count rates of single detectors. On the contrary, the statistical noise of random events for the second method is high because of the low count rate, but the hardware requirement for implementing this method is smaller.

Attenuation

Photons arriving at the surface of the detectors are only a small fraction of the original annihilation events. Another fraction is lost due to the small solid angle spanned by the scanner and because of Compton scattering and photoelectric absorption of photons within the medium surrounding the source. This process is attenuation. Since PET records coincidence events, the attenuation factor for a coincident detector pair depends only on the length of the corresponding chord within the attenuating medium. By using an external source to make transmission scans with and without the imaged subject in place, the correction factors for all chords can be obtained and therefore accurate attenuation correction can be achieved. This enables PET to provide quantitative images, which is an important advantage of coincidence measurement. However, as attenuation correction factors can be very high, for example, it is about 7 for a head and as high as about 40 for a chest, the attenuation correction has to be performed with high accuracy to avoid drastic quantitative errors.

There are several problems which hamper accurate attenuation correction method using transmission scan. First, scattered events detected in the transmission measurements make the attenuation appear to be lower than the actual attenuation (*buildup effect*). Second, the additional stochastic noise due to counting statistics propagates into the corrected emission data (Dahlbom and Hoffman 1987). Third, any movement of the subject between the emission and transmission scans introduces discrepancies between image pixels and the corresponding attenuation coefficients. To overcome these problems, various attenuation correction methods have been proposed. They include: 1) using a rotating pin source and a mask (realized mechanically or electronically) to remove the scatter and random coincidences (Carson *et al* 1988); 2) making simultaneous emission and transmission scans to reduce the total scan time and therefore minimize the registration errors due to subject movement (Thompson *et al* 1989); 3) measuring singles instead of coincidence events in transmission scans to improve the statistics (deKemp and Nahmias 1994); 4) smoothing transmission data to reduce data variance (Chatziioannou and Dahlbom 1996).

It should be noted that the recorded emission data includes scattered events, while the transmission data may or may not include scatter, depending on the measuring technique. Hence, correction for scatter in both the transmission and the emission data is a prerequisite for accurate attenuation correction.

Scatter

When annihilation photons interact within the media through which they travel, there are three possible interaction types: Rayleigh (coherent) scattering, Compton (incoherent) scattering and photoelectric absorption. In tissue, the Compton scattering is preponderant and the Rayleigh scattering is negligible because the energy of the annihilation photon is high (~ 511 keV, Johns and Cunningham 1983).

When Compton scattering occurs between a photon and an electron, the photon changes its direction and loses a part of its energy to the electron. Because of the uncertainty on the position of interaction, a Compton scattered photon carries poor information about the original annihilation location. So if either photon of an annihilation pair is scattered, the coincidence event being detected generally degrades image quality. The scattered events degrade contrast by smearing counts from high activity regions into low activity regions, introduce quantitative errors through inaccurate attenuation correction (Gardner *et al* 1992, Hoffman and Phelps 1986, Jones *et al* 1992, Wienhard *et al* 1992, Henze *et al* 1983), and reduce the overall spatial resolution by broadening the true distribution (Lecomte *et al* 1990, 1991). Scatter has initially received less attention than attenuation until accurate quantitative imaging is at issue. Using smaller scintillator to improve resolution (Derenzo *et al* 1993) and removing the septa to increase sensitivity (Spinks *et al* 1992) in modern PET systems makes scatter problem more complicated (Bentourkia *et al* 1995) and more important than ever (Thompson *et al* 1992). Further discussions of scatter is presented in more detail below.

Review of existing scatter correction methods

General

The aim of scatter correction is to compensate for the effects of scatter in order to obtain the best quantitative estimate of the activity distribution within the object. Studies have previously shown that scatter distribution is nonstationary and is influenced by many factors: the object geometry and composition (Frey and Tsui 1990, Barney *et al* 1991), the source distribution (Floyd *et al* 1984, Barney *et al* 1993), the acquisition geometry and the detector characteristics (Bentourkia *et al* 1995). Many correction methods have been developed by exploiting various aspects of the knowledge about scatter, but only a few of

them are widely recognized and even fewer have been tested and accepted for high resolution PET.

Compared to PET, more SPECT systems have been implemented and naturally there are more scatter correction methods developed for it. As the imaging processes of PET and SPECT are similar, the same photon propagation model can be derived for the two systems by simply giving a PET coincidence event the same treatment as the single event of SPECT. Therefore, the correction algorithms for the two systems are to some extent interchangeable. The difference of emission photon energy for PET and SPECT can be accommodated by adjusting the relevant energy parameters in the algorithm. So the methods reviewed hereafter are generally applicable for both PET and SPECT, except as specified.

According to the way they treat the scattered photons, the existing scatter correction methods can be classified into four categories: 1) limiting the detection of scattered photons; 2) compensating for the effects of scattered events; 3) weighting the events detected; and 4) estimating scattered counts and making relevant correction. Briefly, the principles and the limitations of the methods in these four categories are described below. More detailed discussions can be found in an excellent review article (Buvat *et al* 1995a) and other literature (King *et al* 1992, Msaki *et al* 1996, Sorensen and Phelps 1987).

Limiting the detection of scattered photons

Since Compton scattering changes the energy of the incident photons, energy discrimination can be used to reject many of the Compton scattered photons. However, the limited energy resolution of PET and SPECT systems prevents a complete rejection. Usually, a window with certain width centered on the photopeak of the radioisotope (for example, 126-154 keV for ^{99m}Tc and 350-680 keV for 511 keV annihilation photons) is

used to preserve the detection efficiency while scatter is rejected. The center of the window can be slightly shifted upward to improve the performance of scatter discrimination (Koral *et al* 1986), but accurate quantification using this method only is impossible because the fraction of scattered photons in the photopeak window is unknown.

Compensating for the effects of scattered events

These methods attempt to remove the effects of scattered photons without precisely estimating their contribution. For example, in the effective attenuation correction, the buildup effect due to scatter is modeled as an effect function $b(x_p, y_p, x, y)$, where (x_p, y_p) and (x, y) are the positions of the primary event and of the measured event, respectively. The attenuation process is then expressed as:

$$n(x,y) = n_0(x_p, y_p) b(x_p, y_p, x, y) e^{-\int_l \mu(t)\,dt} \qquad (1.2)$$

where n_0 and n are the emitted and detected counts, $e^{-\int_l \mu(t)\,dt}$ accounts for attenuation on chord l, t is the position variable on l and $\mu(t)$ is the attenuation coefficient at position t. If a proper function $b(x_p, y_p, x, y)$ is available, it is evident from equation (1.2) that projection data free of the influence of scattered events can be obtained. However, obtaining $b(x_p, y_p, x, y)$ for various acquisition conditions is unrealistic and a too complicated problem to be calculated accurately for every specific cases (Wu and Siegel 1984, Ljungberg and Strand 1990a). Using a simplified buildup function makes implementation easier, but introduces quantification errors in the corrected data (Gilland *et al* 1991).

There are other simple compensating correction methods for scatter, such as multiplying the to be corrected image data by a scale factor related to the scatter fraction (King *et al* 1991), processing image data by filters (Metz filter, Wiener filter, etc.) related with the response function of the imaging system (Frey and Tsui 1993), and performing scatter (King *et al* 1988) and other corrections simultaneously with reconstruction using a comprehensive *a priori* detection probability matrix (Floyd *et al* 1985a, Bowsher and Floyd 1991, Frey *et al* 1993). While the assumptions made for these methods are straightforward, their implementation is complicated because many factors must be modeled at the same time. Usually these methods end up with introducing approximations which damage their potential.

Weighting the detected events

Weighting methods acquire data within a wide energy range. Each detected event is relocated by multiplying the event coordinates with a predetermined weighting matrix related to event energy (Halama *et al* 1988). Since the weighting matrix depends on many parameters, such as radioisotope, collimator and especially the object being imaged, using a predetermined weighting matrix seriously limits the implementation of these methods (Devito *et al* 1991, Jaszczak *et al*, 1991). The ignorance of scatter nonstationarity and the requirement for extra signal processing electronics represent additional disadvantages.

Estimating scattered events

The contribution of the scattered photons can be estimated either from the energy spectrum or the spatial distribution of scattered events. Figure 1.3 illustrates how this is done. The estimated scatter component is then subtracted from the original data or restored to contribute to the image formation. Methods aiming at estimating scatter have three evident advantages. First, scatter problem is studied independently from attenuation and reconstruction, this makes the estimation process simple to formulate. Second, the

scatter component can be estimated from measured data and *a priori* knowledge about the acquisition system. So it is more flexible than weighting methods. Third, using the physical description of the photon propagation process, various scatter correction schemes can be formulated explicitly (Msaki *et al* 1996). According to the work space where the scatter distribution is estimated (figure 1.3), estimating methods can be further classified into spatial convolution and spectral analysis categories.

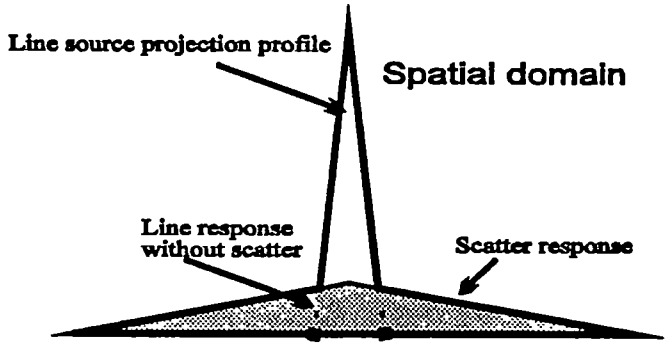

Figure 1.3a. The scatter component (shadowed) of a line source projection is obtained by extrapolating the long tails on each side of the line source. This is an example of using spatial distribution information to estimate scatter.

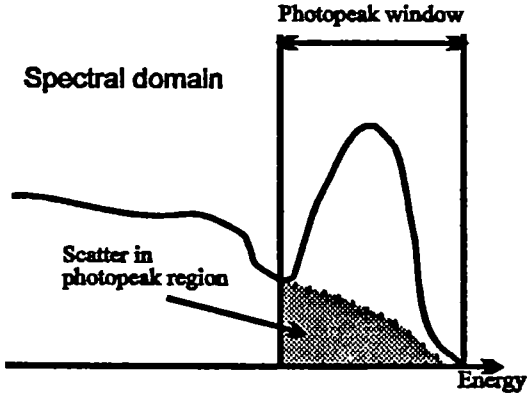

Figure 1.3b. Example of spectral scatter correction methods. The contribution of the scattered events to the photopeak is estimated by the shaded area which is obtained by modeling the Compton continuum spectral information.

Methods based on spatial convolution

The data acquired by an imaging system can be considered as a mixture of primary events and blurring contributions due to Compton scattering. Neglecting the contribution from random events and attenuation effects for simplicity, the data acquired at one point in the projection can be written as:

$$p(x) = \int t(x_p) h(x_p, x) dx_p \tag{1.3}$$

where $p(x)$ is the counts measured at position x, $t(x_p)$ is the primary projection of the source distribution, and $h(x_p, x)$ is the system response function at x for a source at x_p. The system response consists of a geometric channel $h_g(x_p, x)$, and a blurring channel $h_{sc}(x_p, x)$, such that $h(x_p, x) = h_g(x_p, x) + h_{sc}(x_p, x)$. $h_{sc}(x_p, x)$ is also known as the Scatter Response Function (SRF). As the geometric (primary photon) channel does not have blurring effects other than the system intrinsic resolution, $h_g(x_p, x)$ can be replaced by a delta function $\delta(x - x_p)$ (King *et al* 1991). Representing $h_{sc}(x_p, x)$ by $h_{sc}(x_p, x - x_p)$, i.e. h_{sc} depends on the source position and the distance between the source and measurement position, equation (1.3) can be written as:

$$\begin{aligned} p(x) &= \int t(x_p) h(x_p, x - x_p) dx_p \\ &= t(x_p) \otimes h(x_p, x) \\ &= t(x_p) \otimes [\delta(x - x_p) + h_{sc}(x_p, x)] \\ &= t(x) + t(x_p) \otimes h_{sc}(x_p, x) \end{aligned} \tag{1.4}$$

There are several ways for obtaining SRF, which include Monte-Carlo simulation (Beck *et al* 1982, Floyd *et al* 1985, Acchiappati *et al* 1989, Bendriem *et al* 1987), mathematical modeling (Egbert and May 1980), and phantom measurements (Bailey and Meikle 1994, Bentourkia *et al* 1995a, Bergström *et al* 1983, Prati *et al* 1993, Shao and Karp 1991). Various assumptions about $h_{sc}(x_p, x)$, for example, assuming it as stationary or piece-wise

nonstationary, have been made to achieve an approximated solution of equation (1.4) by performing convolution or deconvolution (Axelsson *et al* 1984, Bentourkia *et al* 1995a, Bergström *et al* 1983, Msaki *et al* 1987). By explicitly distinguishing the different scatter components corresponding to each sub-system (object, detector etc.), it is also possible to process these components selectively according to their relevance to image formation. Various scatter correction schemes can be devised (Msaki *et al* 1996) depending on the choice to preserve or remove scatter in the image formation process (Links 1995).

Convolution Subtraction (CS) algorithm

Convolution subtraction (Axelsson *et al* 1984, Bergström *et al* 1983, Msaki *et al* 1987) is the most commonly used scatter correction algorithm for both PET and SPECT. In this approach, scatter is considered as detrimental to the image and should be removed. The primary projection t is assumed to be formed only by the annihilation photons which are transmitted through the object and stopped in the detector without undergoing Compton interactions. The scatter contribution is estimated by an integral transformation of the measured projection using the SRF and then subtracted (Allard *et al* 1987, Bergström *et al* 1983, Hoverath *et al* 1993, King *et al* 1981, Paans *et al* 1989, Prati *et al* 1993, Shao and Karp 1991, Townsend *et al* 1989). From equation (1.4), we have:

$$t(x) = p(x) - t(x_p) \otimes h_{sc}(x_p, x) \tag{1.5}$$

Using the approximation $t(x_p) \otimes h_{sc}(x_p, x) \approx p(x) \otimes h'_{sc}(x_p, x)$, where $h'_{sc}(x_p, x)$ is obtained by fitting measured data (Bergström *et al* 1983), then

$$t(x) = p(x_p) \otimes \left[\delta(x - x_p) - h'_{sc}(x_p, x)\right] \tag{1.6}$$

In this algorithm, both nonstationary and stationary SRFs can be used. It should be noted that the scatter corrected projection $t(x)$ is the scatter-free distribution but still blurred by the finite resolution of the detection subsystem (Bentourkia *et al* 1995a). Even though this convolution subtraction procedure does not amplify noise, the statistical noise in $t(x)$ is relatively higher because of the reduction in total counts.

Deconvolution Restoration (DR) algorithm

Both the primary and scatter components are assumed to be useful to image formation for this algorithm. The response of each sub-system is included in the overall system response function $h(x_p, x)$ to form an inverse filter to restore the effects of all degradation processes in the measurement (Links *et al* 1990, 1992, Shao *et al* 1994a). A pre-requisite for doing this is that the SRF must be symmetric and shift-invariant, i.e. $h(x_p, x) = h(x - x_p)$. From equation (1.4), the primary projection distribution $t(x)$ can be obtained by deconvolution in Fourier domain:

$$t(x) = p(x_p) \otimes FFT^{-1}\left\{\frac{1}{FFT\left[h(x - x_p)\right]}\right\} \qquad (1.7)$$

Restoration methods can improve the image contrast and resolution without significantly degrading S/N because they preserve counts. However, the amplification of high frequency noise has to be limited. Methods using Metz and Wiener filters have been proposed to restore only the low frequency scatter component (Links *et al* 1992, King *et al* 1991). The assumption of symmetrical and shift-invariant SRF can lead to significant quantitative errors. In addition, the inclusion of object scatter in images would finally reduce resolution and complicate attenuation correction (Msaki *et al* 1996).

Convolution Subtraction & Deconvolution Restoration algorithm

After studying the characteristics of each component of the system response function in high resolution PET, Bentourkia *et al* (1996) have developed a subtraction & restoration method which subtracts object scatter and restores detector scatter without altering the geometric response. In this way, the undesirable scatter events from the object can be removed while the useful scatter events from the detector are recovered. So this method has some advantages over pure subtraction or restoration methods. When the detector scatter intensity is small, such as the case for low resolution PET systems, the effect of restoration disappears and the algorithm is identical to the convolution subtraction algorithm. This is the most relevant algorithm for the system used in this work.

Stationary and nonstationary SRF

Stationary SRF is defined as $h_{sc}(x_p, x) = h_{sc}(x_p - x)$, i.e. it is spatially shift-invariant. Most early works have been using spatially stationary SRF for scatter correction (Axelsson *et al* 1984, Floyd *et al* 1985b, 1985c, Msaki *et al* 1987, Mukai *et al* 1988). However, neglecting the dependence of SRF on object and acquisition geometry makes accurate estimation of scatter in several acquisition configurations impossible (Ljungberg *et al* 1990b, Msaki *et al* 1993b).

The nonstationary nature of scatter must be taken into consideration for accurate quantification of PET and SPECT images. Several methods have been suggested to obtain nonstationary SRF, which include measuring a line source placed at varying positions within a suitable phantom (Bergström *et al* 1983, Bentourkia *et al* 1995a) or using Monte Carlo simulation (Ljungberg and Strand 1990, Ollinger *et al* 1992, Waterson *et al* 1995). A model using Singular Value Decomposition (SVD) has also been proposed to address this problem (Lewitt *et al* 1994). Despite of the promising preliminary results reported, obtaining the nonstationary SRF routinely in the clinical settings still remains a major problem to be resolved.

Methods based on spectral analysis

The investigation on energy-based scatter correction methods have been going on for some time. For example, the availability of a second window on imaging systems has led to the development of the dual window scatter correction in SPECT (Jaszczak *et al* 1984) and more recently in PET (Grootoonk *et al* 1991). As more accurate energy information spanning a broader energy range becomes available in SPECT (Koral *et al* 1988, Waggett *et al* 1978) and PET (Lecomte *et al* 1992) imaging systems, novel energy-based scatter correction methods for these systems have been proposed. The anticipation of a more widespread use of such systems has stimulated simulation studies providing more detailed description of the energy characteristics of scattered events (Bentourkia *et al* 1995b, 1995c, Floyd *et al* 1984, Lecomte *et al* 1992, Thompson *et al* 1992). These studies were useful in formulating improved scatter correction techniques, which include the Triple Energy Window (TEW, Shao *et al* 1994), the Notched Energy Window (NEW, Thompson and Picard 1993) spectral fitting (Koral *et al* 1988. Wang and Koral 1992), Principal Component Analysis (PCA, Gagnon *et al* 1989) and Factor Analysis (FA, Mas *et al* 1990, Buvat *et al* 1993). These methods differ in the assumptions made about the energy characteristics of the true and scattered events. Their performance depends on how such assumptions are used in the derivation of the correction algorithms. Below, the main categories of spectral analysis methods for PET and/or SPECT are described. The methods specially related to PET are highlighted.

Pixel-by-pixel spectral analysis methods

In these methods, the spectrum of scattered photons is estimated using the data acquired in multiple energy windows. Pixel-by-pixel, the scatter contribution in the main data acquisition window, which can be the photopeak window or a wider range, is removed. Only primary events are left for image formation. Several methods using two or three

energy windows are based on the assumption that the scatter spectrum in the main window has a simple shape which can be estimated (King *et al* 1992, Pretorius *et al* 1993, Logan and McFarland 1992). Although such techniques are easy to implement, the rough spectrum estimation can cause significant inaccuracies. Some other methods try to decompose the spectrum using *a priori* information about the system energy response (East *et al* 1982, Koral *et al* 1988, Wang and Koral 1992, Maor *et al* 1991). However, factors such as the spatially variant nature of scatter, make it difficult to obtain the relevant *a priori* knowledge.

Global spectral analysis methods

By recording the spectrum of events over a wide energy range, a data set with both spatial and spectral information is obtained. Shown in figure 1.4 is a schematic diagram of the multispectral PET data set. The coincident energy windows (k,l) of each line of response (LOR) form a 2D energy spectrum (Lecomte *et al* 1992) as shown in figure 1.5. Like in conventional PET, the set of LORs associated with each window pair (k,l) can be rebinned into a sinogram in the projection space, which is called an *energy frame*.

Using existing mathematical data processing tools, such as Principal Components Analysis (PCA, Jolliffe 1986) or multivariate analysis (Seber 1984), the correlation between energy frames can be exploited to reduce the dimensionality of the data set. The first few components, which contain most of the correlated structure information in the original data set, are preserved for further data processing. Depending on the physical assumptions about these components, certain transformation or spectral decomposition can subsequently be performed to yield the scatter corrected data. Factor Analysis of Medical Imaging Sequences (FAMIS, Buvat *et al* 1993, Di Paola *et al* 1982, Mas *et al* 1990) and Holospectral Imaging (HI, Gagnon *et al* 1989) are approaches based on this concept.

Due to the lack of theoretical support for the underlying physical hypotheses about the principal components, the effectiveness of the method HI remains to be proved. By contrast, approaches based on FAMIS avoid hypotheses about the physical processes involved by employing the factor analysis only as a step for reducing noise tainting the data. Subsequently, pixel-by-pixel spectral decomposition is performed to extract a scatter-free component (Mas *et al* 1990, Buvat 1992). The need for *a priori* system energy response information for each pixel imposes significant difficulties to implement the technique in clinical applications (Buvat *et al* 1993). Till recently, almost all the tests dealing with the FAMIS methods have used simulated data (Buvat *et al* 1993, 1995b). No application in PET has been reported yet for either HI or FAMIS.

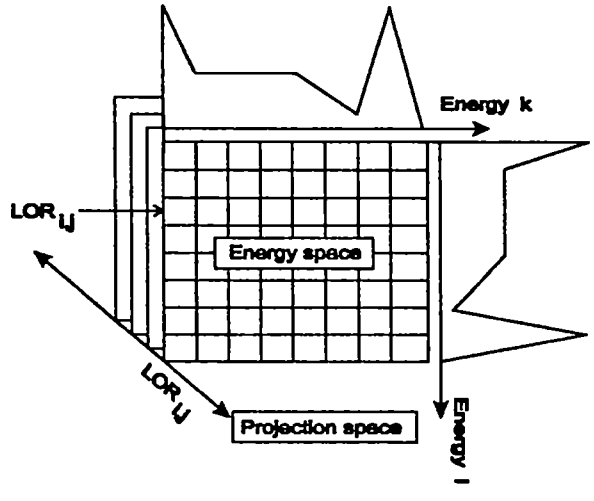

Figure 1.4. The multispectral data set records both the spatial and spectral information of detected events. Each projection point $LOR_{i,j}$ in the projection space is associated with a 2D energy spectrum in the spectral domain.

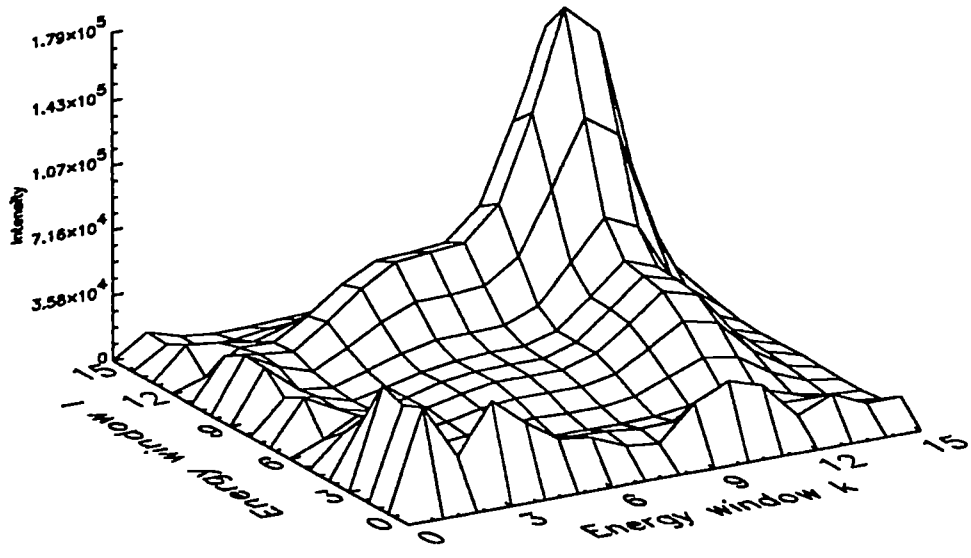

Figure 1.5 An example showing the energy distribution (spectrum) of a line of response (LOR) element in spatial domain.

Existing PET spectral analysis methods

Most scatter correction methods for PET are based on spatial convolution. It is only recently that spectral analysis methods, such as Dual Energy Window (DEW, Bendriem *et al* 1993, Grootoonk *et al* 1991), Triple Energy Window (TEW, Shao *et al* 1994b) and Notched Energy Window (NEW, Thompson and Picard 1993) have appeared. In principle, all these methods belong to the pixel-by-pixel spectrum analysis category discussed above. Because of the complexity of multispectral acquisition systems for PET and the difficulty of handling large dimension multispectral data set, no global spectral analysis method has yet been tested in PET.

DEW is the only PET spectral analysis method which has been implemented in commercial systems and which, thus, has received continuous attention (Cutler and Hoffman 1993, Harrison *et al* 1992, Sossi *et al* 1995). It uses two energy windows: an upper window encompassing the 511 keV positron annihilation photopeak, and a lower window

accepting coincidences in which one or both photons deposit energy in a lower energy range (200 keV ~ 380 keV). The true event count in the upper window is derived from the knowledge of two pre-determined, unscattered and scattered event ratios in the two windows. The main problems with DEW technique include noise amplification (Barney *et al* 1994) and the difficulty in obtaining appropriate *a priori* ratios for various imaging object (Cutler and Hoffman 1993, Harrison *et al* 1992, Sossi *et al* 1995). This method will be analyzed further in Chapter 2.

New scatter correction methodology: multispectral PET (MSPET)

Rationale

As mentioned earlier, most modern PET scanners use very small detectors to improve spatial resolution (Bloomfield *et al* 1995, Cherry *et al* 1996, Cutler *et al* 1992, Daghighian *et al* 1994, Watanabe *et al* 1992). For example, the PET scanner in Sherbrooke is based on 3x5x20 mm^3 individual BGO scintillators (Lecomte *et al* 1993, 1994). The main drawbacks of using small scintillators are: 1) the decreased sensitivity resulting from the lower intrinsic detection efficiency and the poorer packing fraction (Lecomte *et al* 1996, Murthy *et al* 1994); 2) the increased statistical noise resulting from the lower counts in the smaller pixels; 3) the increased inter-crystal scatter which reduces system sensitivity and resolution (Bentourkia *et al* 1995b, Lecomte *et al* 1991, Moses *et al.* 1993, Murthy *et al* 1994, Shao *et al* 1996). However, it has been demonstrated recently that by using a broad energy window (lowering energy threshold), it is possible to preserve the useful information resulting from detector scatter and, therefore, to recover the system sensitivity (Bentourkia *et al* 1996, Bentourkia and Lecomte 1996).

As shown in figure 1.4, another advantage of MSPET is that it increases the degrees of freedom for data manipulation. The energy dependence of the multispectral data provides valuable insight into the underlying physical processes. Using MSPET, it is easy to acquire data for all energy frames and study the energy dependence of various scatter parameters as presented in a recent work of Bentourkia and Lecomte (1996). Such additional information about scatter can be used to design new, more efficient scatter correction methods for PET.

When using broad window acquisition, the increased fraction of scattered events in the acquired data requires more efficient scatter correction methods. HI and FAMIS methods in SPECT have shown that multispectral acquisition provides more complete information on the detected events and allows for more flexible data manipulation. It is reasonable to postulate that MSPET has the potential for improving scatter correction efficiency as well.

Major problems

From the discussions about the existing scatter correction methods, it is evident that, compared to the methods based on spatial convolution which have relied explicitly on photon spatial degradation model (Msaki *et al* 1996), there has not been a model which includes the energy variable to describe the photon propagation process. This lack of theoretical guidance causes difficulties in developing spectral correction approaches.

Another common problem is that most existing scatter correction methods are confined to information either in the spatial or spectral domain only, few methods developed up to now has used both. Although such global consideration would be the logical way to optimally exploit information in data. In fact, both the spatial and spectral information

have inherent characteristics of the measured photon events, they must be considered together to ensure a more complete description of the physical detection process.

Several techniques proposed

To fulfill the need for theoretical guidance with energy-based scatter correction methods, the energy variable will be introduced into the conventional photon spatial degradation model (Msaki *et al* 1996) to formulate a photon spectral degradation model. Energy-dependent scatter correction methods such as DEW will be analyzed by this model.

Multispectral Frame-by-frame (MF) convolution scatter correction, whereby spatial scatter processing is conducted in each individual energy frame, is proposed as a method which employs both the spatial and spectral information. Anticipated problems for this approach include higher statistical fluctuations due to multiple energy windows, larger data storage requirements and heavier computation load. If the statistical noise in individual energy frame can not be completely resolved, the potential benefit of the method might be overwhelmed by the cumulated errors from each individual energy frame.

In order to advance the MF approach and to take full advantage of the spectral analysis capability and data processing flexibility offered by multispectral PET, it is essential to minimize the statistical fluctuations and systematic errors in multispectral data due to using multiple energy windows. By analyzing the origins of data variances, multispectral data pre-processing techniques which consist of spectral smoothing, normalization for detector efficiency and optimal data pre-processing sequence are proposed and studied to enhance the statistical significance of multispectral data.

Principal Component Analysis (PCA) is proposed as an alternative noise suppression technique using the concept of extracting correlated information among energy frames. To unify the spatial and spectral analysis, the result of PCA will be subsequently processed by the consecutive subtraction-restoration algorithm in the spatial domain to produce the final result. The essence of this method, referred to as Global Scatter Correction (GSC) method, is to thoroughly exploit the information in data.

Chapter 2 Theory

Standard photon degradation model & correction algorithms

Definitions

A high resolution PET system is considered as having two components in series (figure 2.1): the object (o) and detection (d) sub-systems. The response of each sub-system i ($i = o,d$) to a point source of unit radioactivity is assumed to have geometric (h_{ig}) and scatter (h_{is}) channels in parallel which transmit unscattered and scattered photons, respectively. As the intensity of the component(s) to be preserved for image formation in each sub-system is to be normalized to unity, the geometric and scatter responses are expressed as $f_{ig}h_{ig}$ and $f_{is}h_{is}$, respectively. The weight factors f_{ig} and f_{is} are the geometric and scatter fractions in the sub-system total response, such that $f_{ig} + f_{is} = 1$, $i = o,d$; h_{ig} and h_{is} are the corresponding response functions normalized to unity.

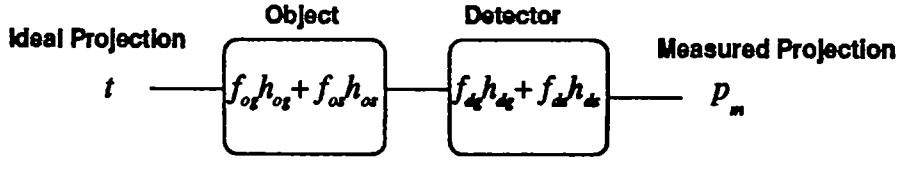

Figure 2.1. Photon degradation model for a system consisting of object (o) and detector (d) sub-systems in series. Each sub-system has a geometric (g) and a scatter (s) channel in parallel. The overall response to the ideal projection t produces the measured projection p_m.

Model

The data acquisition process can be expressed as::

$$p_m = t \otimes \left(f_{og}h_{og} + f_{os}h_{os}\right) \otimes \left(f_{dg}h_{dg} + f_{ds}h_{ds}\right) \qquad (2.1)$$

where the spatial variables have been omitted for clarity. This model can be shown to be the basis of most existing spatial convolution scatter correction methods. The choice to reform or remove scattered photons emerging from each sub-system forms various scatter correction schemes and determines the intensity of the true component in the measured projection at the output of the system (Msaki *et al* 1996). We will limit the following discussion to two algorithms. One is the widely accepted Convolution Subtraction (CS) method; another one is the most relevant method for the high resolution PET used in this work (OSDR, Bentourkia *et al* 1996).

Convolution Subtraction (CS) algorithm

As mentioned in Chapter 1, only the geometric channels are assumed to contribute useful photons for image formation in this algorithm. Accordingly, each of these channel responses should be re-normalized to unity. As the annihilation photons transmitted through the object are not degraded by blurring, h_{os} is simply a delta function. Adding the normalization factors to equation (2.1) and replacing h_{os} by δ,

$$\begin{aligned} p_m &= t \otimes \left[\left(f_{os} h_{os} + f_{os} h_{os} \right) / f_{os} \right] \otimes \left[\left(f_{ds} h_{ds} + f_{ds} h_{ds} \right) / f_{ds} \right] \\ &= t \otimes \left\{ h_{ds} + \left(f_{ds} / f_{ds} \right) h_{ds} + \left(f_{os} / f_{os} \right) h_{os} \otimes \left(h_{ds} + \left(f_{ds} / f_{ds} \right) h_{ds} \right) \right\} \\ &= t \otimes \left\{ f_s h_s + f_d h_d + f_o h_o \right\} \end{aligned} \qquad (2.2)$$

where the imaging system's response $h = f_s h_s + f_d h_d + f_o h_o$ is the sum of *geometric* ($f_s h_s = h_{ds}$), *detector scatter* ($f_d h_d = \left(f_{ds} / f_{ds} \right) h_{ds}$) and *object scatter* ($f_o h_o = \left(f_{os} / f_{os} \right) h_{os} \otimes \left(h_{ds} + \left(f_{ds} / f_{ds} \right) h_{ds} \right)$) components. Following equation (2.2), the measured projection p_m can be expressed as the sum of three independent components:

$$p_m = \varphi + s_d + s_o \tag{2.3}$$

where $\varphi = f_g h_g$, $s_d = f_d h_d$ and $s_o = f_o h_o$. The scatter-free projection φ is simply obtained by direct subtraction of the scatter distribution:

$$\begin{aligned} \varphi &= p_m - s_d - s_o \\ &= p_m - t \otimes \{f_d h_d + f_o h_o\} \\ &= p_m - t \otimes \left\{ \left(f_{ds} / f_{dg} \right) h_{ds} + \left(f_{os} / f_{og} \right) h_{os} \otimes \left(h_{dg} + \left(f_{ds} / f_{dg} \right) h_{ds} \right) \right\} \end{aligned} \tag{2.4}$$

Since the primary projection t is not known *a priori*, one might just approximate $s_o = t \otimes f_o h_o$ and $s_d = t \otimes f_d h_d$ by $s_o \approx p_m \otimes f_o' h_o'$ and $s_d \approx p_m \otimes f_d' h_d'$ respectively, where f_i' and h_i' are obtained by fitting the line source measurement (King *et al* 1981, Bentourkia *et al* 1995a). Then

$$\begin{aligned} p_{od} &= p_m - p_m \otimes f_d' h_d' - p_m \otimes f_o' h_o' \\ &= p_m \otimes \left(\delta - f_d' h_d' - f_o' h_o' \right) \end{aligned} \tag{2.5}$$

However, this approach would be inconsistent with the formulation of the model since the detector scatter $t \otimes \left[\left(f_{ds} / f_{dg} \right) h_{ds} \right]$ in equation (2.4) does not have any dependence on the object sub-system and, therefore, it should not be estimated from the measured projection which includes the degradation effects of the object sub-system. In order to overcome this difficulty, the object scatter-free projections p_o must first be obtained by the convolution-subtraction,

$$p_o = p_m - s_o = p_m \otimes \left(\delta - f_o' h_o' \right) \tag{2.6}$$

to remove all events formed by photons which pass through the h_{α} channel. One can then proceed to remove the detector scatter using similar approximations to estimate s_d by $p_o \otimes f_d' h_d' / (1 - f_o')$, where the factor $1/(1 - f_o')$ is required to normalize the detector scatter response to the intensity of a line source in air (without the object). This reasoning leads to:

$$\begin{aligned} \varphi &= p_o - s_d \\ &= \left\{ p_m \otimes (\delta - f_o' h_o') \right\} \otimes \left\{ \delta - f_d' h_d' / (1 - f_o') \right\} \end{aligned} \tag{2.7}$$

According to equation (2.7), the CS algorithm seeks to obtain the scatter-free distribution φ which is still blurred by the finite resolution of the detection sub-system h_{d_E}, instead of the primary projection t.

Object scatter Subtraction & Detector scatter Restoration (OSDR) algorithm

It has been shown that the benefits of removing s_d are only marginal in terms of image contrast, but are obtained at the expense of a substantial loss of scattered events which reasonably resolve the source (Bentourkia *et al*, 1995a). Such events could be included in image formation (Bentourkia *et al*, 1996). In order to incorporate a distinct treatment of selected scatter components, the OSDR algorithm in which object and detector scatter are segregated as undesirable and useful events, respectively, has been established. In this case, the ideal projection t is formed by all annihilation photons transmitted through the object. The degradation process producing the measured projection is then given by:

$$
\begin{aligned}
p_m &= t \otimes \left(\delta + \frac{f_{os} h_{os}}{f_{og}} \right) \otimes \left(f_{dg} h_{dg} + f_{ds} h_{ds} \right) \\
&= t \otimes \left\{ f_{dg} h_{dg} + f_{ds} h_{ds} + \left(f_{os} / f_{og} \right) \left[h_{os} \otimes \left(f_{dg} h_{dg} + f_{ds} h_{ds} \right) \right] \right\} \\
&= t \otimes \left\{ f_g h_g + f_d h_d + f_o h_o \right\}
\end{aligned}
\tag{2.8}
$$

where the *geometric* ($f_g h_g = h_{dg}$), *detector scatter* ($f_d h_d = f_{ds} h_{ds}$) and *object scatter* ($f_o h_o = \left(f_{os} / f_{og} \right) h_{os} \otimes \left(f_{dg} h_{dg} + f_{ds} h_{ds} \right)$) components are defined similar to those in equation (2.2). As both detector geometric and scatter channels are considered to contribute useful events to image formation, the detector sub-system response function is normalized to 1. Using the convolution subtraction algorithm in equation (2.6) to remove the object scatter and rewriting equation (2.8):

$$
\begin{aligned}
p_o &= p_m - s_o \\
&= p_m \otimes (\delta - f_o' h_o') \\
&= t \otimes (f_g h_g + f_d h_d)
\end{aligned}
\tag{2.9}
$$

Without attempting to recover fully resolution (Links *et al* 1992, Shao *et al* 1994a), the restoration for the blurring effects of the detector scatter component to reposition events in the geometric component can be realized by solving equation (2.9) using deconvolution (Bentourkia *et al* 1996):

$$
\varphi = p_o \otimes FT^{-1} \left\{ \frac{1}{f_g + FT(f_d h_d)} \right\}
\tag{2.10}
$$

where the approximation $h_d \approx h_d \otimes h_g$ has been used; FT and FT^{-1} are the forward and inverse Fourier transforms, respectively. To implement this algorithm, the detector response parameters, f_{dg} and $f_{ds} h_{ds}$, are required. If they are obtained by fitting the line

source projections in the presence of object scatter (Bentourkia *et al* 1995a), a normalization factor $\frac{1}{(1-f_o')}$ is needed for the two scale factors. Equation (2.10) becomes:

$$\begin{aligned}\varphi &= p_o \otimes FT^{-1}\left[\frac{(1-f_o')}{f_g' + FT(f_d' h_d')}\right] \\ &= p_m \otimes (\delta - f_o' h_o') \otimes FT^{-1}\left[\frac{(1-f_o')}{f_g' + FT(f_d' h_d')}\right]\end{aligned} \qquad (2.11)$$

Photon spectral degradation model

The spatial scatter degradation model (Msaki *et al* 1996) has provided theoretical foundation to the question of *which scatter component in terms of its origin (object, detector) should be preserved in or removed from image formation* (Links *et al* 1995). A similar question, i.e. *which event in terms of its energy, should be preserved in or removed from image formation*, arises in high resolution imaging systems where the lower energy threshold can no longer be a critical dividing line between predominantly low energy scattered photons and predominantly high energy unscattered (primary) photons (Bentourkia *et al* 1995b). To answer this question, the energy characteristics of scattered and unscattered events have to be studied theoretically and experimentally.

Definition of energy variables

In order to keep track of the photon energy in the propagation process, sub-system responses will be considered to have multiple energy channels transmiting photons over a broad energy range. These multiple energy channels form what has been referred to as the *energy space* (figure 2.2). Since PET has a two dimensional energy space, a point in

this space (e) corresponds to an event detected with energy falling in a certain window pair. In addition, two energy variables are needed to characterize photons traveling through each sub-system: the input and the output photon energy. The primary photon energy is denoted by e_p and the resulting energy from a sub-system i ($i = o,d$) by e_i. Since the sub-systems are in series, the object will receive primary photons e_p from the source while the detector will receive a mixture of transmitted (e_p) and scattered photons (e_o) from the object.

Global definition of response functions

For multispectral system, sub-system responses depend on the energy and position of input events. For instance, the complete expression of the object response function is $f_{os}h_{os}(x_p,x_o;e_p,e_o)$, where x_p and e_p are the input position and energy of primary photons, x_o and e_o the position and energy of emerging photon from the object, and f_{os} the object scatter fraction of the sub-system response. Similarly, the detector geometric response function can be expressed as: $f_{dg}h_{dg}(x_o,x_d;e_o,e_d)$. Note that the parameters f_{ig} and f_{is} ($i = o,d$) are also functions of spatial and energy variables, which were omitted for clarity. The semicolon in these expressions is used to separate the spatial and energy variables.

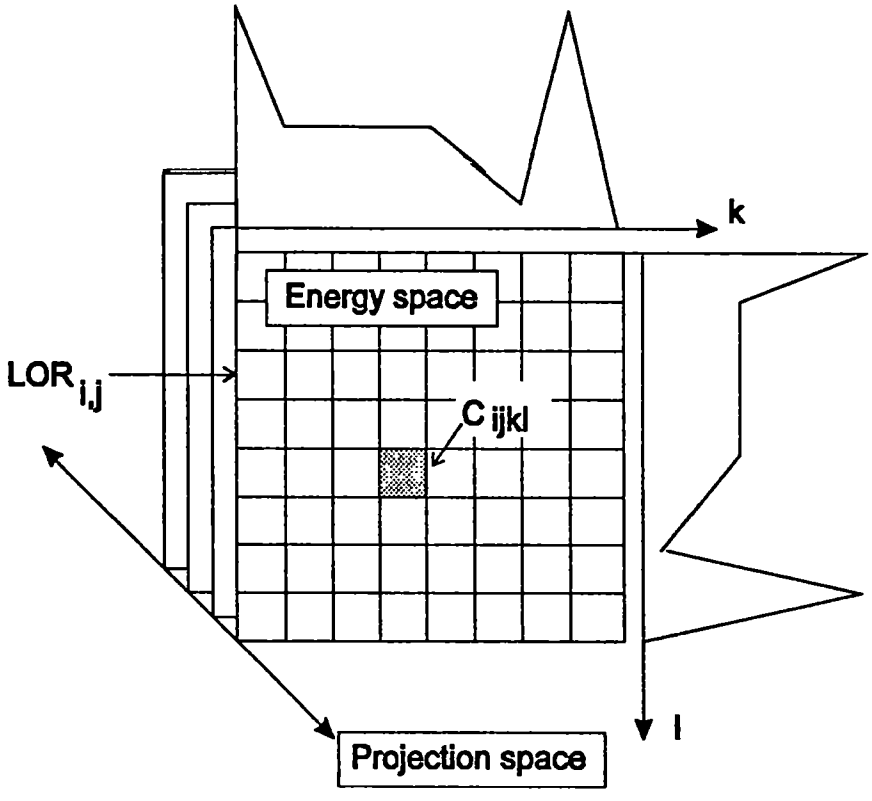

Figure 2.2. Schematic diagram showing the structure of multispectral data set. A 2D energy spectrum in the energy space is defined for every $LOR_{i,j}$ between pairs of opposing detectors in the projection space.

Sub-system geometric channel response functions

Since the annihilation photons transmitted through the object do not interact with the medium, h_{o_E} is simply a delta function in both the spatial and energy domains, such that $h_{o_E} = \delta(x_o - x_p; e_o - e_p)$. The detector geometric response function h_{d_E} can be assumed to be a delta function in the spatial domain, but it has a complex spectral distribution in energy space which is determined by the detection characteristics of the detector (Bentourkia *et al* 1995c), i.e.

$$h_{d_E} = h_{d_E}(x_o, x_d; e_o, e_d) = \delta(x_d - x_o) h_{d_E}(e_o, e_d)$$

This is so because the geometric channel of the detector sub-system does not change the spatial distribution of incident photons whereas the events may be registered at an energy lower than that of the incident photon due to escape of the Compton scattered photons.

Sub-system scatter channel response functions

As have been reported by many groups (Adam *et al* 1996, Bergström *et al* 1983, Barney *et al* 1991, Bentourkia *et al* 1995b, Thompson *et al* 1993), the object scatter channel, h_{os} outputs a smooth and broad distribution in both the spatial and the energy domains. Due to the difficulty of locating the position of emission from object scattered events measured, photons passing through the h_{os} channel have relatively little useful information.

The detector scatter response h_{ds} is formed by photons scattered in the primary detector and detected by neighboring detectors. Because of the high stopping power of detector materials, the spatial distribution of h_{ds} is narrow and centered about the primary photon incidence location (Adam *et al* 1996, Bentourkia *et al* 1995a). Its energy distribution depends on the source energy and acquisition geometry.

Model

Using the global definition of sub-system responses and rewriting equation (2.1), the measured projection at point e_d in the energy space is:

$$p_m(x_d,e_d) = t(x_p,e_p) \otimes \left[f_{os}h_{os}(x_p,x_o;e_p,e_o) + f_{os}h_{os}(x_p,x_o;e_p,e_o)\right] \otimes \left[f_{ds}h_{ds}(x_o,x_d;e_o,e_d) + f_{ds}h_{ds}(x_o,x_d;e_o,e_d)\right] \quad (2.12)$$

Using the knowledge of sub-system response functions described above, we can expand equation (2.12) as:

$$
\begin{aligned}
p_m(x_d;e_d) &= t(x_p;e_s)\otimes\Big\{f_{os}f_{ds}\delta(x_o-x_p;e_o-e_p)\otimes\big[\delta(x_d-x_o)h_{ds}(e_o,e_d)\big] \\
&\quad + f_{os}f_{ds}\delta(x_o-x_p;e_o-e_p)\otimes h_{ds}(x_o,x_d;e_o,e_d) \\
&\quad + f_{os}h_{os}(x_p,x_o;e_s,e_o)\otimes\big[f_{ds}\delta(x_d-x_o)h_{ds}(e_o,e_d)+f_{ds}h_{ds}(x_o,x_d;e_o,e_d)\big]\Big\} \\
&= t(x_p;e_p)\otimes\Big\{f_{os}f_{ds}\delta(x_d-x_p)h_{ds}(e_p,e_d) \\
&\quad + f_{os}f_{ds}h_{ds}(x_p,x_d;e_p,e_d) \\
&\quad + f_{os}f_{ds}\big[h_{os}(x_p,x_d;e_p,e_o)\otimes h_{ds}(e_o,e_d)\big]+f_{os}f_{ds}\big[h_{os}(x_p,x_o;e_p,e_o)\otimes h_{ds}(x_o,x_d;e_o,e_d)\big]\Big\} \\
&= t(x_p,e_p)\otimes\Big\{f_{os}f_{ds}h_{ds}(x_p;e_p,e_d) \\
&\quad + f_{os}f_{ds}h_{ds}(x_p,x_d;e_p,e_d) \\
&\quad + f_{os-d}h_{os-d}(x_p,x_d;e_p,e_d)\Big\}
\end{aligned}
\tag{2.13}
$$

where

$$
\begin{aligned}
&f_{os-d}h_{os-d}(x_p,x_d;e_p,e_d)= \\
&f_{os}f_{ds}\big[h_{os}(x_p,x_d;e_p,e_o)\otimes h_{ds}(e_o,e_d)\big]+f_{os}f_{ds}\big[h_{os}(x_p,x_o;e_p,e_o)\otimes h_{ds}(x_o,x_d;e_o,e_d)\big]
\end{aligned}
\tag{2.14}
$$

Equation (2.13) can be rewritten as:

$$
p_m(e_d)=\varphi(e_d)+s_d(e_d)+s_o(e_d) \tag{2.15}
$$

where $\varphi(e_d)=t(x_p,e_p)\otimes\big[f_{os}f_{ds}h_{ds}(x_p;e_p,e_d)\big]$,

$$
s_d(e_d)=f_{os}f_{ds}\big[t(x_p;e_p)\otimes h_{ds}(x_p,x_d;e_p,e_d)\big]
$$

and

$$
s_o(e_d)=f_{os-d}\big[t(x_p;e_p)\otimes h_{os-d}(x_p,x_d;e_p,e_d)\big].
$$

Equation (2.15) describes the spectral photon degradation process by expressing the system response in a certain energy frame. Its first term $\varphi(e_d)$ corresponds to the annihilation photons transmitted through the object and detected by primary detectors: it is a delta function in the spatial domain with a characteristic spectral distribution in energy space. The second term $s_d(e_d)$ is the detector scatter channel response whereby photons transmitted through the object get scattered in the detector array before being detected. This component is a slightly blurred projection of the source distribution. It is therefore plausible to preserve and restore this component for image formation. But before the restoration operation, this term still falls into the scattered event category. The third term $s_o(e_d)$ is formed by object scattered photons detected by primary (h_{d_p}) or neighboring detectors (h_{d_s}). As the distribution of the object scattered photons is already broad, the further blurring effect of the detector sub-system does not significantly change the characteristics of the measured object scatter component $s_o(e_d)$. This third term is considered to retain little information about the source.

Because of the limited energy resolution of detection systems, the detector responses, h_{d_p} and h_{d_s}, are in fact blurred by the system energy resolution function $r(e_d, e)$. The projection measured in an energy window e_w becomes:

$$\begin{aligned} p_m(e_w) &= \left[p_m(e_d) \otimes r(e_d, e)\right]_{e=e_w} \\ &= \left\{\left[\varphi(e_d) + s_d(e_d) + s_o(e_d)\right] \otimes r(e_d, e)\right\}_{e=e_w} \end{aligned} \tag{2.16}$$

The formula described above can be used to investigate energy-based scatter correction methods and to guide the development of new spectral scatter correction techniques.

Multispectral scatter correction methods

Analysis of the Dual Energy Window (DEW) method

The spectral information obtained through multiple energy window acquisition holds the promise of more selective discrimination of scattered and unscattered photons and more accurate correction for scatter in images (Benali *et al* 1993, Gagnon *et al* 1989, Lecomte *et al* 1992, Yao *et al* 1996a). The Dual Energy Window (DEW) scatter correction method which represented the initial attempt to exploit the spectral information has been implemented in both SPECT (Jaszczak *et al* 1984, King *et al* 1992, Pretorius *et al* 1993) and PET (Grootoonk *et al* 1991, Spinks *et al* 1992). Its simple implementation makes the approach attractive. In addition, it is claimed to take into consideration the scatter originating from outside of the field of view (Grootoonk *et al* 1991, Naudé *et al* 1996). However, the validity of DEW method has been questioned from time to time when results showing its poor performance were reported. No rigorous explanation has yet been given for the unsatisfactory results obtained by this method (Harrison *et al* 1992, Cutler and Hoffman 1993).

The DEW technique in both SPECT and PET uses two energy windows with the upper one containing the photopeak (e_u) and the lower one placed on the Compton region of the spectrum (e_l). The true (unscattered) event counts in the upper window $T(e_u)$ is derived from a knowledge of the two pre-determined ratios of scattered (R_{sc}) and unscattered events (R_{unsc}) between the upper and lower energy windows.

$$T(e_u) = \frac{[C(e_u)R_{sc}] - C(e_l)}{R_{unsc} - R_{sc}} \qquad (2.17)$$

where $C(e_u)$ and $C(e_l)$ are the total counts measured in each window. The DEW method assumes that R_{sc} and R_{unsc} are constant or simple functions of position for different configurations. This approximation facilitates the determination of R_{sc} and R_{unsc} values.

It is evident that the quality of the correction technique greatly depends on the relevance of the pre-determined ratios R_{sc} and R_{unsc} to the actual measurement conditions. By definition of R_{sc} and R_{unsc} and equation (2.15), we have:

$$\begin{aligned} R_{unsc} &= \frac{C_{unsc}(e_l)}{C_{unsc}(e_u)} \\ &= \frac{\left\{\varphi(e_d) \otimes r(e_d, e)\right\}\Big|_{e=e_l}}{\left\{\varphi(e_d) \otimes r(e_d, e)\right\}\Big|_{e=e_u}} \\ &= \frac{t(x_p; e_p) \otimes h_{unsc}(e_l)}{t(x_p; e_p) \otimes h_{unsc}(e_u)} \end{aligned} \tag{2.18}$$

$$\begin{aligned} R_{sc} &= \frac{C_{sc}(e_l)}{C_{sc}(e_u)} \\ &= \frac{\left[s_d(e_d) + s_o(e_d)\right] \otimes r(e_d, e)\Big|_{e=e_l}}{\left[s_d(e_d) + s_o(e_d)\right] \otimes r(e_d, e)\Big|_{e=e_u}} \\ &= \frac{t(x_p; e_p) \otimes h_{sc}(e_l)}{t(x_p; e_p) \otimes h_{sc}(e_u)} \end{aligned} \tag{2.19}$$

where C_{unsc} and C_{sc} are the unscattered and scattered counts acquired from a phantom measurement, and h_{unsc} and h_{sc} are the unscattered and scattered channel responses of the system:

$$\begin{aligned} h_{unsc}(e_w) &= f_{og} f_{dg} h_{dg}(x_p; e_p, e_d) \otimes r(e_d, e)\Big|_{e=e_w} \\ h_{sc}(e_w) &= \left\{\left[f_{og} f_{ds} h_{ds}(x_p, x_d; e_p, e_d) + f_{os-d} h_{os-d}(x_p, x_d; e_p, e_d)\right] \otimes r(e_d, e)\right\}\Big|_{e=e_w} \end{aligned} \tag{2.20}$$

Substituting h_{unsc} and h_{sc} in equation (2.18) and equation (2.19), then

$$R_{unsc} = \frac{\left\{ f_{og} f_{dg} \left[t(x_p;e_p) \otimes h_{dg}(x_p;e_p,e_d) \otimes r(e_d,e) \right] \right\}\Big|_{e=e_w}}{\left\{ f_{og} f_{dg} \left[t(x_p;e_p) \otimes h_{dg}(x_p;e_p,e_d) \otimes r(e_d,e) \right] \right\}\Big|_{e=e_w}} \tag{2.21}$$

$$R_{sc} = \frac{\left\{ t(x_p;e_p) \otimes \left[f_{og} f_{ds} h_{ds}(x_p,x_d;e_p,e_d) + f_{os-d} h_{os-d}(x_p,x_d;e_p,e_d) \right] \otimes r(e_d,e) \right\}\Big|_{e=e_w}}{\left\{ t(x_p;e_p) \otimes \left[f_{og} f_{ds} h_{ds}(x_p,x_d;e_p,e_d) + f_{os-d} h_{os-d}(x_p,x_d;e_p,e_d) \right] \otimes r(e_d,e) \right\}\Big|_{e=e_w}} \tag{2.22}$$

In equation (2.21), $r(e_d,e)$ and $t(x_p;e_p)$ are common to both numerator and denumerator, so R_{unsc} is determined by the distribution of $h_{dg}(x_p;e_p,e_d)$ in energy space, which is spatially invariant. In addition, $h_{dg}(x_p;e_p,e_d)$ depends only on the detection sub-system and is free of the influence from the object. Therefore, R_{unsc} is relatively stable for a given system and the assumption about R_{unsc} in DEW is reasonable. This conclusion is in agreement with the observation made by Sossi *et al* (1995) and has been used in developing a modified DEW scatter correction method (Bendriem *et al* 1993).

In equation (2.22), $t(x_p;e_p)$ and $r(e_d,e)$ are distributions with fixed position and a small energy range, respectively. So R_{sc} is mainly dependent on the scatter channel response function of the system h_{sc}. As shown in equation (2.20), h_{sc} is spatially variant. Therefore, R_{sc} is a complicated function of position and object characteristics which is contrary to the assumption of DEW. This feature of R_{sc} has been noted by Harrison *et al* (1992) as well as Cutler and Hoffman (1993).

As a special case, let us assume an ideal system with perfect system energy resolution measuring a point source, i.e. $t(x_p;e_p) = \delta(x - x0; e - e_p)$ and $r(e_d,e) = \delta(e - e_d)$, $x0$ being a constant. Then equation (2.22) becomes:

$$R_{sc} = \frac{\left[f_{os} f_{ds} h_{ds}(x0, x_d; e_p, e_l) + f_{os-d} h_{os-d}(x0, x_d; e_p, e_l)\right]}{\left[f_{os} f_{ds} h_{ds}(x0, x_d; e_p, e_u) + f_{os-d} h_{os-d}(x0, x_d; e_p, e_u)\right]} \tag{2.23}$$

In accordance with works reported by several groups (Barney *et al* 1991, Bentourkia *et al* 1995, Harrison *et al* 1992, King *et al* 1981) and considering only the object scatter component for simplicity, the scatter distribution in window e_w can be approximated by:

$$h_{sc} = A_{sc}(x0, e_w)\exp\left[S_{sc}(x0, e_w)(x_d - x0)\right] \tag{2.24}$$

where A_{sc} and S_{sc} are the amplitude and shape parameters of the scatter distribution, $(x_d - x0)$ is the distance between the source and position on the projection. Combining equation (2.23) and equation (2.24), we have:

$$\begin{aligned} R_{sc} &= \frac{A_{sc}(x0, e_l)\exp\left[S_{sc}(x0, e_l)(x_d - x0)\right]}{A_{sc}(x0, e_u)\exp\left[S_{sc}(x0, e_u)(x_d - x0)\right]} \\ &= \left[A_{sc}(x0, e_l)/A_{sc}(x0, e_u)\right]\exp\left\{\left[S_{sc}(x0, e_l) - S_{sc}(x0, e_u)\right](x_d - x0)\right\} \end{aligned} \tag{2.25}$$

Because $S_{sc}(x0, e_l)$ is not the same as $S_{sc}(x0, e_u)$, and $A_{sc}(x0, e_l)$ does not necessarily have a simple relationship with $A_{sc}(x0, e_u)$ (Bentourkia *et al* 1995b), it is concluded that R_{sc} is a complicated function of source position, object geometry and energy window setting even for this simple configuration.

The above conclusion is unlikely to be changed if the former configuration is redefined to include the source distribution and the energy resolution factor. Furthermore, since no assumption has been made regarding the acquisition geometry, the conclusion generally applies to systems with different detector assemblies, such as small individual detectors,

continuous or block detectors. In other words, the difficulty of the DEW method originates only from its irrelevant assumptions. To make the technique applicable, a systematic evaluation of the influence of various factors, including source position, object and detector characteristics, would be required to obtain families of R_{sc} curves describing a wide range of object and system configurations.

As mentioned earlier, consideration about scatter from Outside Field Of View (OFOV) was an important feature of the DEW technique. This consideration can be easily incorporated into the proposed degradation analysis. Assuming the OFOV source distribution is $t_{OFOV}(x_{sc}, e_{sc})$, then its contribution to detected events can be described as object scattered photons detected by the detector. The only difference of this term from that of equation (2.14) is the source distribution. Easy to see, the contribution of OFOV scatter only further increases the complexity of R_{sc}.

Multispectral Frame-by-frame (MF) scatter correction & data pre-processing

MF convolution algorithm

The objective of this method is to perform scatter correction more accurately in terms of energy. The method consists of two steps: first, a selected spatial convolution scatter correction algorithm such as CS is applied to each energy frame; second, all the scatter corrected frames are summed together to give the final result. Various spatial scatter correction models can be used, but the OSDR model was chosen in this work. The algorithm of the method is then expressed as:

$$\sum_{e_d} \varphi(e_d) = \sum_{e_d} \left\{ p_m(e_d) \otimes \left[\delta - f_o'(e_d) h_o'(e_d) \right] \right\} \otimes FT^{-1} \left\{ \frac{1 - f_o'(e_d)}{f_s'(e_d) + FT\left[f_d'(e_d) h_d'(e_d) \right]} \right\} \tag{2.26}$$

where the variable e_d indicates an energy frame, the expressions about projection and scatter functions are the same as used in equation (2.11). The resolution factor and spatial variables as used in equation (2.15) are neglected here for simplicity. The assumptions used to derive this algorithm are closed related with those used for the BW OSDR method:

$$p_m(e_d) \otimes f_o' h_o'(e_d) \approx t(e_s) \otimes f_o h_o(e_d) \tag{2.27}$$

and

$$\varphi(e_d) \otimes \left[\frac{f_s'(e_d) + f_d'(e_d) h_d'(e_d)}{1 - f_o'(e_d)} \right] \approx t(e_s) \otimes h_s(e_d) \otimes \left[f_s(e_d) + f_d(e_d) h_d(e_d) \right]$$
$$\approx t(e_s) \otimes \left[f_s(e_d) h_s(e_d) + f_d(e_d) h_d(e_d) \right] \tag{2.28}$$

Comparing the MF method and its approximations (equations 2.26-28) with that of the standard single window mode OSDR algorithm (equation 2.11), we can see clearly that MF method has the advantage of more accurate energy discrimination ability over algorithms using only one wide window. However, it also has the disadvantage of having lower statistics in practice, because data are processed in each energy frame. Since the scatter corrected data are summed together to give the final result, the errors introduced in each energy frame may accumulate.

To reduce the error introduced by the low statistics in individual energy frames, multispectral data pre-processing techniques must be developed to reduce the exaggerated data variance due to using multiple energy windows and should be applied to measured data before performing MF. Compared with the conventional single window scatter

correction method, the combination of pre-processing and multispectral MF scatter correction would result in much heavier calculation load and data storage requirement.

Multispectral data pre-processing

The additional degree of freedom provided by the multispectral acquisition facilitates the design of variance reducing techniques free of these drawbacks. By smoothing data directly in the energy space, the spatial distribution of the measured events is not altered since counts are not moved across the lines-of-response (LORs). Hence, it is plausible that such spectral smoothing could reduce the overall variance of PET data without degrading the spatial resolution, thereby overcoming the inherent drawbacks of spatial domain smoothing. Because the smoothing and normalization procedures are conducted in the energy and spatial domains, respectively, the reduction of stochastic variances and systematic errors is likely to be achieved independently. Moreover, since spatial distributions are not changed, statistical fluctuations of random and emission data can be reduced by smoothing the distributions independently before or collectively after correction of random events.

These postulates have been tested by comparing the ability of four smoothing techniques in the energy space, which utilize various amounts of prior spectral information to restore distortions due to statistical fluctuations in both the energy and spatial domains. The effects of the sequence in which smoothing, normalization of detector efficiency and subtraction of random events are performed on the overall variance reduction have also been investigated. The effectiveness of the spectral smoothing and pre-processing sequences will be assessed by comparing the processed data, in both the spectral and spatial domains, with reference data obtained in high statistics.

Definitions

In most PET systems, including the Sherbrooke PET simulator (Lecomte *et al* 1990, 1993), detectors are grouped in set i in coincidence with opposite set j. The collection of lines-of-response LOR_{ij} joining detectors i and j forms a subset in the spatial domain which will be referred to as the *projection space*. In conventional PET, this space holds the data sets C_{ij} formed by photons detected in coincidence and R_{ij} obtained from an independent measurement of random coincidences. The projection space forms a natural data set for noise reduction techniques in the spatial domain (Casey and Hoffman 1986). In multispectral acquisition, events are further classified according to their energy. This additional information adds another dimension to the acquired data, as shown in figure 2.2. In this multidimensional space, each point is formed by the intersection of energy windows k and l of detectors i and j, respectively. The series formed by the energy coordinates is the *energy space* which, upon acquisition, becomes occupied by data C_{ijkl} and R_{ijkl}. The energy space forms yet another natural data set in which noise reduction techniques in multispectral PET can be performed.

Origins of data fluctuations

Low statistics is the principal factor which compromises much of the potential high resolution PET with multispectral acquisition capability can offer. The statistical fluctuations inherent in measured multispectral data C_{ijkl} can be given by:

$$C_{ijkl} = \left(T^{*}_{ijkl} \pm \varepsilon^{T}_{ijkl}\right) + \left(P^{*}_{ijkl} \pm \varepsilon^{P}_{ijkl}\right) \qquad (2.29)$$

where T and P stand for the true coincidences (including scatter) and the prompt random events, respectively. Their statistical deviations from the expected values marked by * are indicated by ε. Since scatter and attenuation corrections are conducted in subsequent processing steps, their variance generation potential will not be considered here. For this

reason, the sum of true and scatter coincidence events have been collectively denoted by T. The net true coincidence counts T^R, obtained by subtracting randoms estimated by an independent measurement, is given by:

$$T^R_{ijkl} = \left(T^*_{ijkl} \pm \varepsilon^T_{ijkl}\right) + \left(P^*_{ijkl} \pm \varepsilon^P_{ijkl}\right) - \left(R^*_{ijkl} \pm \varepsilon^R_{ijkl}\right)$$

where ε^R represents the fluctuations in the independently measured random counts R about the expected value R^*.

In order to explicitly include the systematic errors due to variations of detector efficiency in variance estimation, the global mean counts in the projection space for true emission, prompt and measured randoms will be denoted by $\overline{T_{kl}}$, $\overline{P_{kl}}$ and $\overline{R_{kl}}$, respectively. After random correction, the overall variance of counts acquired from a plane or uniform source in one energy window pair (k,l) is given by

$$\sigma_{kl}^2 = \frac{1}{m^2} \sum_{i,j=0}^{m-1} \left\{ \left(\overline{T_{kl}} + \overline{P_{kl}} - \overline{R_{kl}}\right) - \left(T^*_{ijkl} \pm \varepsilon^T_{ijkl} + P^*_{ijkl} \pm \varepsilon^P_{ijkl} - R^*_{ijkl} \pm \varepsilon^R_{ijkl}\right) \right\}^2 \qquad (2.30)$$

where the detectors in opposing arrays vary from i=0,1,2,...,m-1 and j=0,1,2,...,m-1. Expanding equation (2.30) and neglecting higher order ε terms, the variance σ_{kl}^2 in the projection space due to uneven detector efficiency, low statistics and subtraction of random events becomes:

$$\sigma_{kl}^2 \approx \frac{1}{m^2} \sum_{i,j=0}^{m-1} \left(\varepsilon^D_{ijkl}\right)^2 + \frac{1}{m^2} \sum_{i,j=0}^{m-1} \left(\varepsilon^T_{ijkl}\right)^2 + \frac{1}{m^2} \sum_{i,j=0}^{m-1} \left(\varepsilon^P_{ijkl}\right)^2 + \frac{1}{m^2} \sum_{i,j=0}^{m-1} \left(\varepsilon^R_{ijkl}\right)^2 \qquad (2.31)$$

where the systematic error due to variations in detector efficiency is:

$$\varepsilon^{p}_{ijkl} = \left(\overline{T_{kl}} + \overline{P_{kl}} - \overline{R_{kl}}\right) - \left(T^{*}_{ijkl} + P^{*}_{ijkl} - R^{*}_{ijkl}\right)$$

By definition, equation (2.31) can be written as the sum of the variance due to systematic error $\left(\sigma^{p}_{kl}\right)^2$ and counting statistics of emission data $\left(\sigma^{T}_{kl}\right)^2$, prompt random coincidences $\left(\sigma^{r}_{kl}\right)^2$ and subtracted random events $\left(\sigma^{s}_{kl}\right)^2$:

$$\sigma_{kl}{}^2 \approx \left(\sigma^{p}_{kl}\right)^2 + \left(\sigma^{T}_{kl}\right)^2 + \left(\sigma^{r}_{kl}\right)^2 + \left(\sigma^{s}_{kl}\right)^2 \qquad (2.32)$$

Random subtraction is usually the first data correction in conventional PET. The contribution of $\left(\sigma^{s}_{kl}\right)^2$ can be neglected if the random distributions are estimated from single event rates since the correction is then almost noiseless (Brooks *et al* 1980). This is not the case when random distributions are estimated from an independent measurement in a delayed coincidence channel where $\sigma^{s}_{kl} \approx \sigma^{r}_{kl}$. Attempts to reduce this variance by smoothing random data in the projection space have been made (Casey and Hoffman 1986, Dahlbom and Hoffman 1987, Sashin *et al* 1992) but these approaches are only valid if the systematic variance $\left(\sigma^{p}_{kl}\right)^2$ resulting from differences in detection efficiency is low. This condition is neither satisfied when acquisition is based on block detectors (Cherry *et al* 1995, Dahlbom and Hoffman 1988) nor when the shape and intensity of multispectral data acquired by different detector pairs are significantly different (Msaki *et al* 1993a). In these situations, normalization for detector efficiency should be applied to both emission and delayed random data before smoothing is conducted in the projection space.

Variance reduction in the energy space

Variance reduction techniques performed in the energy space are introduced in this section to overcome the limitations described above. In multispectral acquisition, each energy frame is confined to one LOR. Since smoothing within an energy frame does not move counts across LORs, the variance reduction is expected to be achieved without degrading

spatial resolution. For the same reason, the emission and random data sets can be processed independently. Variance reduction by such spectral smoothing can be performed in a number of ways using various degrees of *a priori* information.

Prior Constrained (PC) smoothing:

The most straightforward method to suppress statistical noise in energy space is to redistribute counts using *a priori* spectral information derived from *ideal*, high statistics, error free distributions. For a given detector pair, the corrected distribution is calculated according to the expression (Msaki *et al* 1994):

$$D_{ijkl}^{PC} = \frac{\sum_{k,l=L}^{n} D_{ijkl}}{\sum_{k,l=L}^{n} \tilde{D}_{ijkl}} \tilde{D}_{ijkl} \qquad (2.33)$$

where D refers to either the measured emission data C_{ijkl}, the delayed randoms R_{ijkl} or the random corrected data T_{ijkl}^{R}. The data acquired in windows below some cutoff L where no useful signal is present should be discarded. The *ideal* distributions $\tilde{D}_{ijkl}$ taken as references must be derived from a suitable high statistics measurement. The underlying assumption of this approach is that after suppression of statistical fluctuations, the spectral shapes of emission or random data acquired in low and high statistics measurements would be identical. Thus, the variance of distributions with low statistics can be reduced by imposing the shape of the *ideal* distributions. The success of this method depends on the relevance of the chosen *ideal* distribution to a given study.

Weighted Smoothing (WS):

Weighted smoothing is the simplest and most widely used direct method for reducing variance. Smooth distributions are obtained in the energy space by weighted summations of the form:

$$D_{ijkl}^{WS} = \sum_{u=k-\alpha}^{k+\alpha} \sum_{v=l-\alpha}^{l+\alpha} W_{uv} D_{ijuv} \tag{2.34}$$

where $2\alpha+1$ is the size of the smoothing kernel W_{uv}. The choice of the kernel size depends on the dimensions and the characteristics of the data to be processed. Since the useful size of the energy space for the multispectral PET data used in this work is typically limited to 13×13, a kernel size of 3×3 (α=1) was used. The smoothing kernel W is thus given by:

$$W = \left(\frac{1}{b+2}\right)^2 \begin{pmatrix} 1 & b & 1 \\ b & b^2 & b \\ 1 & b & 1 \end{pmatrix} \tag{2.35}$$

The resolution of W can be adjusted by assigning a suitable weight to the parameter b. Thus, the effectiveness of this technique can be adapted to reach a compromise between noise reduction in regions with low count densities and spectral shape integrity of the photopeak. In practice, the selection of b will be based on statistics and, for this reason, the *WS* technique is considered partially *a priori*.

Ideal Low-pass Filter (ILF):

For a given detector pair *(i,j)*, the reduction of statistical fluctuations in the energy matrix D_{ij} of one LOR can be achieved by scaling its 2-D Fourier Transform (FT) by an ideal low-pass filter and finding the inverse of the result:

$$D_{ij}^{ILF} = FT^{-1}\left\{\left[FT\left(D_{ij}\right)\right] ILF\right\} \tag{2.36}$$

ILF is ideal since its intensity is 1.0 below some cutoff frequency ν_c. The choice of this cutoff frequency is also a compromise between noise reduction and photopeak shape distortion which can be adapted to the measured data.

Mean Median (MM) smoothing:

This is an adaptive smoothing technique which preferentially provides significant smoothing in uniform regions and selective noise reduction in regions containing edges and other structural information. The processed distribution is given by (Maeda and Murata 1987, Furuie and Mascarenhas 1992, Mascarenhas *et al* 1993):

$$D^{MM}_{ijkl} = \beta_{kl}\hat{D}_{ijkl} + (1-\beta_{kl})\overline{D}_{ijkl} \qquad (2.37)$$

where β_{kl} is the ratio of local variance in a moving window relative to the maximum variance in the data set *(k,l)*, $\hat{D}_{ijkl}$ is the local median and $\overline{D}_{ijkl}$ is the local mean in the moving window. For the same reason mentioned above, a window size of 3×3 was chosen in this work. Except for the window size, no other *a priori* assumption needs to be made when using the *MM* smoothing technique.

Variance reduction in the projection space

Normalization can be considered as a variance reducing technique in projection space since it suppresses the systematic error $(\sigma^D_{kl})^2$ resulting from non-uniform detector efficiencies.

Normalization in multispectral acquisition is effected by multiplying the measured data D_{ijkl} by factors F^*_{ijkl} compensating for the variations of detection efficiency in projection space and of spectral symmetry in energy space (Msaki et al 1993a):

$$D^N_{ijkl} = D_{ijkl}F^*_{ijkl} \qquad (2.38)$$

where: $$F^{*}_{ijkl} = 0.5\left(\overline{C_{kl}} + \overline{C_{lk}}\right) / C^{B}_{ijkl}$$

C^{B}_{ijkl} are counts derived from a suitable efficiency measurement. Note two important features of the normalization procedure: first, it is expected to have little or no effect on the statistical variance, since the factors F^{*}_{ijkl} are usually derived from blank measurements (e.g. plane source) with high counting statistics (Stearns and Wack 1993); second, application of the equation (2.32) can be done independently on emission (C_{ijkl}) and random (R_{ijkl}) data or collectively on the random event subtracted distribution (C_{ijkl}-R_{ijkl}) since the multiplicative factors F^{*}_{ijkl} are common to both distributions. Further reduction of the statistical variance by smoothing in the projection space was not attempted in this work because of its potential degradation effects on spatial resolution.

Variance reduction by optimal pre-processing sequence

Permutation of R, N and S operations:

In conventional PET, pre-processing procedures normally consist of subtraction of random events (R) followed by normalization of detector efficiency (N). Since collective (RN) and independent (NR) normalization of the emission and random data sets are equivalent, the question of an optimal sequence has not arisen in the past. However, the introduction of energy space data smoothing (S) applied to both emission and random data in multispectral PET imaging gives rise to several possible pre-processing sequences. As in conventional PET, the order in which R and N are performed is not important since normalization is multiplicative. Similarly, as long as the same smoothing function is applied to both the emission and random data sets, the order in which S and R are performed, i.e. independent (SR) and collective (RS) smoothing, is only important from the computational point of view, since smoothing is equivalent to a convolution. The combination of these properties leads to two distinct protocols in which the variance reducing operations (N and S) are permuted about the noise generating operation (R): SNR≡SRN≡RSN and NSR≡NRS≡

RNS. Only the order in which the variance reduction in the energy space (S) and the projection space (N) is performed distinguishes the two protocols. Note that the computational burden is increased whenever N or S occurs before R in the sequences, since the N and S processes have then to be performed in parallel on both the emission and the random data sets. Assuming that *no smoothing* is an alternative correction, then only the collective RN, RSN and RNS sequences, shown in figure 2.3, need to be investigated.

Preferential smoothing

Applying the same smoothing function (S) to both random and emission data neglects the statistical differences which exist between the two distributions. Since statistics of the random data set is usually poorer than that of the emission data set (~ 16%), the use of a preferential smoothing function may be beneficial. Smoothing of the random data set alone (S') and distinct smoothing of the emission and random data sets (S") have been considered as variants of S in the pre-processing sequences shown in figure 2.3 and their results were investigated in this work.

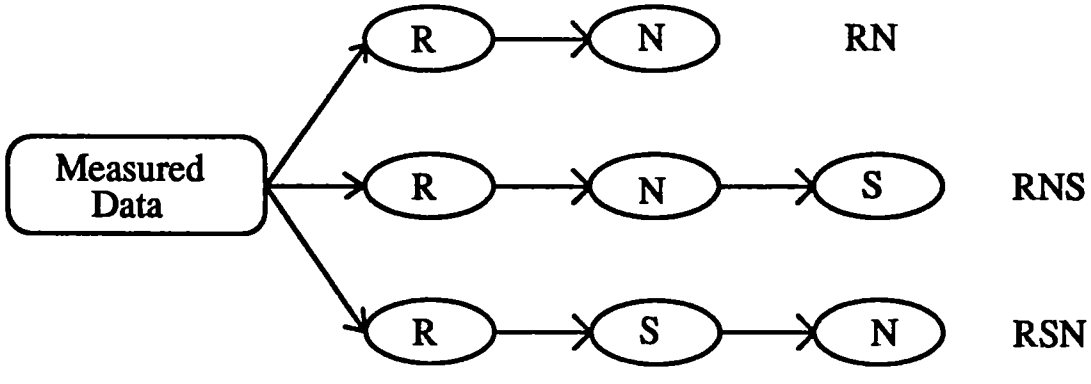

Figure 2.3. Permutations of three data pre-processing procedures: random subtraction (R), normalization (N) and spectral smoothing (S). S also holds for protocols involving smoothing random data only (S') and distinct smoothing of the emission and random data set (S").

Global Scatter Correction (GSC) method

Definition of data set

For a system with multispectral acquisition capability, the energy is an additional variable besides the conventional position index for the acquired data. The complete multispectral data set can be expressed as a matrix P of K rows and L columns. K is the total number of Line Of Responses (LORs) in each energy frame and L the total number of energy frames. Correspondingly, the row and column indices are spatial and energy variables. A row of the matrix corresponds to the energy spectrum of the LOR at the position of the row index. A column corresponds to an energy frame obtained by rearranging the LORs in the sinogram of a given energy window into lexicographic order (figure 2.4).

Assuming that the energy frame measured at the point e_l $(l = 1,2,\ldots,L)$ is written as a column vector $\rho(e_l)$, the multispectral data matrix P can be expressed as:

$$P = [\rho(e_1) \quad \rho(e_2) \quad \cdot \quad \cdot \quad \rho(e_L)] \tag{2.39}$$

where each energy frame $\rho(e_l)$ is the collection of LORs measured at energy e_l.

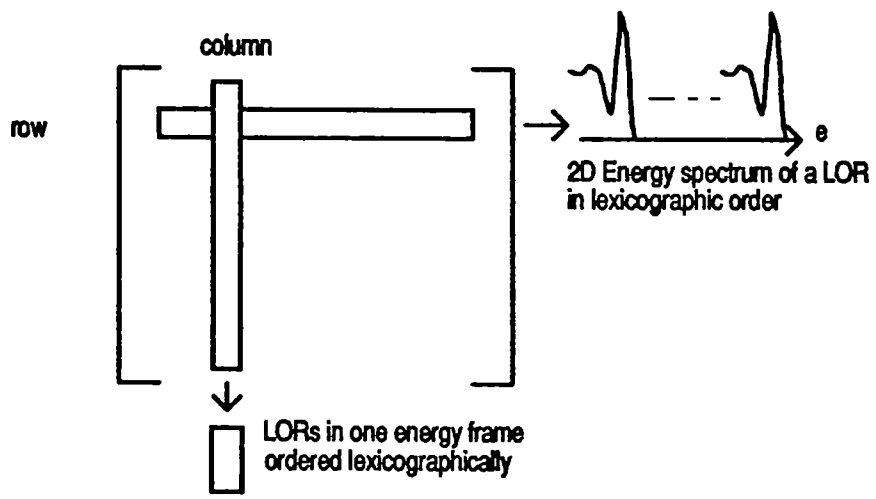

Figure 2.4. Multispectral data set reorganized in a 2D matrix.

According to equation (2.15), $p_m(e) = \varphi(e) + s_d(e) + s_o(e)$, so P can also be written as the summation of geometric, detector and object scattered components:

$$P = \Gamma + S_d + S_o$$

where Γ, S_d and S_o are the data matrices corresponding to the geometric $\varphi(e)$, detector scatter $s_d(e)$ and object scatter $s_o(e)$ components. Let $S = S_d + S_o$ to represent the total scatter component, then $P = \Gamma + S$. In nuclear medicine measurements, the quantum noise N is an important factor which affects the quality of measured data. It was not included in the energy dependent scatter degradation model in order to simplify the model and focus on the energy dependence problem of scatter components. In fact, the quantum noise or statistical fluctuations for data acquired in multispectral mode is even more critical because the counts are distributed in the energy space. Including the noise term N in the data formation, then

$$P = \Gamma + S + N \tag{2.40}$$

Principal Component Analysis (PCA)

PCA is the spectral analysis step of the GSC method. Originally, this is a technique for reducing the dimensionality of a data set in which there is a large number of correlated variables, while retaining as much as possible of the information presenting in the initial data set (Jolliffe 1986). In this work, the reduction of data dimensionality is achieved along with the suppression of noise and scatter.

PCA is realized by first transforming the original energy frames into a new set of components which are orthogonal to each other and classified in decreasing order in terms of information content. Then only the first few components, the principal components, are preserved as representative of the original data. Computation of the

principal components has been formulated as the solution of an eigenvalue-eigenvector problem for a positive-semidefinite symmetric matrix by Pearson (1901) and Hotelling (1933).

Singular Value Decomposition (SVD)

There are several algorithms and commercial programs available for performing PCA. The algorithm and program used in this work are Singular Value Decomposition (SVD, Wilkinson, 1965) and the library function of PV_WAVE Command Language (Precision Visuals Inc. 1991, Press *et al* 1990). Decomposing the multispectral data set P by SVD, we have:

$$P = \Phi \mathring{\lambda}^{1/2} A^{'} \tag{2.41}$$

where $\Phi = [\phi_1 \quad \phi_2 \quad \cdot \quad \cdot \quad \phi_L]$ is a *vector orthogonal* matrix, ϕ_l $(l = 1,2,\ldots L)$ are column vectors of length K. $A = \begin{bmatrix} a_{e_1,1} & a_{e_1,2} & \cdot & \cdot & a_{e_1,L} \\ a_{e_2,1} & a_{e_2,2} & \cdot & \cdot & \cdot \\ \cdot & \cdot & \cdot & \cdot & \cdot \\ \cdot & \cdot & \cdot & \cdot & \cdot \\ a_{e_L,1} & \cdot & \cdot & \cdot & a_{e_L,L} \end{bmatrix}$ is a $L \times L$ *orthonormal* matrix. It is the matrix which performs the transformation between the original energy frames and the new components. Assuming $A_{col}(l) = \begin{bmatrix} a_{e_1,l} \\ a_{e_2,l} \\ \cdot \\ \cdot \\ a_{e_L,l} \end{bmatrix}$, then $A = [A_{col}(1) \quad A_{col}(2) \quad \cdot \quad \cdot \quad A_{col}(L)]$;

$D^{1/2} = \begin{bmatrix} \lambda_1^{1/2} & & & & \\ & \lambda_2^{1/2} & & & \\ & & \cdot & & \\ & & & \cdot & \\ & & & & \lambda_L^{1/2} \end{bmatrix}$ is a $L \times L$ diagonal matrix, λ_l's are *ordered* such

that $\lambda_1 \geq \lambda_2 \geq \ldots \geq \lambda_L$ and $\mathrm{var}\left[PA_{col}^{'}(l)\right] = \lambda_l$, where var( ) represents variance. Rewriting equation (2.41) as:

$$P = \left[\rho(e_1) \;\; \rho(e_2) \;\; \cdot \;\; \cdot \;\; \rho(e_L)\right] = \sum_{l=1}^{L} \phi_l \lambda_l^{1/2} A_{col}^{'}(l) \tag{2.42}$$

where

$$\rho(e_i) = \sum_{l=1}^{L} \phi_l \lambda_l^{1/2} a_{e_i,l} \tag{2.43}$$

These two equations are the SVD algorithm used in this work. Figure 2.5 shows the structure of one principal component.

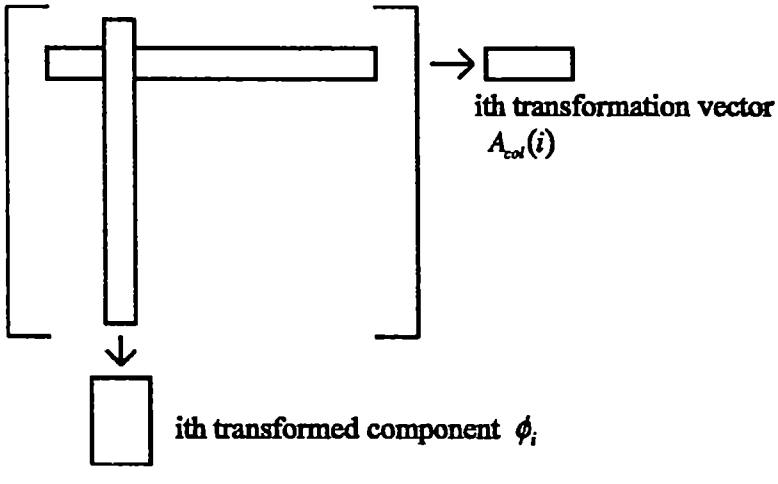

Figure 2.5. Illustration of the *i*th principal component of the multispectral data set obtained by performing Singular Value Decomposition (SVD).

Spectral Decomposition Theorem (SDT)

Assuming that P has a known covariance matrix, $\Sigma = P^{'}P$, the (i,j)th element of Σ is the covariance between $\rho(e_i)$ and $\rho(e_j)$ when $i \neq j$, and the variance of $\rho(e_i)$ when $i = j$. Then λ_i corresponds to the *i*th eigenvalue of Σ, the corresponding *i*th eigenvector is

$A_{col}(i)$, such that $\Sigma A_{col}(i) = \lambda_i A_{col}(i)$ (Jolliffe, 1986). According to the Spectral Decomposition theorem (Mardia *et al* 1979),

$$\Sigma = \sum_{l=1}^{L} \lambda_l A_{col}(l) A_{col}^{'}(l) \tag{2.44}$$

Since A is an orthonormal matrix, i.e. $A_{col}^{'}(l) A_{col}(l) = 1$, then

$$\begin{aligned} trace(\Sigma) &= \sum_{l=1}^{L} \lambda_l trace\left[A_{col}(l) A_{col}^{'}(l)\right] \\ &= \sum_{l=1}^{L} \lambda_l trace\left[A_{col}^{'}(l) A_{col}(l)\right]. \\ &= \sum_{l=1}^{L} \lambda_l \end{aligned} \tag{2.45}$$

The variance λ_l represents the relative importance of the lth principal component ϕ_l, as the λ_l's are ordered from large to small. If the frames of P have substantial correlation among them, then the first few principal components will account for most of the variation in the original data set P. Hence forth the first few principal components form the best estimate of the original data set (Chapter 1, Jolliffe 1986, Mardia *et al*, 1979). The dimensionality reduction is thus achieved by keeping only the first few principal components of P as its estimate ($\hat{P}$):

$$\hat{P} = \sum_{l=1}^{I} \phi_l \lambda_l^{1/2} A_{col}^{'}(l) \quad I << L \tag{2.46}$$

Maximum dimensionality reduction for MSPET

As $P = \Gamma + S + N$, the variance-covariance matrix for P is written as:

$$\begin{aligned}\Sigma &= P^{'}P \\ &= (\Gamma+S+N)^{'}(\Gamma+S+N) \\ &= \Gamma^{'}\Gamma+S^{'}S+N^{'}N+S^{'}\Gamma+\Gamma^{'}S \\ &\quad +N^{'}\Gamma+\Gamma^{'}N+N^{'}S+S^{'}N\end{aligned} \tag{2.47}$$

Since statistical fluctuation is *isotropically* distributed in space and has a *zero average*, the covariance between Γ and N, S and N can be neglected. Thus we have:

$$\Sigma = \Gamma^{'}\Gamma+S^{'}S+N^{'}N+S^{'}\Gamma+\Gamma^{'}S \tag{2.48}$$

Using var() and cov() to represent variance and covariance terms, then equation (2.48) becomes:

$$\begin{aligned}\mathrm{var}(P) &= \mathrm{var}(\Gamma)+\mathrm{var}(S)+\mathrm{var}(N) \\ &\quad +\mathrm{cov}(\Gamma^{'},S)+\mathrm{cov}(S^{'},\Gamma)\end{aligned} \tag{2.49}$$

As mentioned earlier, $\mathrm{var}\left[PA_{col}^{'}(l)\right] = \lambda_l$, where λ_l is the lth maximum eigenvalue of Σ and $\mathrm{var}\left[PA_{col}^{'}(l)\right]$ corresponds to the variance of the lth principal component. So there is:

$$\mathrm{var}\left[PA_{col}^{'}(1)\right] = \lambda_1 \tag{2.50}$$

Since $\lambda_1 = \mathrm{var}\left[PA_{col}(1)\right] = A_{col}^{'}(1)\mathrm{var}(P)A_{col}(1)$, using knowledge of equation (2.49), we have:

$$\begin{aligned}\lambda_1 &= A_{col}^{'}(1)[\mathrm{var}(\Gamma)+\mathrm{var}(S)+\mathrm{var}(N) \\ &\quad +\mathrm{cov}(\Gamma^{'},S)+\mathrm{cov}(S^{'},\Gamma)]A_{col}(1)\end{aligned} \tag{2.51}$$

As Γ is the geometric component, *all the energy frames of it must have the same structure.* In other words, Γ is only one component distributed over energy space. This can be expressed as:

$$\Gamma = \phi_\Gamma \lambda_\Gamma^{1/2} a_\Gamma^{'} \tag{2.52}$$

where a_Γ is a column matrix similar to $A_{col}(i)$, it corresponds to the relative proportion of ϕ_Γ in energy space. So the first component in equation (2.51) is:

$$A_{col}^{'}(1)\mathrm{var}(\Gamma)A_{col}(1) = \lambda_\Gamma A_{col}^{'}(1)a_\Gamma a_\Gamma^{'} A_{col}(1) \tag{2.53}$$

$A_{col}^{'}(1)a_\Gamma$ and $a_\Gamma^{'}A_{col}(1)$ are both scale factors and equal to the inner product of $A_{col}(1)$ and a_Γ.

$$\begin{aligned} A_{col}^{'}(1)\mathrm{var}(\Gamma)A_{col}(1) &= \lambda_\Gamma A_{col}^{'}(1)a_\Gamma A_{col}^{'}(1)a_\Gamma \\ &= \lambda_\Gamma \left[A_{col}^{'}(1)a_\Gamma\right]^2 \end{aligned} \tag{2.54}$$

As $A_{col}^{'}(1)A_{col}(1) = a_\Gamma^{'}a_\Gamma = 1$ and $A_{col}^{'}(1)a_\Gamma a_\Gamma^{'}A_{col}(1) \le A_{col}^{'}(1)A_{col}(1)a_\Gamma^{'}a_\Gamma = 1$, therefore

$$A_{col}^{'}(1)\mathrm{var}(\Gamma)A_{col}(1) = \lambda_\Gamma k_\Gamma^2 \qquad \text{where } 0 \le k_\Gamma = A_{col}^{'}(1)a_\Gamma \le 1 \tag{2.55}$$

Similar to equation (2.42), S and N can be decomposed by SVD:

$$\begin{aligned} X &= \Phi_X D_X^{1/2} A_X^{'} \\ &= \sum_{l=1}^{L} \phi_{X-l}\lambda_{X-l}^{1/2} A_{X-col}^{'}(l) \qquad \text{where } X = S,\ N \end{aligned} \tag{2.56}$$

Since the columns of A, $A_{col}(i)\, i = 1,2,\cdots L$, form a basis for L-dimensional space, therefore

$$A_{X-col}(l) = \sum_{j=1}^{L} C_{X-jl} A_{col}(j) \tag{2.57}$$

where C_{X-jl} $(X = S, N;\ j = 1,2, \ldots L;\ l = 1,2, \ldots L)$ are appropriately defined constants. Now equation (2.56) becomes:

$$X = \sum_{l=1}^{L} \phi_{X-l} \lambda_{X-l}^{1/2} \left[\sum_{j=1}^{L} C_{X-jl} A_{col}^{'}(j) \right] \tag{2.58}$$

Using the knowledge that Φ_X is orthonormal vector and A orthonormal matrix, the second or third components in equation (2.51) is:

$$\begin{aligned} & A_{col}^{'}(1)\mathrm{var}(X)A_{col}(1) \\ & = A_{col}^{'}(1)\mathrm{var}\left\{ \sum_{l=1}^{L} \phi_{X-l} \lambda_{X-l}^{1/2} \left[\sum_{j=1}^{L} C_{X-jl} A_{col}^{'}(j) \right] \right\} A_{col}(1) \\ & = \sum_{l=1}^{L} \lambda_{X-l} C_{X-1l}^{2} \end{aligned} \tag{2.59}$$

The right side of equation (2.59) can be explained as the variance of the X weighted by the projections of $A_{X-col}(l)$ $(l = 1,2, \ldots L)$ on $A_{col}(1)$. Similarly the covariance term in equation (2.51) is:

$$
\begin{aligned}
&A_{col}^{'}(1)\mathrm{cov}(\Gamma^{'},S)A_{col}(1) \\
&= A_{col}^{'}(1)\left[a_{\Gamma}\lambda_{\Gamma}^{1/2}\phi_{\Gamma}^{'}\right]\left\{\sum_{l=1}^{L}\phi_{S-l}\lambda_{S-l}^{1/2}\left[\sum_{j=1}^{L}C_{S-jl}A_{col}^{'}(j)\right]\right\}A_{col}(1) \\
&= k_{\Gamma}\lambda_{\Gamma}^{1/2}\left\{\sum_{l=1}^{L}\phi_{\Gamma}^{'}\phi_{S-l}\lambda_{S-l}^{1/2}C_{S-1l}\right\}
\end{aligned}
\tag{2.60}
$$

and

$$
A_{col}^{'}(1)\mathrm{cov}(S^{'},\Gamma)A_{col}(1) = k_{\Gamma}\lambda_{\Gamma}^{1/2}\left\{\sum_{l=1}^{L}\phi_{\Gamma}^{'}\phi_{S-l}\lambda_{S-l}^{1/2}C_{S-1l}\right\} \tag{2.61}
$$

So the two covariance components are the inner product of Γ and S weighted by the projection of $A_{S-col}(l)$ $(l=1,2,\ \ldots\ L)$ on $A_{col}(1)$. Replacing the terms in equation (2.51) by corresponding expressions obtained in equations (2.55-61), we have:

$$
\begin{aligned}
\lambda_1 = {} & \lambda_{\Gamma}k_{\Gamma}^2 + \sum_{l=1}^{L}\lambda_{S-l}C_{S-1l}^2 + \sum_{l=1}^{L}\lambda_{N-l}C_{N-1l}^2 \\
& +2k_{\Gamma}\lambda_{\Gamma}^{1/2}\left\{\sum_{l=1}^{L}\phi_{\Gamma}^{'}\phi_{S-l}\lambda_{S-l}^{1/2}C_{S-1l}\right\}
\end{aligned}
\tag{2.62}
$$

When the variance of the scatter and noise components is much less than that of geometric component (Bentourkia *et al* 1995a, 1995b, Bergström *et al* 1983, Chan *et al* 1983, King *et al* 1981), the first principal component of P (ϕ_{1pc}), which is responsible for the largest variance among the components of the new data set, will be mainly determined by the geometric component Γ. So the vectors ϕ_1 and ϕ_{Γ}, and equivalently $A_{col}(1)$ and a_{Γ}, have very close direction in multi-dimensional space, and the approximation: $k_{\Gamma} = A_{col}^{'}(1)a_{\Gamma} \approx 1$ can be made. So there is:

$$\lambda_1 = \lambda_\Gamma + \sum_{l=1}^{L} \lambda_{S-l} C_{S-1l}^2 + \sum_{l=1}^{L} \lambda_{N-l} C_{N-1l}^2 + 2\lambda_\Gamma^{1/2} \left\{ \sum_{l=1}^{L} \phi_\Gamma^{'} \phi_{S-l} \lambda_{S-l}^{1/2} C_{S-1l} \right\} \tag{2.63}$$

This is to say that the ϕ_{1pc} contains all information related to the primary structure in data set P, thus maximum dimensionality reduction can be achieved by preserving this component only. As an example, the relative importance of the principal components for a line source is shown in figure 2.6.

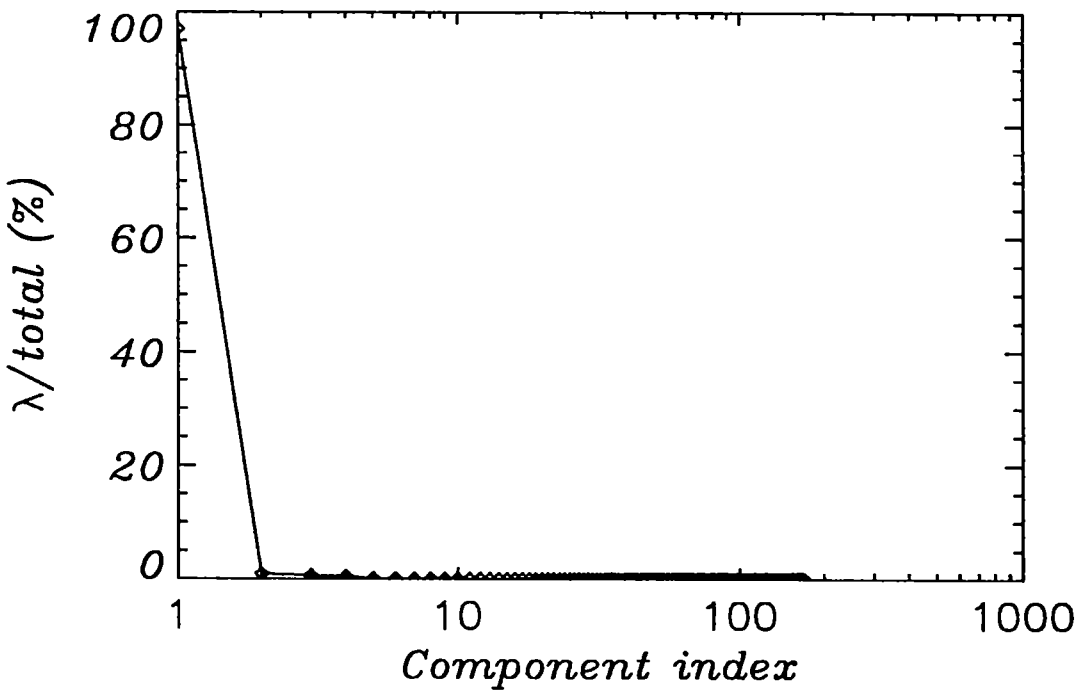

Figure 2.6. The relative importance of the principal components in terms of their variance for a line source located at 5 cm from the center of a acrylic cylinder, $\lambda_1/(total\ variance) = 97\%$.

In the case where the geometric component Γ is not prevalent, the scatter and noise components contribute a non-negligible proportion to the total variance and the

approximation: $k_\Gamma = A'_{col}(1)a_\Gamma \approx 1$ is not valid anymore. However, if the variance of the ϕ_{1pc} is dominant in the total variance and no other component contains a significant fraction of the total variance, i.e. all the other components have about the same variance intensity, the maximum dimensionality reduction can still be achieved by preserving the ϕ_{1pc} only. The reason is that the less correlated scatter and noise contributions are distributed over all the components, whereas most of the geometric component is concentrated in the ϕ_{1pc} because of its strongly correlated nature. Under this situation, the Γ may not be fully preserved as in equation (2.63), but the benefit is the higher data quality achieved by removing more scatter and noise at the cost of small amount of Γ. This is illustrated in figure 2.7 where the relative importance of the principal components is plotted for hot spot phantom measurement.

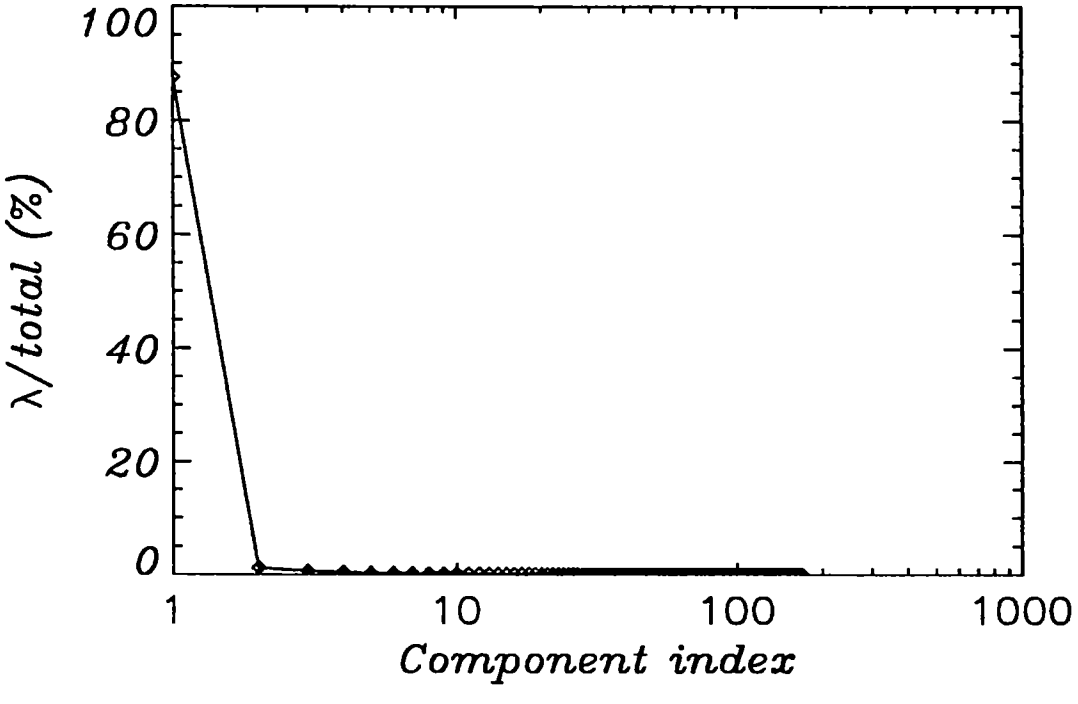

Figure 2.7. Same as figure 2.6 for hot spot phantom measurement, $\lambda_1/(total\ variance) = 88\%$.

If several principal components carry significant fractions of the total variance, they should all be preserved in order to retain useful information. However, this was not the case observed in our measurements.

Calculation of the ϕ_{1pc}

The sum of all energy frames equals to the data set acquired in a broad window. From equation (2.42), we have:

$$\sum_{e_i} \rho(e_i) = P(BW) = \sum_{l=1}^{L} \left[\phi_l \lambda_l^{1/2} \sum_{e_i} a_{e_i,l} \right] \tag{2.64}$$

This equation reflects one important feature of the spectral decomposition theorem with respect to the physical meaning of the new principal components: the recombination of new components forms the original data set in broad window, the coefficient ($\sum_{e_i} a_{e_i,l}$) for each component is from the corresponding transformation vector ($A_{col}(l)$).

As the ϕ_{1pc} constitutes the best replacement of the whole data set P, according to equation (2.46),

$$\hat{P} = \phi_{1pc} = \phi_1 \cdot \lambda_1^{1/2} \cdot A_{col}^{\cdot} \Psi^{\cdot} \tag{2.65}$$

here ϕ_{1pc} is a $K \times L$ matrix. Each column of ϕ_{1pc} corresponds to its fraction in the corresponding energy frame and all the columns have the same structure (ϕ_1). Since multispectral acquisition and analysis is a means to process data, the final image formation data does not need energy information. So there is no need to keep distributing the ϕ_{1pc} over individual energy window after PCA, which we believe has achieved

optimal extraction of useful information in data. The ϕ_{1pc} can be regrouped into the broad energy window:

$$\phi_{1pc} = \phi_1 \cdot \lambda_1^{1/2} \cdot \sum_{l=1}^{L} a_{e_l,1} \tag{2.66}$$

Spatial convolution scatter correction

The projections of the ϕ_{1pc} and the corresponding original BW data of the centered line source are presented in figure 2.8. It is clear that although preserving only the ϕ_{1pc} reduces scatter background (projection tails) efficiently, scatter component still exists in the ϕ_{1pc} (see also equation 2.62). Further processing in the spatial domain is required to correct the scatter residue. The scatter kernel obtained from the ϕ_{1pc} of a line source measurement is used for this purpose.

Various scatter correction algorithms based on spatial analysis (Msaki *et al*, 1996) can be applied to the ϕ_{1pc}. The most current approach is to process the projections individually. Methods such as Convolution Subtraction or Deconvolution Restoration can be applied depending on the system configuration to give the optimal results. For instance, the Object scatter Subtraction and Detector scatter Restoration (OSDR) algorithm used for the high resolution PET system has been implemented as following:

$$\varphi = \left[\phi_{1pc} \otimes \left(\delta - f_o' h_o'\right)\right] \otimes FT^{-1}\left\{\frac{f_g' + f_d'}{f_g' + FT\left(f_d' h_d'\right)}\right\} \tag{2.67}$$

Statistical noise

The additional component N in equation (2.40) usually only carries a small proportion of the total image information in terms of variance. Because of its zero average value, quantum noise contributes to the ϕ_{1pc} without covariance contribution with Γ or S (equation 2.51). As statistical noise is unstructured in the sense that Poisson noise is isotropic and less correlated, it is expected that all the components obtained by decomposing N are more or less equal. In other words, there is no special structure which contains dominant component as is the case for highly correlated Γ component. Therefore, the component of N projecting on ϕ_{1pc} should have an intensity of about $1/\sqrt{L}$ the initial intensity of N. This means preserving only the first principal component can efficiently remove stochastic noise.

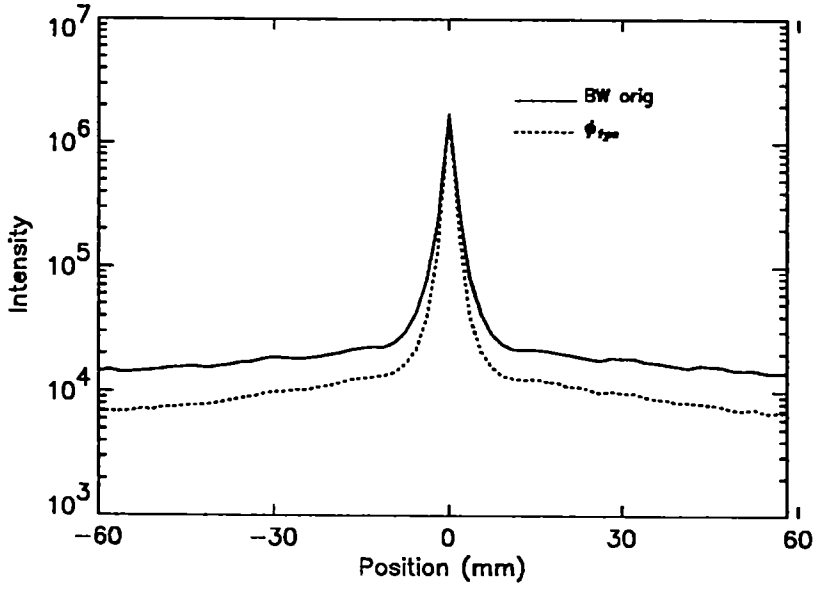

Figure 2.8. Comparing the original centered line source projection (BW orig) with its ϕ_{1pc} obtained by decomposing the oringinal data by SVD. Both projections are the sum of all incidences.

Chapter 3 Materials & Methods

A high resolution MultiSpectral PET (MSPET) scanner simulator has been developed in Sherbrooke (Lecomte *et al* 1990, 1992, 1993, 1994) to simulate a small animal PET imaging system. One important objective of this system is to achieve more efficient scatter correction by taking advantage of the energy information of the measured events. Unlike conventional PET, where the energy threshold decides if the event should be registered or rejected, MSPET registers coincident events in a series of 16 contiguous energy windows for each detector and thus defines a 2D energy spectrum for each line of response between coincident detectors.

Experimental setup

The schematic diagram of the simulator is shown in figure 3.1. Two lead slice collimators of 87.5 mm long were used to define a port diameter of 135 mm. The width of the shielding gap was adjusted at 10.5 mm to include two layers of detectors. Two opposite detector arrays, each consisting of eight dual-channel detector modules (Lecomte *et al* 1989, 1990), constitute the basic detection units of the system. One array represents 1/32 of a full animal ring tomograph having 310 mm in diameter. The modules consist of two individual detectors which can be operated independently. Each detector is made of one 3 mm x 5 mm x 20 mm BGO scintillator, coupled to one silicon Avalanche Photo Diode (APD) with a 3 mm x 3 mm active area. The scintillator center-to-center distance in slice is 3.8 mm and 5.5 mm axially. No interslice collimator was used. In multispectral mode, the data from only one layer of detectors could be acquired. The signal from the detectors were processed using purposely developed electronics (Lecomte *et al* 1993) and data were

recorded using a PC-based multispectral analyzer (PC/MCA MCard, APTEC, Downsview, Ontario) employed as an histogramming memory.

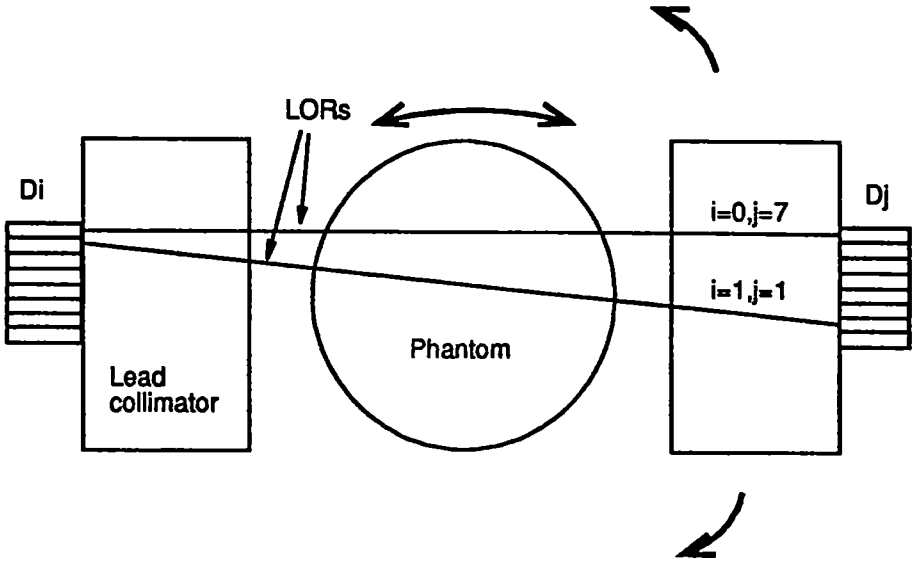

Figure 3.1. Schematic diagram of the Sherbrooke multispectral PET simulator. Each of the two opposing detector arrays consists of eight detectors. Each detector is capable of acquiring data in sixteen energy windows. One detector array and the phantom are rotated in a pre-determined sequence for tomographic data acquisition.

Fixed measurements were made using the opposite detector arrays set up as shown in figure 3.1. The projection space of the measured data in this case is a 8×8 matrix formed by the 64 coincidence LORs (see figure 2.2). Tomographic data were collected by scanning one of the detector arrays and by rotating the phantom in a series of 144 different positions. For a fixed ring size and field-of-view, the sequence of positions is predetermined (Héon *et al* 1993). The data acquired in each energy window were rebinned into projections and interpolated to a sample distance of 0.95 mm before reconstruction by Filtered Back Projection (FBP). A ramp filter was used for all image

reconstruction. Attenuation correction was not performed for several reasons. First, attenuation correction must be made after scatter correction, it should not influence the comparison of scatter correction methods. Second, the measurements of contrast, recovery factors were made at about the same distance from the center of the hot spot phantom, the difference of attenuation effect on different spots is negligible. Third, the phantom is relatively small (11 cm acrylic cylinder), the attenuation effect is less significant than large size objects.

Each set of measurements was repeated under the same conditions and for the same length of real time to measure the randoms by the delayed time window method. With the source activities used in this work, the random fraction (random / total) was about 16%. Since detector signals were processed in parallel (Lecomte *et al* 1990, 1993), dead time losses were negligible even at the highest count rates encountered. Because of the significant dependence of APD gain on temperature, the system had to be operated in a temperature controlled environment in order to ensure a very stable (maximum variation<1°C) temperature at the detector site.

Multispectral acquisition was realized by digitizing the energy signals from each detector into 16 energy windows and storing them simultaneously with the LOR address defined by any two coincident detectors. Each contiguous energy window spans a range of about 43 keV with the threshold levels indicated in Table 3.1. The photopeak of each detector was centered between window 11 and 12.

A complete data set consists of 16x16 energy frames, which corresponds to k,l = 0,15 in figure 1.4. Only data with energy higher than 129 keV (k,l >=3) were kept for image formation considering the low signal-to-noise ratio at lower energy. The data acquired in

multispectral mode provided the flexibility for grouping the data into any desired window mode, such as Broad Window (BW), Conventional Window (CW) etc.

Phantom measurements

Several sets of measurement were made for testing the techniques proposed in this work. The acquisitions with fixed detector arrays were made for assessing the effectiveness of the energy space smoothing techniques and data pre-processing sequences. The tomographic measurements were used mainly for testing scatter correction methods.

Table 3.1. Lower and upper thresholds of multiple energy windows (each window is about 43 keV wide).

Window number	Threshold(keV)
0	0-43
1	44-86
2	87-129
3	130-172
4	173-215
5	216-258
6	259-301
7	302-344
8	345-387
9	388-430
10	431-473
11	474-516
12	517-559
13	560-602
14	603-645
15	646-688

Fixed acquisitions

Plane source

The emission scan from which the efficiency normalization factors were evaluated was acquired with a high activity (42 μCi/cm^2) plane source of ^{22}Na in air for 12 hours. From experience, this acquisition time is sufficiently long to consider statistical fluctuations in the normalization measurement negligible i.e. about 3% or less relative standard deviation (Msaki *et al* 1993a).

Flood source

The emission measurement and the associated delayed random coincidences were obtained from a cylindrical flood source of ^{22}Na, having a diameter of 110 mm and an activity concentration of 9.1 μCi/cc, for various acquisition times ranging from 2.5 minutes to 12 hours. This measurement was used to assess the effects of spectral smoothing on low statistics data in the energy and the projection spaces.

Line source

Measurements were obtained from a line source of ^{22}Na (0.84 mm effective diameter, 2.8 μCi/mm) placed at the center of an acrylic cylinder of diameter 110 mm. In this configuration, the LORs which pass through the source are such that $i=j$. The acquired data were rebinned into 15 parallel projection bins for each window pair. This measurement was used to evaluate the effects of spectral smoothing on spatial distribution.

Tomographic acquisitions

Line source measurements

Measurements were made using the same ^{22}Na line source at the center and at 50 mm from the center of a cylindrical phantom of diameter 110 mm and height 25.4 mm filled with water. Stationary and position-dependent scatter kernels were derived from the centered and off-centered line source projections, respectively (Bentourkia *et al* 1995a). Considering the low random contribution and the added statistical noise that would be introduced by random subtraction, no random correction was performed on these data

sets. Data were also acquired with the line source placed at 10 mm from the center of the cylindrical phantom in order to test the effects of the scatter corrections on spatial resolution.

Hot spot phantom measurements

The effects of scatter corrections on image quality in terms of relative sensitivity, contrast and activity recovery were evaluated from measurements performed with a hot spot phantom made of acrylic and having eight hollow cylinders of diameters varying from 2.0 to 22.7 mm filled with a water solution of ^{22}Na, as shown in figure 3.2. Compared to the very high spatial resolution of the system ($\approx$ 2.1 mm), the largest hot spot is big enough to produce significant amount of scatter events for assessing scatter correction methods.

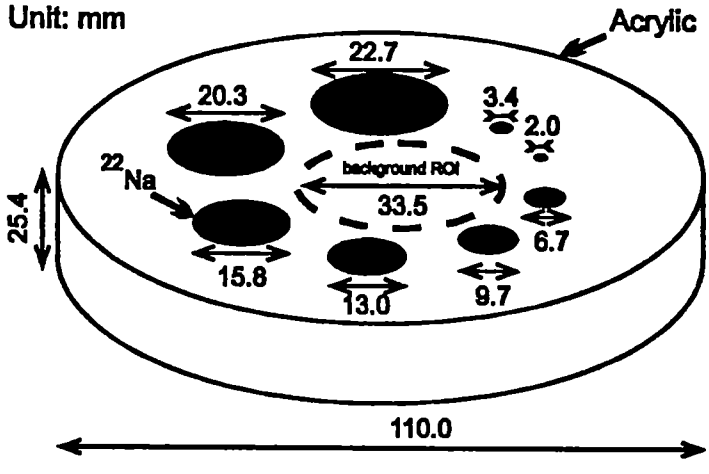

Figure 3.2. Hot spot phantom used to assess image quality with the various scatter processing methods. The eight hollow cylinders have their axes located at a distance of 28 mm from the center of the disk and were filled with a water solution of ^{22}Na. The shown background Region Of Interest (ROI) is the cold region used for image evaluation.

These tomographic measurements were also used to test data pre-processing techniques.

Data pre-processing techniques

Choice of smoothing parameters

Prior Constrained (PC) smoothing

The ideal distributions $\tilde{D}_{ijkl}$ taken as the reference energy spectrum for the emission and random data in equation (2.33) were derived from the 12-hour plane source measurement. While not typical of all cases, these spectral distributions were assumed to represent suitable estimates for most common situations. In the S smoothing protocols, the emission distribution C^*_{ijkl} was used as $\tilde{D}_{ijkl}$ to process both the emission and random data. In the protocols involving S' or S", the random distribution R^*_{ijkl} from the same 12-hour plane source measurement was used as $\tilde{D}_{ijkl}$ in smoothing the random data sets. The data acquired in windows below the cutoff L=3 where C_{ijkl} and R_{ijkl} become comparable were discarded. According to equation (2.29), this condition is satisfied when the data consists of no signal.

Weighted Smoothing (WS)

For consistent results, it was found necessary to adjust the value of the b parameter as a function of statistics in the weighting kernel of equation (2.35). Using the flood source measurements, the energy frames of each of the 64 LORs were smoothed by equation (2.34). The b parameter was allowed to vary from 1 to a maximum value such that the photopeak height in the high statistics spectra was reduced by no more than 5% after smoothing. The relative deviation between the smoothed energy data and the expected spectra derived from the 12-hour flood source measurement was estimated by the normalized mean-square error (*NMSE*), described below. Plots of *NMSE vs b* were made and the optimum b determined from the lowest *NMSE* value. The mean of these optimum b parameters as a function of statistics are shown in figure 3.3 for the emission and the random data from the flood source. For similar acquisition times, the energy spectrum of the randoms has more statistical fluctuations, but is also less sharply peaked around 511

keV. This is why the mean optimum *b* values for random data are sometimes lower than for emission data. The same *b* value derived from the emission data was used to process the emission and random spectra in the S protocol, while the optimum *b* value for randoms was used in the S' and S" protocols to smooth random coincidence spectra.

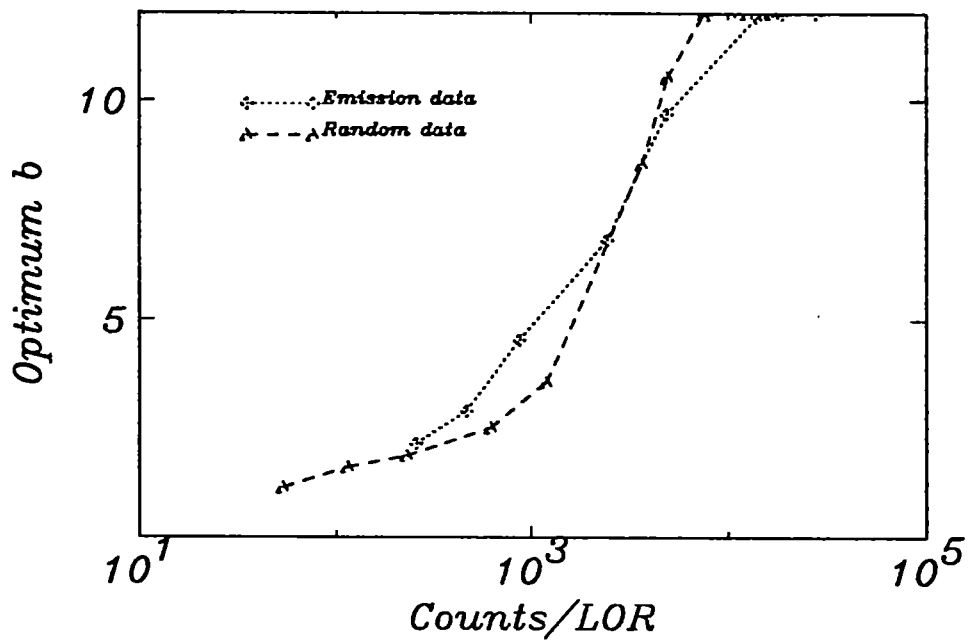

Figure 3.3. Optimum *b* parameter of the Weighted Smoothing (*WS*) kernel as a function of statistics for emission and random data.

Ideal Low-pass Filter (ILF)

In order to determine the optimum cutoff frequency of the ILF filter, the 2D energy spectra were first stripped of energy windows below the threshold L=3 and then 2D Fourier transformed. For typical intermediate and high statistics data, more than 90% of the Fourier spectrum is concentrated into the lower frequency range corresponding to $\nu \leq 3$ *window*$^{-1}$, as can be observed in figure 3.4 (*top right*). Eliminating higher frequencies with an ILF of cutoff frequency $\nu_c = 3$ *window*$^{-1}$ successfully suppresses statistical fluctuations in the 2D energy spectrum while preserving the photopeak shape (see figure 3.4, *bottom left*). Further investigation using *NMSE* showed that

$\nu_c = 3\ window^{-1}$ was the optimum choice in all cases, except for spectral smoothing of low statistics random data (< 8 counts/LOR) where a lower cutoff frequency was found more advantageous. The ILF cutoff frequency was set at $\nu_c = 3\ window^{-1}$ in all S protocols and was reduced to $\nu_c = 2\ window^{-1}$ as needed for random data distributions based on S' and S" smoothing.

Evaluation of variance reduction

The smoothing techniques and pre-processing sequences are expected to reduce variance by producing smoother distributions with shapes similar to that of corresponding reference distributions obtained in high statistics. The performance of the various protocols was evaluated by comparing the processed low count distributions, in both the energy and projection spaces, with the high statistics (*expected*) distributions using the following validation criteria.

Energy space

Ideally, spectral smoothing would remove statistical fluctuations in the 2D energy spectra associated with each LOR, thereby producing smoother distributions with

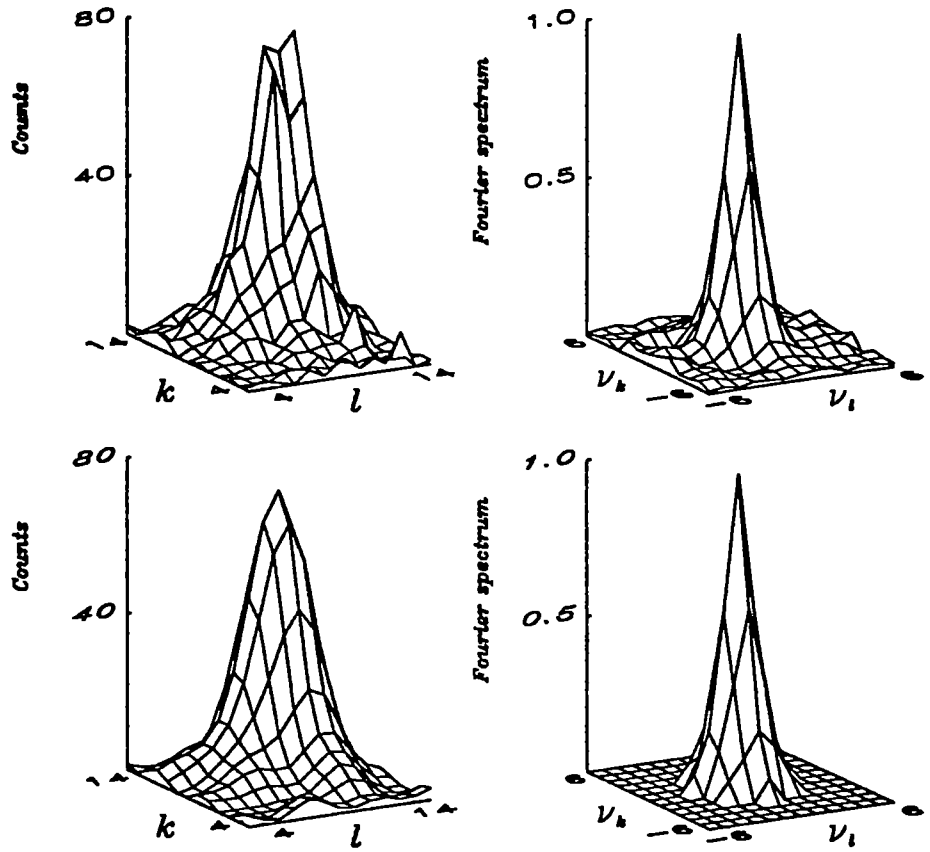

Figure 3.4. Illustration of the *ILF* smoothing algorithm for low statistics emission data from the flood source. *Clockwise*: 2D energy spectrum; Fourier spectrum of the 2D energy spectrum obtained by 2D Fourier transform; *ILF* filtered Fourier spectrum using $\nu_c = 3$ *window*$^{-1}$; *ILF* smoothed 2D energy spectrum obtained by inverse 2D Fourier transform.

shape approaching that obtained in high statistics. The normalized mean-square error given by (Mascarenhas*et al* 1993)

$$NMSE_{ij} = \frac{\sum_{k,l=L}^{n} \left(D^{s}_{ijkl} - D^{*}_{ijkl}\right)^2}{\sum_{k,l=L}^{n} \left(D^{s}_{ijkl}\right)^2} \qquad (3.1)$$

was used to assess the extent to which the smoothed distributions D^{s}_{ijkl} (where S holds for *PC*, *WS*, *ILF* and *MM*) in the energy space matched the shape of the expected energy spectra D^{*}_{ijkl} obtained in high statistics. These reference distributions were obtained from the corresponding 12-hour flood source measurement and normalized to the number of counts in the smoothed distributions.

Projection space

In principle, the corresponding index $NMSE_{kl}$ can be used to assess similar effects in projection space. However, in the case of a uniform phantom where the same count density is expected for all LORs, a measure of the fluctuations about the mean is preferred. For a given window pair *(k,l)*, such fluctuations about the mean count $\overline{D_{kl}}$ in the projection space is simply given by the relative standard deviation:

$$\%SD_{kl} = 100\frac{\sigma_{kl}}{\overline{D_{kl}}} \tag{3.2}$$

Spatial distribution

In order to assess the effects of spectral smoothing on the event spatial distribution in projection space, the data acquired from the line source with the fixed detector arrays were rebinned into 15-bin parallel projections for each window pair *(k,l)*. The expected projection is a sharp peak aligned to the source location and surrounded by a flat background. Due to the limited number of points in these projections, the full-width-at-half-maximum (FWHM) is not appropriate for estimating resolution. A more suitable index which is less sensitive to statistical fluctuations and which takes the whole spread function into consideration is the auto-correlation width, defined as:

$$R_w = \left\{\sum_p C_{pw}\right\}^2 \Big/ \sum_p C_{pw}^{\,2} \tag{3.3}$$

where C_{pw} is the count number in projection bin p and energy window index w, $w = (16 - L) * (k - L) + (l - L)$, assuming a lower energy threshold such that $k,l \geq L$. This concept of auto-correlation width was used previously to measure the width of line spread function in projections (Lecomte *et al* 1984, Schmitt *et al* 1986).

Another index which is more sensitive to changes in the background is the weighted projection deviation (*WPD*):

$$WPD = \sum_{pw} \{(p - p_c) * C_{pw}\}^2 \Big/ \sum_{pw} C_{pw}^{\ 2} \qquad (3.4)$$

The central projection bin p_C corresponds to the location of the source in the projection. A successful variance reduction protocol is expected to yield *WPD* values closer to the limit obtained in high statistics.

Scatter correction

Scatter kernels

Nonstationary kernels for object and detector scatter in all window modes were extracted from the *off-center* line source measurement (Bentourkia *et al* 1995a). The *stationary* scatter kernels were extracted from the projections of the *centered line source summed over all incidence angles.* The energy dependence for both stationary and nonstationary kernels was obtained by deriving the kernels in each individual energy window, as described elsewhere (Bentourkia *et al* 1995b).

Scatter correction protocols

Window modes

In order to evaluate the proposed Multispectral Frame-by-frame (MF) convolution and Global Scatter Correction (GSC) methods, the acquired multispectral data were regrouped into four window modes: Conventional Window (CW), Broad Window (BW), Multi-Frame (MF) and MultiSpectral (MS) modes. The CW mode was accomplished by summing all acquired data within the energy range 344 - 658 keV. In the BW mode, the sum was extended to include data down to the lower threshold of 129 keV. The Multispectral Frame-by-frame (MF) mode was implemented differently for stationary and nonstationary scatter corrections in order to compensate for the effect of low statistics in individual energy frames: in the stationary correction, all multiple energy windows over the same energy range as for BW were used; in the nonstationary correction, only two energy windows set to 129 - 429 keV and 430 - 658 keV were used. When MF was performed in combination with multispectral data pre-processing technique (RNS), the multispectral data set were first smoothed in the energy space and then regrouped into four designated energy frames (two energy windows for each detector). The raw multispectral data forms the MS mode.

Protocols

All acquired data were corrected for random coincidences and normalized for detection efficiency (Msaki *et al* 1993a) unless otherwise specified. The four energy window modes (CW, BW, MF and MS) and the two sets of scatter kernels (stationary and nonstationary) formed eight *major* scatter correction protocols. The combination of data pre-processing (including spectral smoothing) with stationary and nonstationary MF formed another protocol. The data in the CW and BW modes without scatter correction, as well as the MS data after spectral analysis (PCA), were evaluated as reference.

Indices for assessing image quality

The ability of the techniques to improve image quality was assessed by indices of resolution, contrast, quantitative accuracy and noise characteristics.

Resolution

The FWHM (full-width-at-half-maximum) and FWTM (full-width-at-tenth-maximum) of the reconstructed image of a line source at 10 mm from the center was used to evaluate the image resolution recovery. The resolutions were obtained by averaging over the radial and tangential profiles through the line source.

Relative sensitivity

The gain in sensitivity by using different window modes and scatter correction schemes was estimated as the ratio of overall counts in the processed to the corresponding CW images of the hot spot phantom.

Contrast

The percent image contrast was calculated from the reconstructed images of the hot spot phantom as:

$$IC(D) = 100 \times \frac{CP_h(D) - CP_c}{CP_h(D)} \qquad (3.5)$$

where CP_h is the average counts/pixel in selected region-of-interest (ROI) of the hot spots of diameter D and CP_C is the mean background counts/pixel in the background ROI at the center of the phantom (figure 3.2).

Relative recovery factor

The relative recovery factor is a measure of the loss of quantitative accuracy due to spillover effects resulting from scatter. It is evaluated with the hot spot phantom according to the formula:

$$RF(D) = 100 \times \frac{CP_h(D)}{CP_h(D_{max})} \qquad (3.6)$$

where the largest hot spot (D_{max}) is assumed to be free of errors associated with the partial volume effect. This index of activity recovery should not be confused with the Recovery coefficients extracted to correct for partial volume effects (Hoffman and Phelps 1986).

Relative standard deviation

The relative standard deviation (%STD) was evaluated as:

$$\%STD = 100 \frac{\sqrt{\sum_{i=1}^{N} (C_i - M)^2}}{M} \qquad (3.7)$$

where C_i is the number of counts in pixel i and N the total number of pixels in the ROI. This index was used to estimate the amplification of statistical noise resulting from the scatter corrections. The mean counts/pixel (M) and %STD were evaluated in ROIs defined in the second largest hot spot and in the background ROI (figure 3.2) of the hot spot phantom image.

Chapter 4 Results

Multispectral Frame-by-frame (MF) scatter correction & data pre-processing

Multispectral data pre-processing

Variance reduction in energy space

Smoothing methods

The performance of the different smoothing techniques was assessed by evaluating $NMSE_{ij}$ as a function of statistics for the flood source measurement, using the emission and random energy spectra obtained in the high statistics 12-hour measurement as the expected distributions. Results from detector pair (5,5) are presented in figure 4.1. Selected 2D energy spectra from the same detector pair, before and after *MM* smoothing, are compared in figures 4.2 and 4.3 for emission and random data, respectively. The choice of this detector pair was purely arbitrary and the conclusions reached below equally apply to other detector pairs.

As expected, the energy distributions are severely distorted in low statistics and the *NMSE* is high. These distortions become moderate in intermediate and absent in high statistics. The *PC* smoothing is observed to produce the best results since it fully recovers the expected spectral shapes irrespective of the counting statistics (*NMSE*≈0). All other smoothing techniques are successful at reducing the stochastic fluctuations in low to intermediate statistics emission data (<2000 counts/LOR), thereby producing smoothed distributions which are closer to the expected distributions. We also note that these techniques are more efficient at reducing variance in random data. This is a consequence of the flatter spectral distribution of the random data which suffers less distortions from the smoothing process than the emission data. These results suggested that independent

smoothing of the random and emission data would be a better option than collective smoothing. *ILF* smoothing is the most efficient overall, while *MM* smoothing converges to a higher value than the other methods in high statistics.

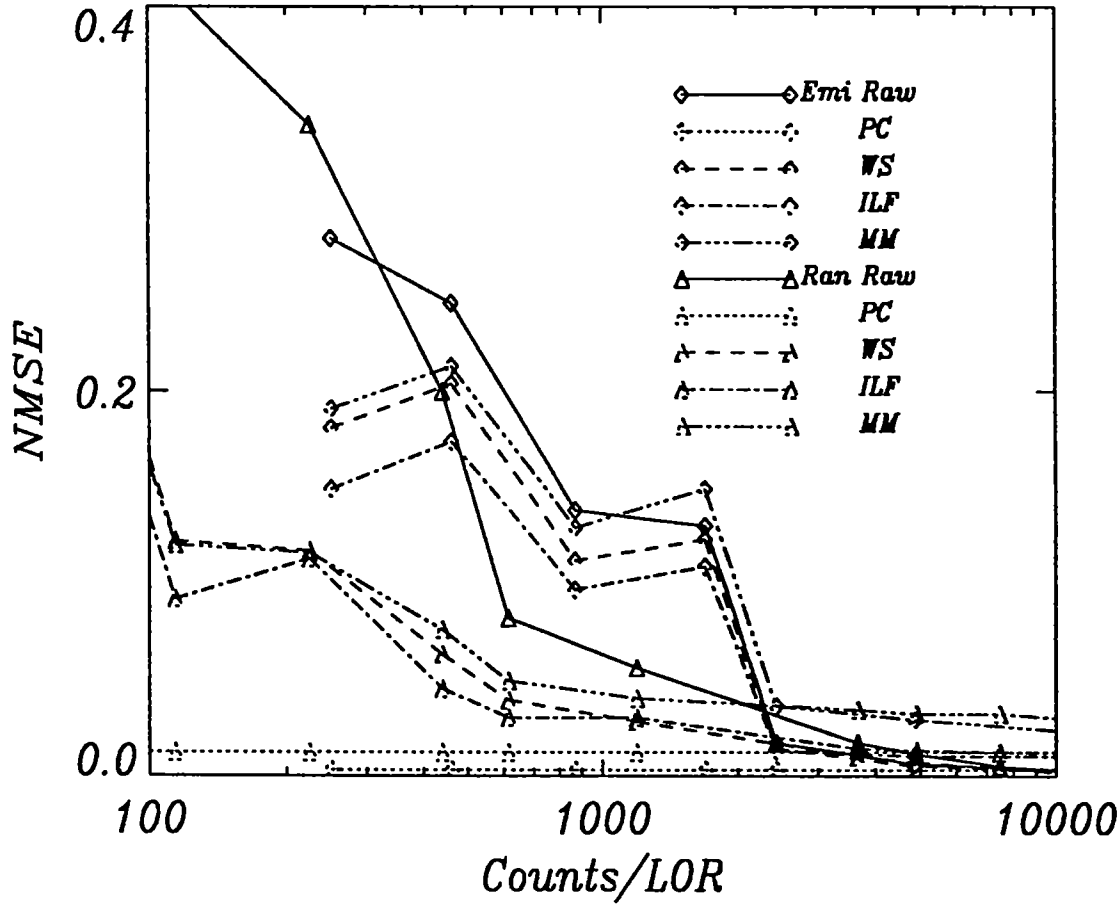

Figure 4.1 Normalized mean-square error (*NMSE*) as a function of statistics for different smoothing algorithms. The emission and random data from the flood source measured by detector pair (5,5) were used. The high statistics emission and random spectra were taken as the expected distributions in computing *NMSE*.

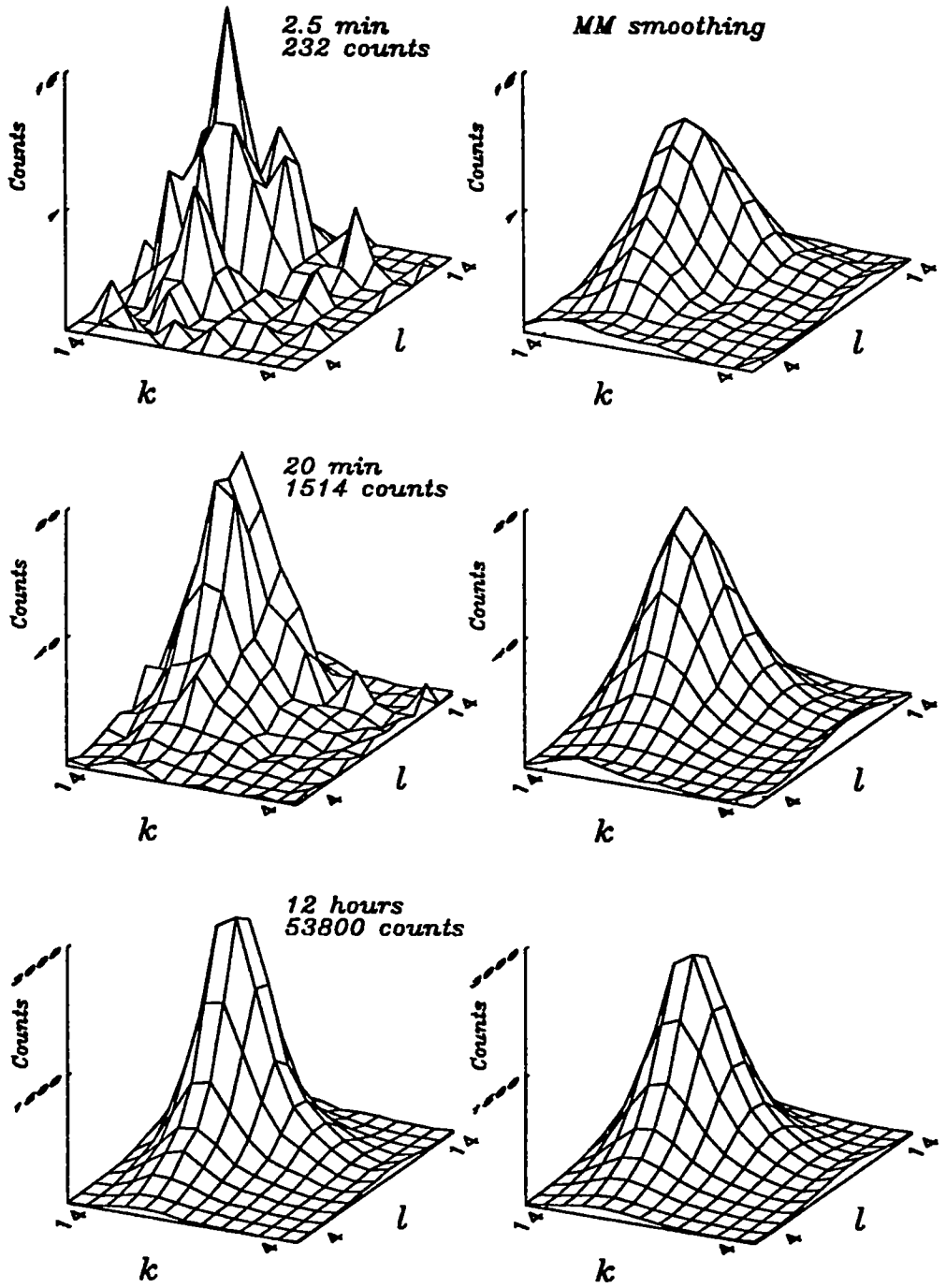

Figure 4.2. Variation of spectral shape and texture of the measured (*left*) and *MM*-smoothed (*right*) emission data acquired from the flood source by detector pair (5,5) in low (*above*), intermediate (*middle*) and high statistics (*bottom*).

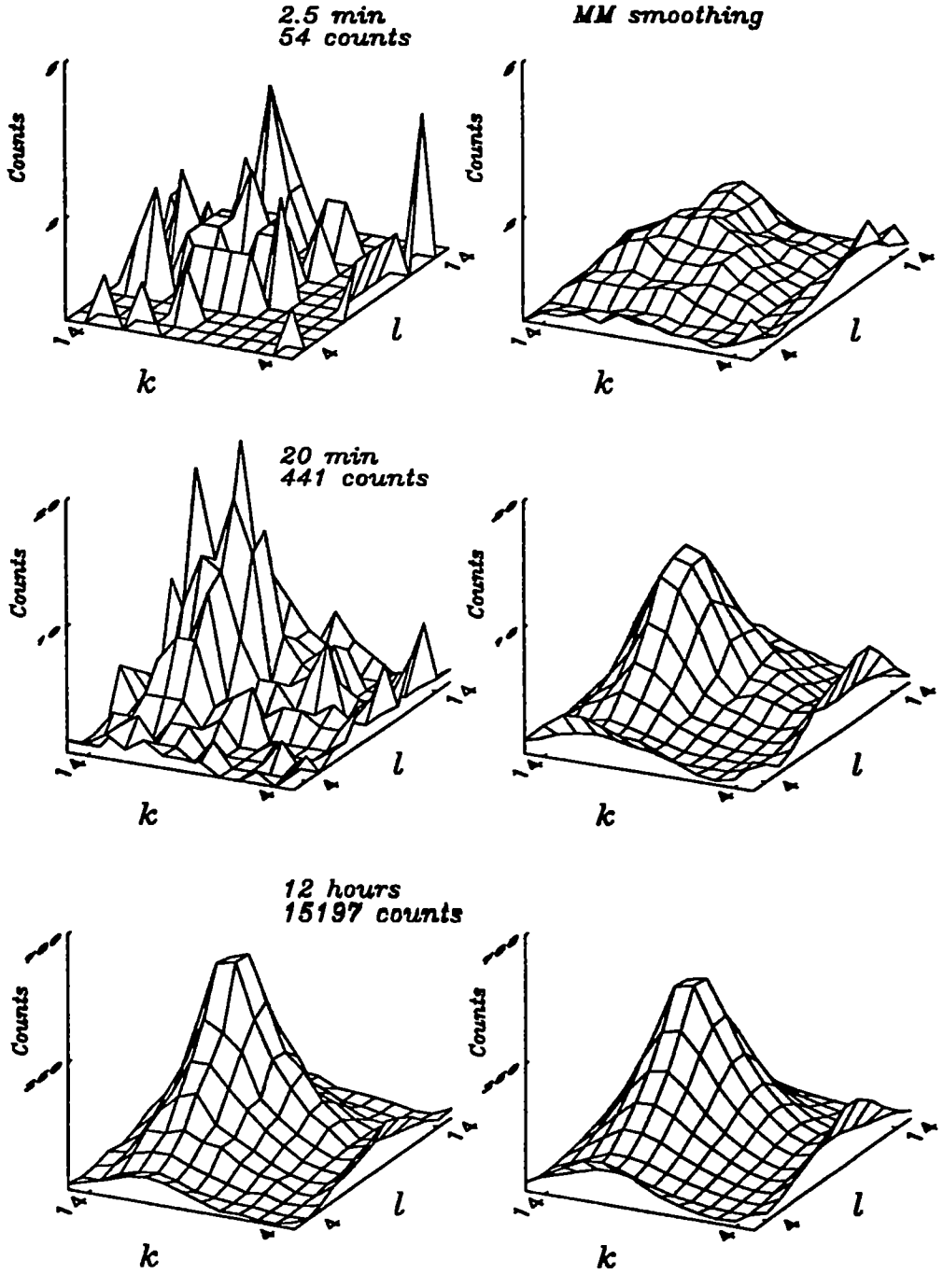

Figure 4.3. Same as figure 4.2 for random data.

Effect of spectral distribution

In order to investigate the effects of spectral distributions on variance reduction, the smoothing methods were applied to data acquired from the line source. The spectral shape

is significantly different when the LOR passes through ($D_{4,4}$) or misses ($D_{4,3}$) the source, as can be observed from the distributions shown in figure 4.4. It is also evident from this figure that *PC* smoothing is accurate in the first case, but fails to restore the correct distribution in the latter case. This is because the ideal distribution used for *PC* smoothing, which was derived from the plane source measurement, is inadequate to process data from LORs off the source position. Similar evaluations (not shown) have indicated that the other three smoothing techniques, which do not require *a priori* knowledge of the spectral distribution, do not suffer from this drawback.

Pre-processing sequence

The same data acquired from the flood source by detector pair (5,5) were pre-processed following the three sequences shown in figure 2.3, with and without preferential smoothing of the random data. Selected low statistics data smoothed using the *WS* technique are compared to the RN high statistics data in figure 4.5. The *NMSE* evaluated as a function of statistics for the different pre-processing protocols is presented in figure 4.6.

The comparison of the RN processed data of figure 4.5 with the corresponding emission and random data in figures 4.2 and 4.3 indicates that the subtraction of random events and the normalization for efficiency cause substantial noise amplification and spectral shape distortions in low statistics. The conventional RN sequence would thus be of little value with typical multispectral PET data where distributions are expected to have very few counts. Preferential smoothing of the random data set (S') in either the RS'N (not shown) or RNS' sequences leads to insignificant variance reduction and negligible improvements of *NMSE*. The need for minimizing statistical fluctuations in both the random and the emission data is clearly demonstrated by the results obtained with the protocols involving S or S".

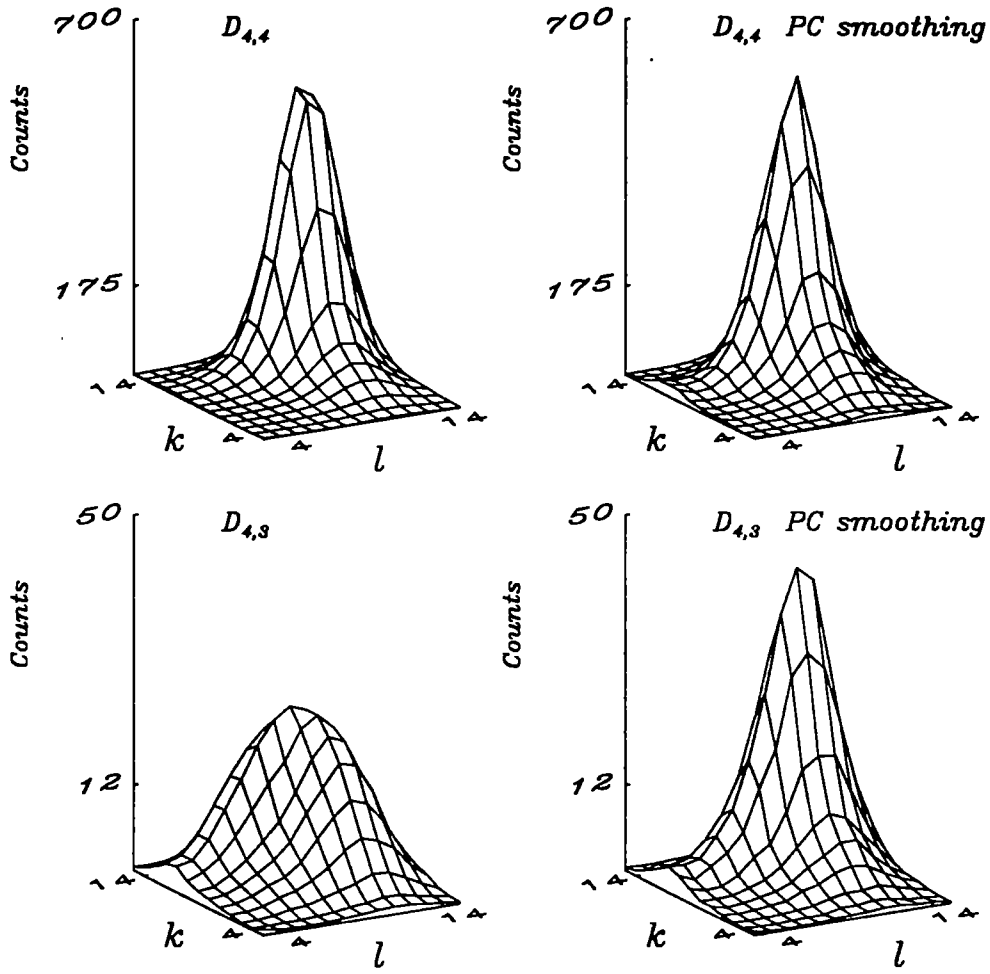

Figure 4.4. Energy spectra acquired from a line source by detector pair (4,4) whose LOR passes through the source and detector pair (4,3) which misses the source. *Left:* Distributions obtained from high statistics measurement (24 hours) and normalized to a 20-minute acquisition time. *Right*: *PC*-smoothed distributions of the 20-minute measurement obtained using the plane source measurement as the ideal distributions.

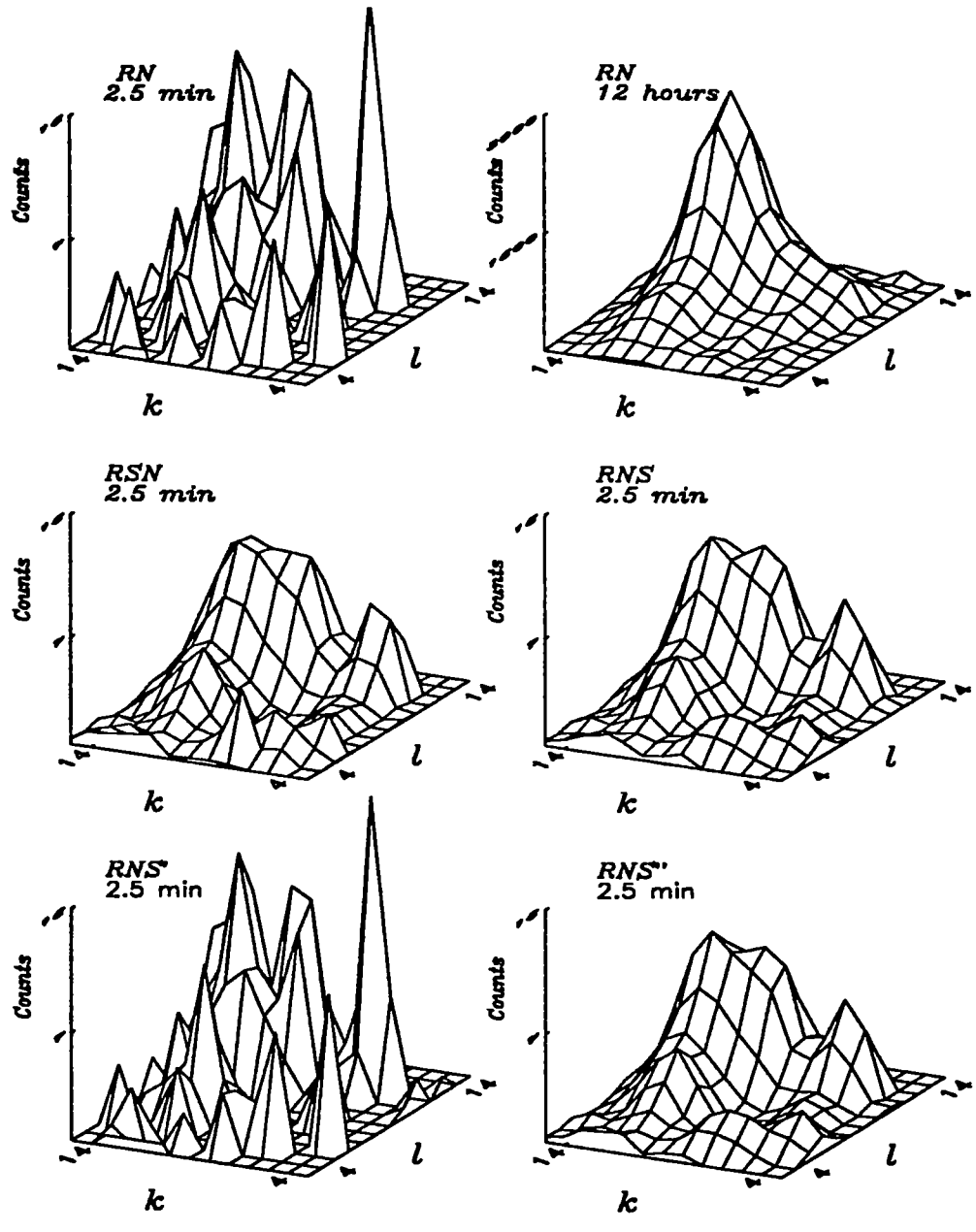

Figure 4.5. Comparison of spectral shape and texture for selected data pre-processing sequences. The data are from low (*2.5 min*) and high statistics (*12 hours*) measurements of the flood source acquired by detector pair (5,5). *WS* smoothing was used. The high statistics RN corrected distribution (*top right*) was used as the expected distribution for computing the *NMSE* values reported in figure 4.6.

processing of the randoms in the S" protocol also showed no apparent benefit. Irrespective of statistics, the RNS sequence appears more successful at reducing variance. The slight shape distortions observed with the RSN sequence suggest that, for best results, the systematic component of the variance needs to be reduced by normalization of detector efficiency before attempting to reduce the statistical components by energy space smoothing. Other evaluations by using the *ILF* and *MM* smoothing techniques have led to similar conclusions.

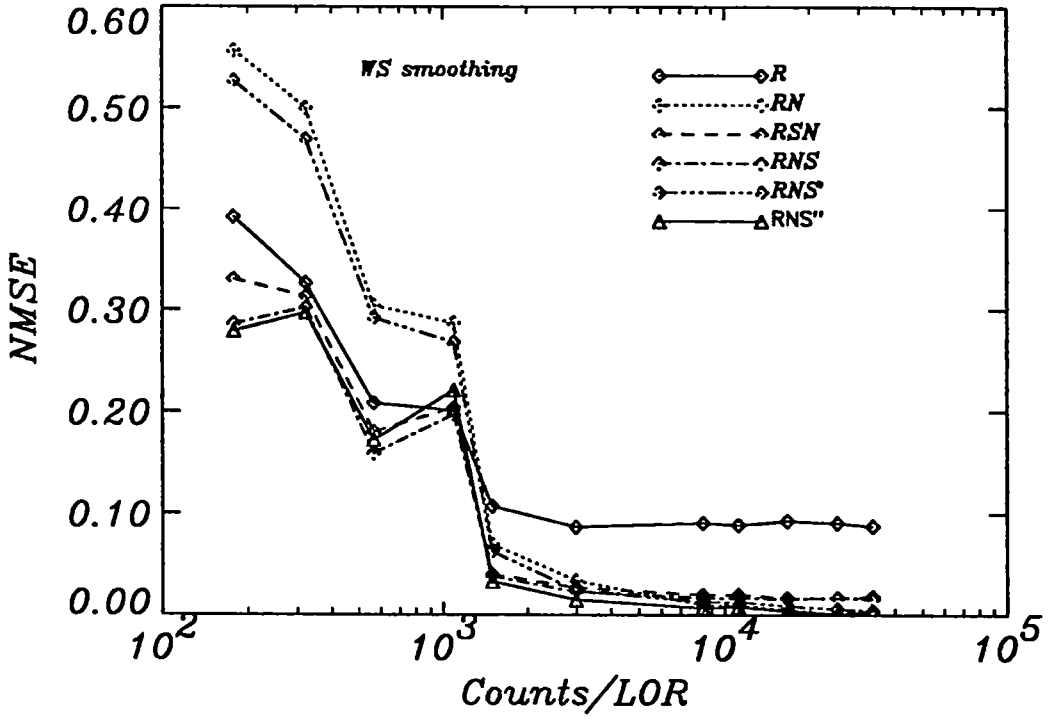

Figure 4.6. Normalized mean-square error (*NMSE*) as a function of statistics for different data pre-processing sequences. Results for the energy data measured from the flood source by detector pair (5,5) and smoothed by the *WS* technique are shown.

Variance reduction in projection space

Smoothing methods

With the detector configuration used in this work, a flood source is expected to generate approximately the same count number in every LOR between the two fixed arrays of opposite detectors. The indirect effect of spectral smoothing in the spatial domain was thus assessed by the relative standard deviation $\%SD_{kl}$ of the projection data. Results are presented in figure 4.7 for window pair $k=l=11$. As no normalization for detector efficiency was made, the 24% and 17% *SD* values for the high statistics emission and random data before smoothing should be attributed solely to the systematic errors of detector efficiency. These are natural limits which energy space smoothing aims to achieve for this window pair.

All spectral smoothing techniques were capable of reducing *%SD* in projection space. *PC* and *WS* smoothing techniques converged nicely to a plateau at the targeted *%SD* values. The other two smoothing techniques reduced *%SD* down to about 21% and 13% at high statistics for emission and random data, respectively. This is believed to be a consequence of the overcorrecting effect of these techniques on the photopeak value in the energy space, as pointed out above. Similar effects have been observed in lower energy windows, although *%SD* values were higher.

Pre-processing sequence

The same data acquired from the flood source by window pair $k=l=11$ is shown in figure 4.8 after pre-processing by several different sequences. A short acquisition with an average of less than 10 counts/LOR is compared to a long acquisition having more than 2000 counts/LOR. The *%SD* as a function of average counts/LOR is plotted in figure 4.9 for the different pre-processing sequences. The *ILF* smoothing method was used throughout for S, S' and S".

The plot in figure 4.9 indicates that the contribution of systematic error to the variance is prominent if the average counts/LOR is larger than about 100. The normalization in RN makes this contribution to *%SD* drop from 26% (after random subtraction) to a few percent only with high statistics. Smoothing of the emission and random data in the RSN or RNS protocols decreases *%SD* by an approximately constant amount (~20%), irrespective of statistics. Preferential smoothing of the random data in the RNS" (and RS"N) protocols reduces *%SD* further slightly, while smoothing of the random data set only (S') is inefficient. These results confirm that spectral smoothing in energy space can be successful at reducing the statistical variance as the systematic errors are suppressed independently by normalization in projection space. Similar trends were noted in all energy windows.

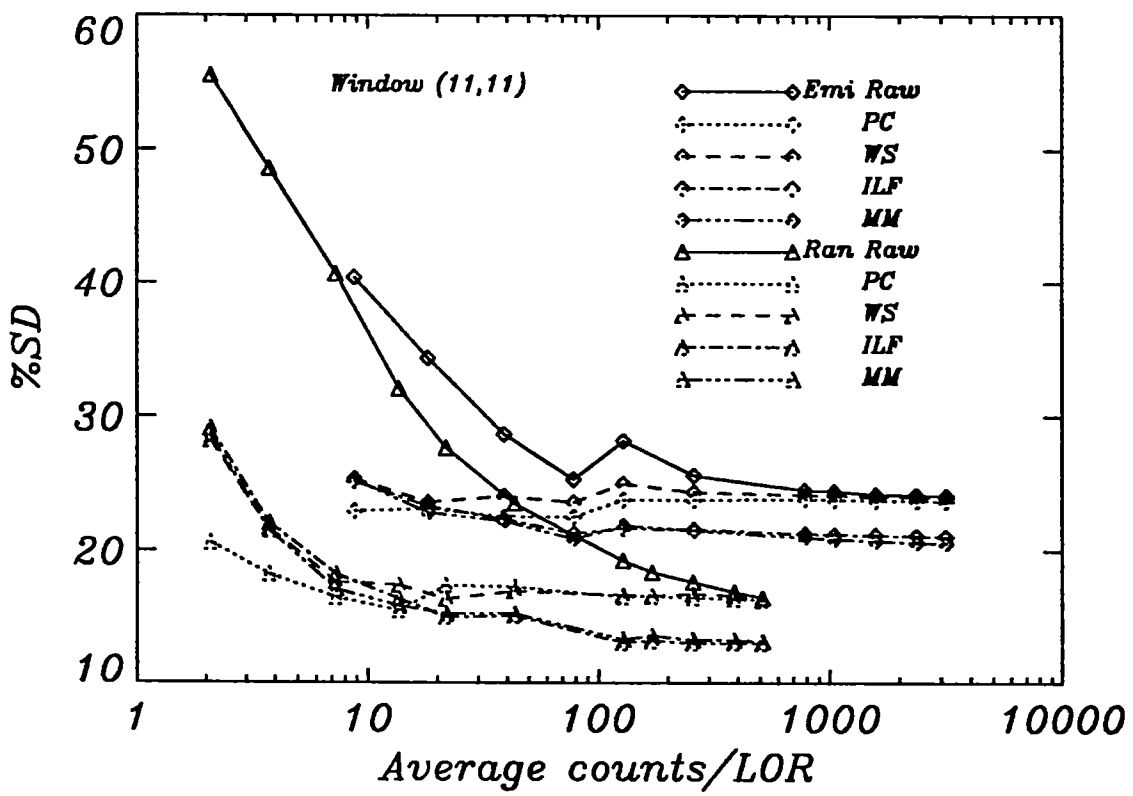

Figure 4.7. Relative standard deviation (*%SD*) of the projection space distributions for emission and random data acquired from the flood source in window pair

(11,11) as a function of average counts/LOR for the four smoothing algorithms.

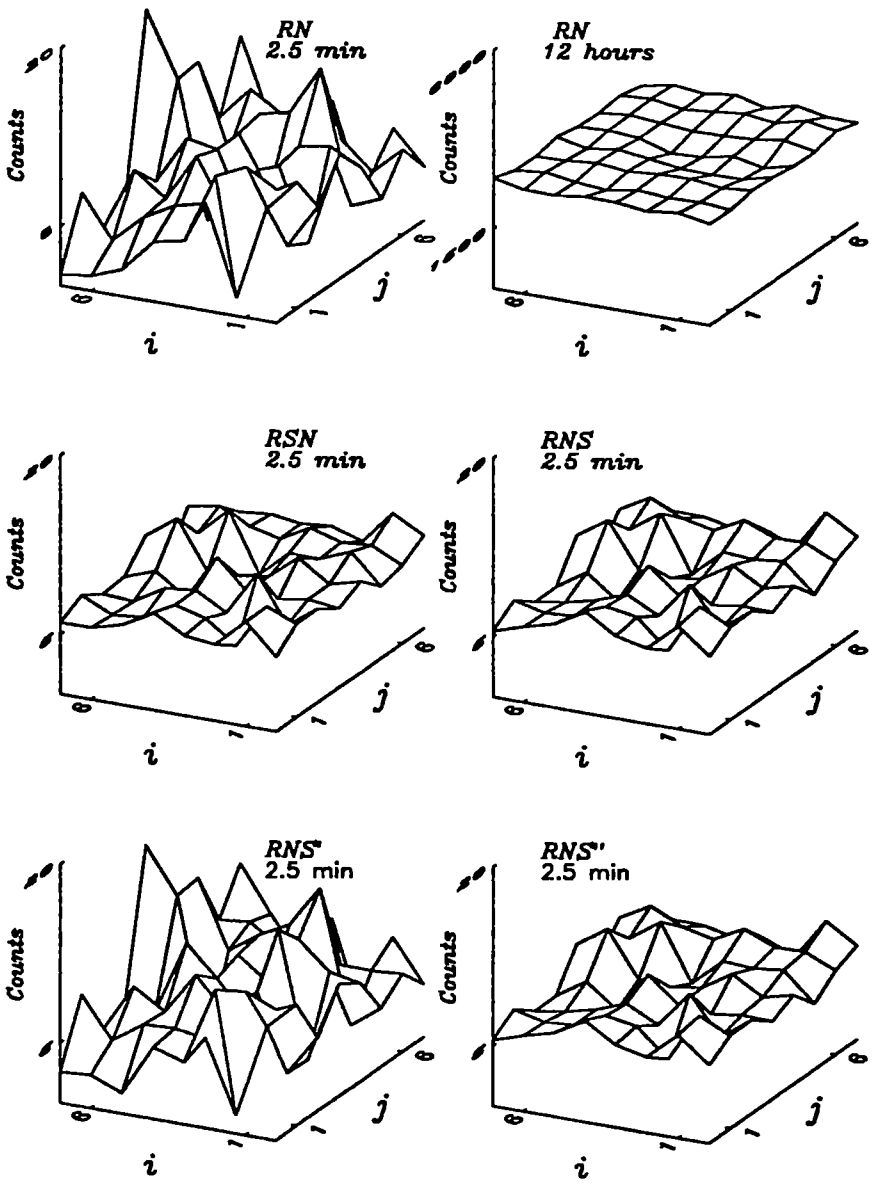

Figure 4.8. Comparison of projection space distributions from a flood source for different data pre-processing sequences. Low (*2.5 min*) and high (*12 hours*) statistics data acquired by window pair (11,11) are displayed. *ILF* smoothing was used.

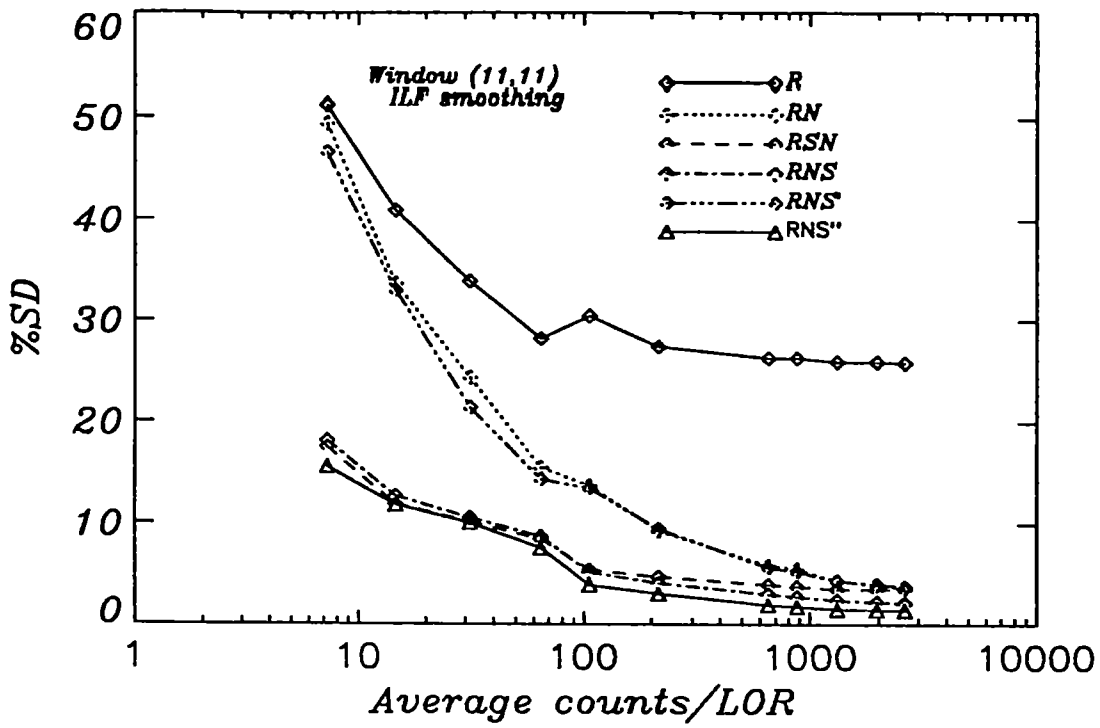

Figure 4.9. Relative standard deviation (*%SD*) of the projection space data from the flood source in window pair (11,11) as a function of average counts/LOR for different pre-processing protocols.

Effects on spatial distribution

Multispectral projections of a line source after RN and RNS, where S is either *PC*, *WS*, *ILF* and *MM* smoothing, were studied. The effect of *ILF* smoothing can be assessed visually in figure 4.10. RNS protocols using other smoothing techniques produced similar appearance. The overall spread of these line source distributions was evaluated as a function of total counts by the average autocorrelation width, *AAW* (figure 4.11) and the weighted projection deviation, *WPD* (figure 4.12).

Although it is clear that statistical fluctuations induce noise in the distributions about source location in low statistics measurements (figure 4.10, *left*), the resulting distortions do not affect resolution significantly, on the average (curve RN in figure 4.11). The *WPD*,

which is more sensitive to noise in the background away from the source location, decreases steadily as statistics increases (curve RN in figure 4.12). As statistical fluctuations within the energy space (along the *w* axis in figure 4.10) are mostly responsible for these effects, spectral smoothing overcomes these effects by suitably rearranging counts according to the expected energy distributions. A significant reduction of the background noise (as measured by *WPD*) and some improvement of resolution is obtained with all techniques except the *PC* smoothing, for which systematic deviation patterns occur (see figures 4.11 and 4.12). This is an indirect consequence of aberrations induced by this technique when the prior assumptions are not valid, as this was shown to be the case with a line source. *The event repositioning along the energy axis which leads to some minor effects on the width of the line spread functions is observed* to be roughly independent of statistics and smoothing techniques (excluding*PC* smoothing).

Variance reduction in images

Effect on spatial resolution

The FWHM and FWTM evaluated from the reconstructed line source images are presented in Table 4.1 for selected energy windows in the Compton (window 6: 259-301 keV) and the near photopeak (window 11: 474-516 keV) regions of the spectrum. The FWHM of RNS corrected data improved in the lower energy frames while the FWTM remained almost the same for both RN and RNS sequences. These results verify the hypothesis that smoothing in the energy space would have little detrimental effect on spatial resolution. It is noticed that spectral smoothing reduces the FWHM and FWTM for low statistics energy frame.

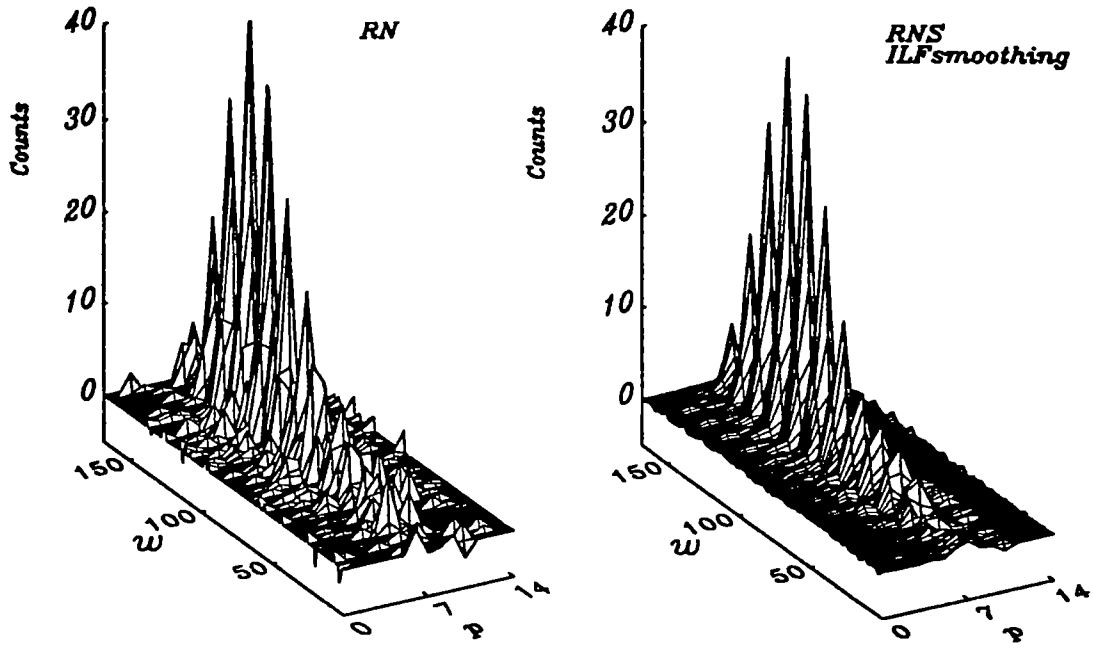

Figure 4.10. Multispectral projection data acquired from the line source processed by RN and RNS for a low statistics (*2.5 min*) measurement. Projections are shown as a function of the window pair number $w = 13*(k-3)+(l-3)$ for $k,l \geq 3$.

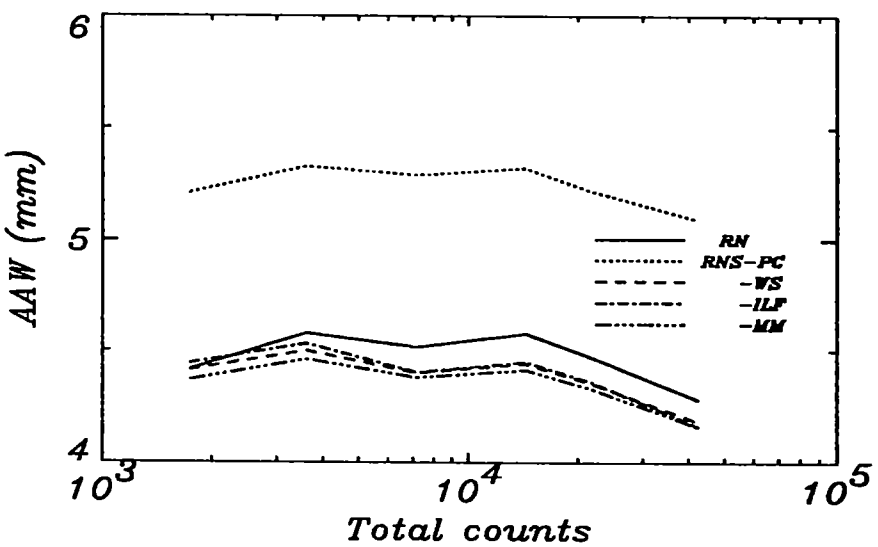

Figure 4.11. Average Autocorrelation Width (*AAW*) of the line source projection distributions as a function of total counts for the RN and RNS processed

data. Only windows k,l=9~14 were used to avoid *AAW* from being dominated by low energy profiles.

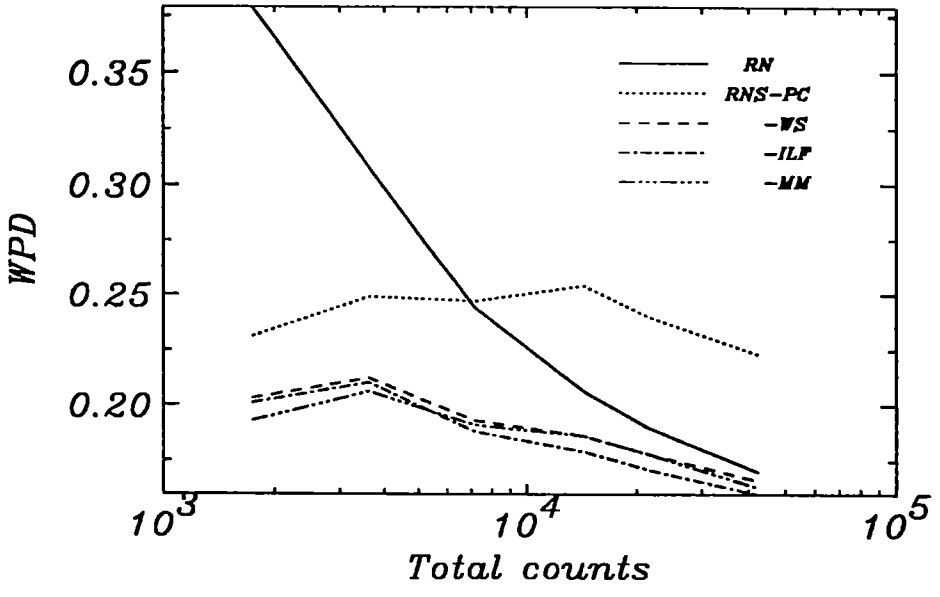

Figure 4.12. Same as figure 4.11 for Weighted Projection Deviation (*WPD*) index ($k,l \geq 3$).

Table 4.1. FWHM and FWTM evaluated from the images of the line source at 20 mm from center. Conventional (RN) and multispectral (RNS) data pre-processing techniques were applied on data.

	FWHM (mm)		FWTM (mm)	
	RN	RNS	RN	RNS
(6,6)	3.8	3.2	7.7	7.6
(6,11)	3.1	3.1	6.4	6.5
(11,11)	2.7	2.7	5.2	5.2

Table 4.2. Average counts and standard deviations in the largest hot spot and background ROI in the hot spot phantom image after being processed by conventional (RN) and multispectral (RNS) data pre-processing protocols.

	Hot spot		Background	
	RN	RNS	RN	RNS
(6,6)	8±5	9±3	15±15	14±7
(6,11)	33±9	33±4	9±11	8±4
(11,11)	120±17	109±12	4±7	4±2

Table 4.3. Contrast evaluated for the largest hot spot of the hot spot phantom image after being processed by conventional (RN) and multispectral (RNS) data pre-processing protocols.

	RN	RNS
(6,6)	0.14	0.32
(6,11)	0.31	0.61
(11,11)	0.51	0.76

Effect on multispectral images

A visual inspection of the images shown in figure 4.13 clearly demonstrates that data smoothing in the energy space in conjunction with normalization in projection space significantly improves statistical accuracy and sharpness of the multispectral image series. As we move from window 6 to window 11, the statistics increases from 21,791 counts to 179,125 counts, in proportion of the energy distribution. The effects of spectral smoothing were to suppress fluctuations in both the hot spots and background (see Table

4.2) and to improve image contrast by 49% to as much as 129% in the windows with low counts (see Table 4.3). A similar trend was observed for other energy windows.

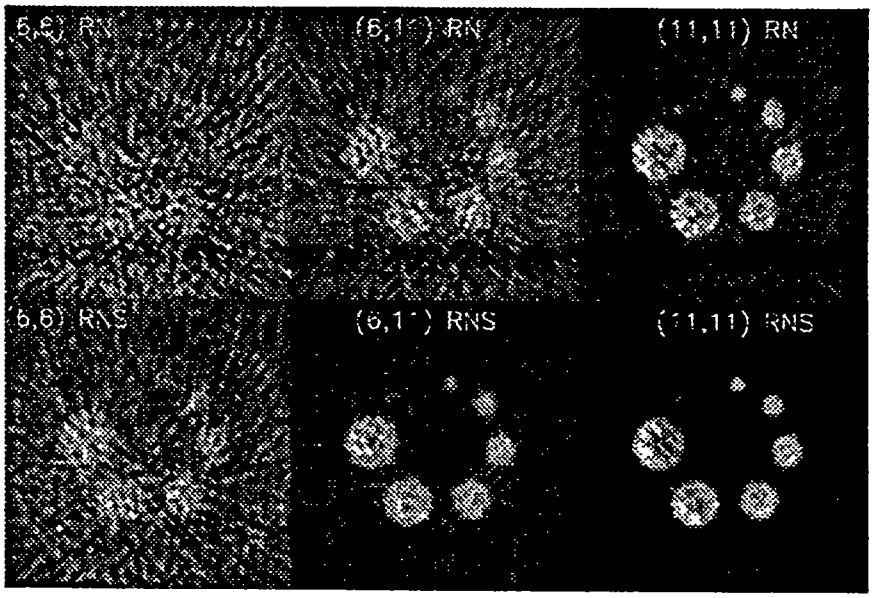

Figure 4.13. Images of hot spot phantom acquired in selected energy frames and processed by the RN and RNS sequences. Windows 6 and 11 correspond to the energy ranges [252 - 293] and [462 - 503] keV, respectively.

Multispectral Frame-by-frame (MF) scatter correction

The first multispectral scatter correction method proposed, the MF method, was compared with the methods using CW and BW acquisition modes. Both stationary and nonstationary scatter kernels were tested with the OSDR scatter correction algorithm. The conventional and multispectral data pre-processing protocols, RN and RNS respectively, were performed in combination with MF scatter correction. The smoothing algorithm (S) used is the Ideal Low-pass Filter (ILF). The CW and BW data without scatter correction performed are presented as references.

Table 4.4. Comparison of the effects of the different scatter correction protocols on spatial resolution, relative sensitivity and relative standard deviation. *%Sen.* is the sensitivity relative to the CW mode for each scatter correction. %STD(H) and %STD(C) are the relative standard deviations calculated from second largest hot spot and background ROI, respectively. The RN data pre-processing protocol was used in all cases and spectral smoothing was used for MF (RNS), where S is the ILF algorithm. The scatter correction algorithm for all scatter correction protocols is OSDR.

	No scatter correction		Stationary kernel				Nonstationary kernel			
	CW	BW	CW	BW	MF	MF (RNS)	CW	BW	MF	MF (RNS)
%Sen.	100	172	100	157	175	168	100	159	160	166
FWHM	2.88	2.91	2.82	2.81	2.84	2.83	2.82	2.80	2.84	2.84
FWTM	5.36	5.35	5.48	5.51	5.36	5.10	5.53	5.63	5.55	5.13
%STD(H)	10.4	10.4	11.2	11.5	13.8	14.2	11.7	12.1	13.0	12.6
%STD(C)	44.9	32.3	83.6	78.3	80.8	87.3	106.5	106.8	102.5	81.4

Table 4.4 shows the results of relative sensitivity, spatial resolution and relative standard deviation obtained from processed data. All scatter correction protocols with the BW and MF modes improved sensitivity by over 50% relative to CW without significant degradation of spatial resolution. When combined with the multispectral data pre-processing (RNS), the MF protocols apparently yield smaller FWTM than other protocols. This is in accordance with the observation in figure 4.11 and 4.12, whereby the AAW and WPD were reduced after employing spectral smoothing. If the corresponding CW FWTM is used as the standard, then this smaller FWTM can be considered as an deviation induced by spectral smoothing. The %STD in the hot region of the hot spot phantom image, i.e. %STD(H), is higher for MF protocols compared to CW and BW mode, which might be the result of accumulated variances in energy frames. The spectral smoothing slightly

aggravate this effect when many energy frames, i.e. too little counts in each energy frame (the stationary MF protocols), were used. This is reversed when less energy frames (the nonstationary MF protocols) were used.

Images processed by the scatter correction protocols using stationary kernels are presented in figure 4.14. As it is hard to visually perceive differences between these images, the profiles through the 15.8, 13.0 and 9.7 mm hot spots (see figure 4.14) are provided in figure 4.15. The effects of stationary and nonstationary scatter correction on contrast and relative activity recovery are evaluated quantitatively and compared in figures 4.16-17 for all the protocols.

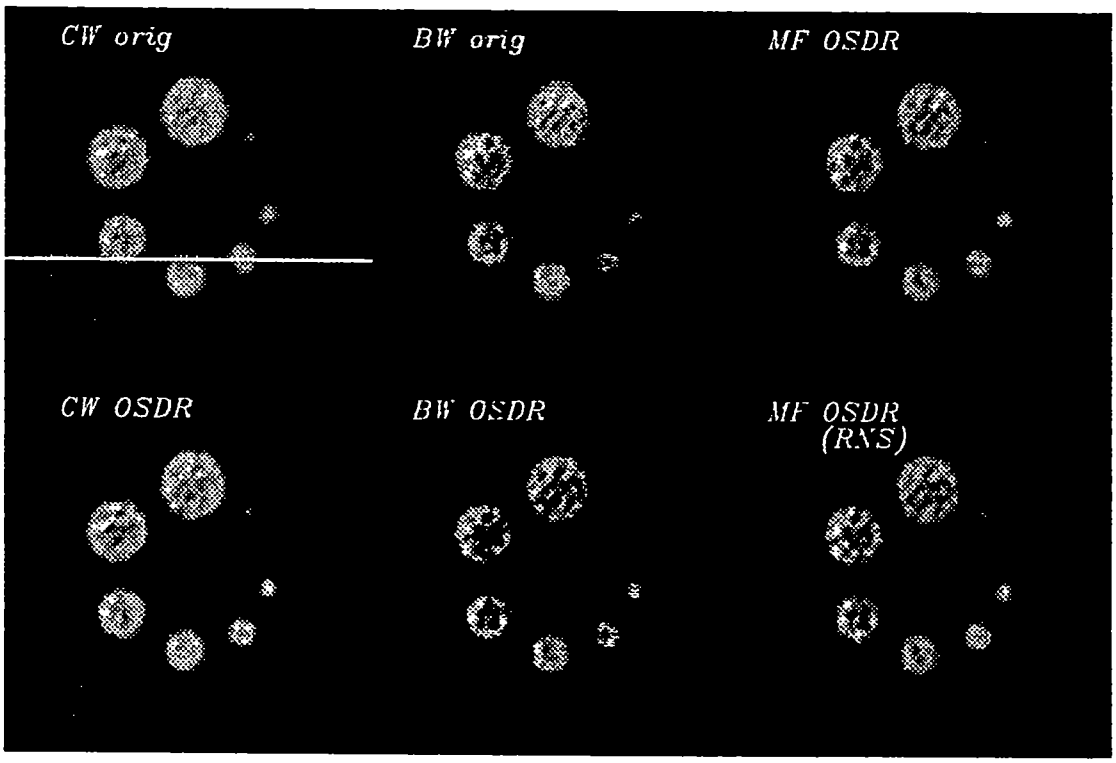

Figure 4.14. Hot spot images comparing the effect of Multispectral Frame-by-frame Object scatter Subtraction and Detector scatter Restoration (MF OSDR) with that of Conventional Window (CW) and Broad Window (BW) modes.

All protocols except the one indicated RNS used the conventional data pre-processing technique (RN) and stationary scatter kernel. S in RNS is the ILF spectral smoothing algorithm. The CW and BW data without scatter correction (orig) are shown as references.

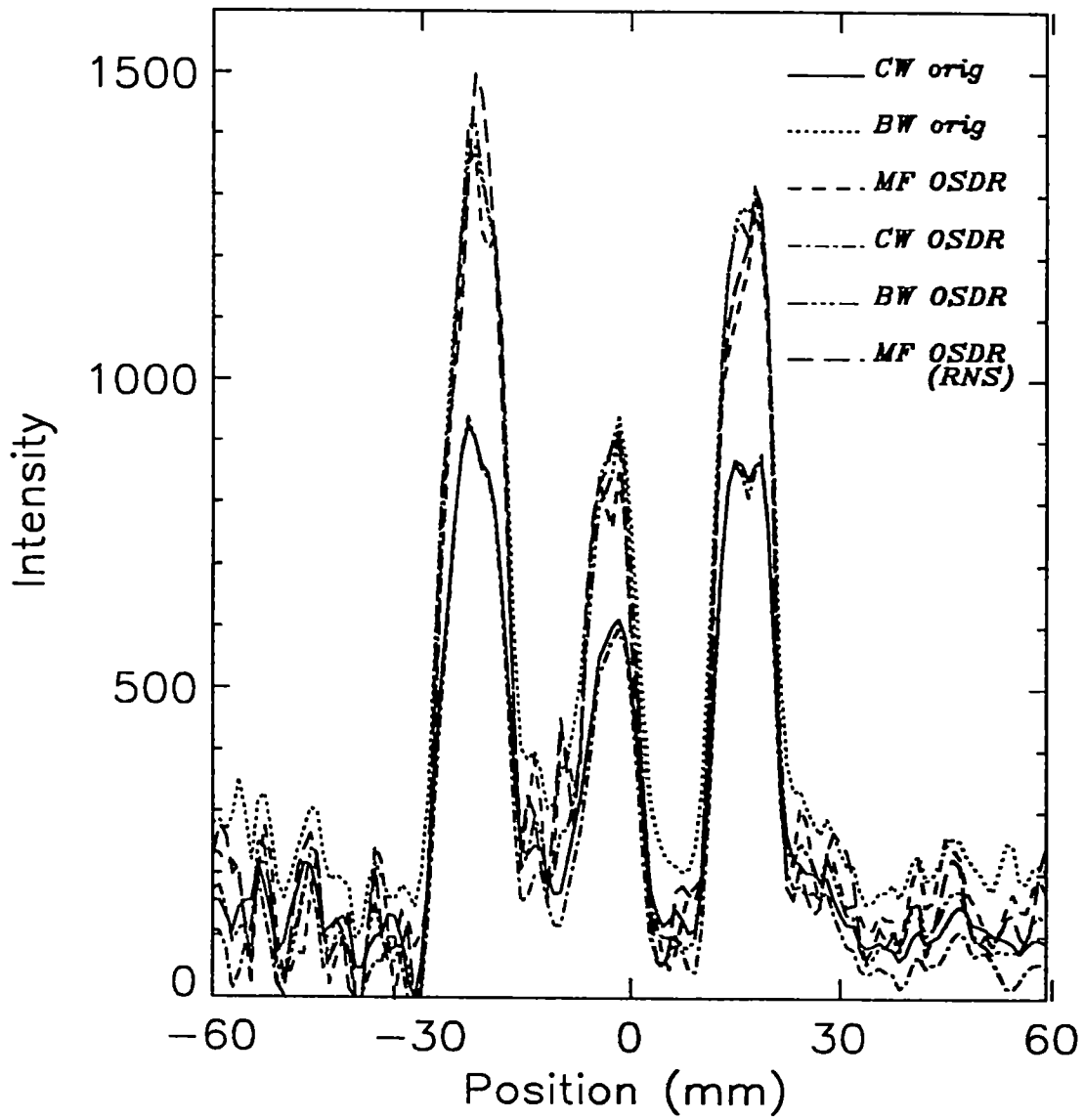

Figure 4.15. Profiles through the 15.8, 13.0 and 9.7 mm hot spots in the images of figure 4.14. The position of the profile is indicated in the top-left image of figure 4.14.

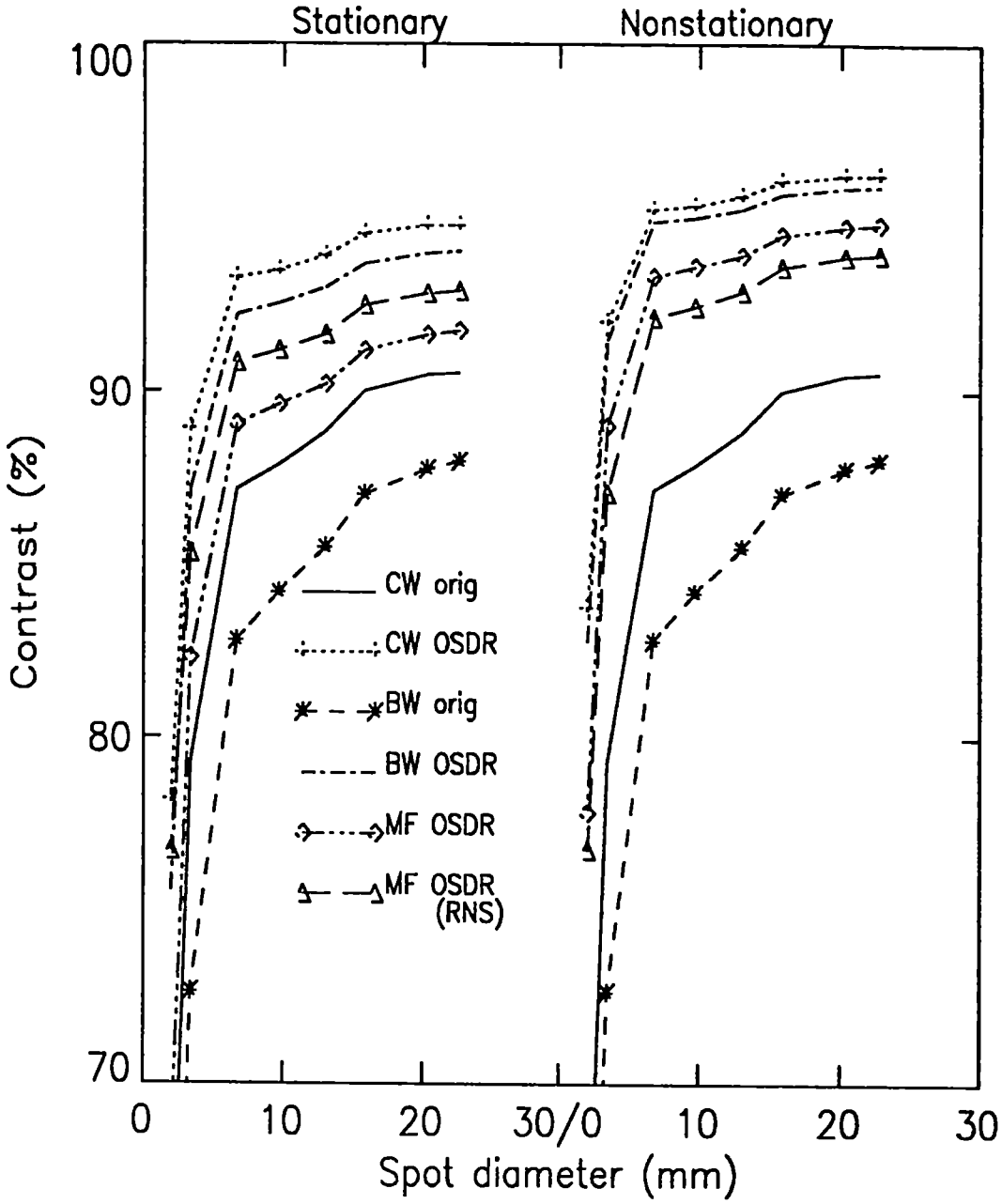

Figure 4.16. Comparison of contrast as a function of hot-spot diameter for images processed by the various stationary and nonstationary scatter correction protocols described in figure 4.14.

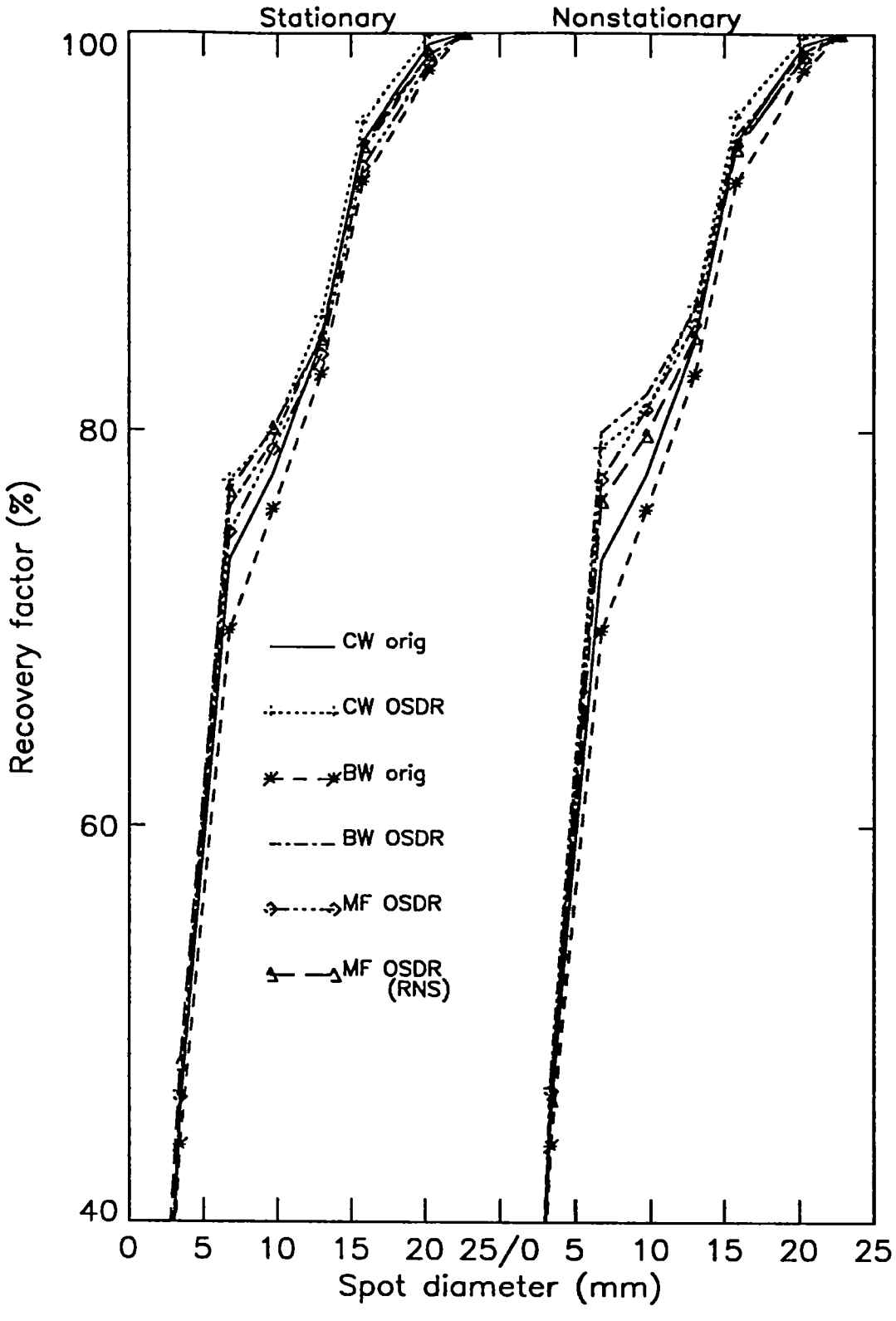

Figure 4.17. Same as figure 4.16 for the relative activity recovery factor.

While all scatter correction protocols with the BW and MF are shown to improve contrast and activity recovery, using nonstationary scatter kernels consistently achieves better results. The nonstationary BW OSDR method is the most successful at improving contrast (figure 4.16) and recovering activity (figure 4.17) in small ROIs. The performance of MF protocols, whether using RN or RNS data pre-processing techniques, is consistently inferior to that of BW mode in terms of contrast, activity recovery and noise characteristics (table 4.4). This result suggests that: 1) the postulate of MF is inherently deficient in terms of accumulated errors from making approximations in each energy frame; and 2) the smoothing algorithm and the data pre-processing protocol are not efficient enough in practical measurement situation.

Relative to the CW and BW protocols, the MF protocol using conventional data pre-processing technique (RN) is observed to be more sensitive to the nonstationarity of the scatter functions. The multispectral data pre-processing (RNS) procedure amended the performance of stationary multiple window MF method but degraded that of the nonstationary two window mode in terms of contrast and activity recovery. As a result, the MF protocol became less sensitive to the nonstationarity of scatter functions when it was combined with RNS. This observation clearly demonstrates the two sides of the smoothing technique: improving statistics and introducing deviations. When statistics is low, as is the case of using multiple windows for stationary MF, the benefit of smoothing is dominant; When statistics is relatively high, as is the case with the two energy windows used for nonstationary MF, imposing a pre-determined filter on data introduces deviations without bringing much improvement of the statistical significance. In these situations, the benefit of smoothing is overwhelmed by its disadvantage.

Global Scatter Correction

Results of spectral analysis

Principal components

The first six principal components obtained by applying Singular Value Decomposition (SVD) to a multispectral hot-spot phantom data set are shown in figure 4.18. The relative intensities of the images can be deduced from the quantitative information given in table 4.5. It is evident that the first principal component (ϕ_{1pc}) carries most of the information of the original data set. Although the hot spot pattern in the third principal component is clearly recognizable, its intensity is very low. The other components simply do not have the structure of original data. The components with higher order (nth principal component, $n \geq 7$, not shown) are similar to the case of sixth component.

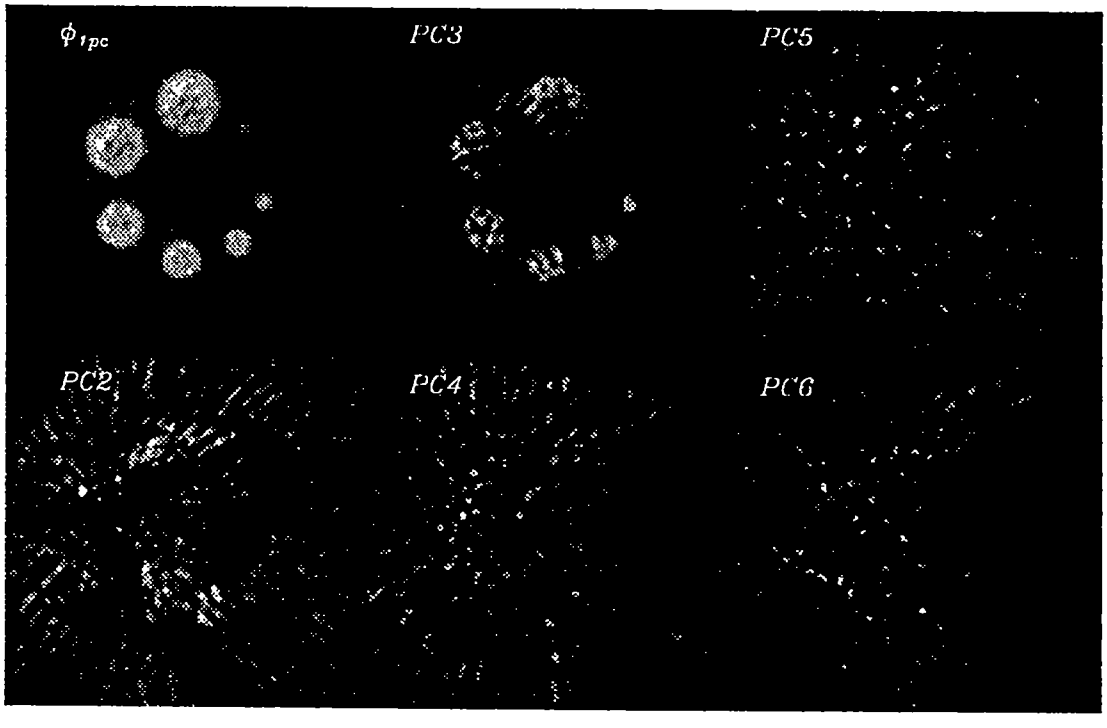

Figure 4.18. The images of the first six principal components of the multispectral hot spot phantom data obtained by Singular Value Decomposition (SVD).

Table 4.5. Quantitative information on the six principal components in figure 4.18. The maximum pixel values and total counts are given.

	Max. value	Total counts
ϕ_{1pc}	1863.34	4959160
PC2	0.028	53
PC3	0.037	24
PC4	0.042	53
PC5	0.028	36
PC6	0.042	51

Variances of principal components

The component variances for the hot spot phantom data are plotted in figure 4.19. Assuming that the image structure information is well represented by the variance of the data matrix, the dominant importance of ϕ_{1pc} is evident.

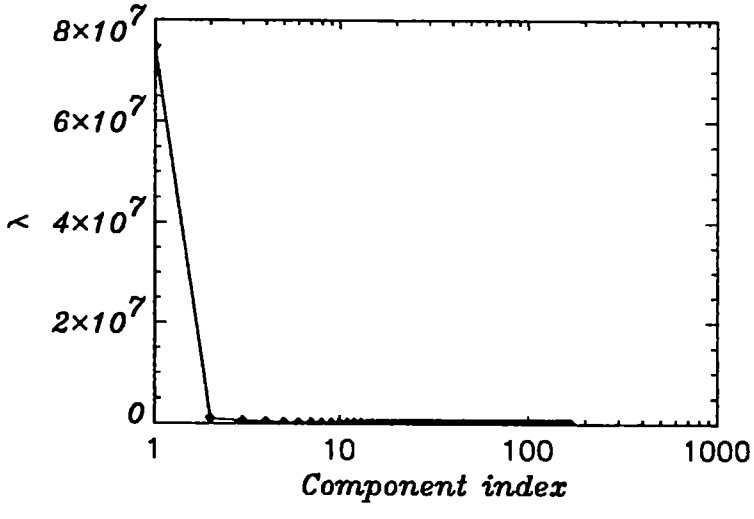

Figure 4.19. Variances (or eigenvalue) of the principal components obtained by decomposing the hot spot phantom multispectral data with SVD.

Transformation coefficients

Figure 4.20 presents the transformation coefficient vectors, $A_{col}(l)$, $l = 1,2...6$, for the principal components shown in figure 4.18. The coefficients are plotted in the 2D energy space where the two energy axis correspond to the energy of each coincidence event. The $A_{col}(l)$ coefficients can be interpreted as the weight of the original energy frames to the principal components. The transformation coefficients of ϕ_{1pc} (top left image) has a high degree of similarity with the high statistical emission energy spectrum presented in figure 4.5 (top right). This is in accordance with the physical interpretation that most of the photopeak region are true events which give useful structure information about the imaged object. We note that the coefficients of the third principal component are exclusively concentrated in the photopeak region, which explains why the hot-spot pattern in the corresponding component image is clear even though it has very low statistics (figure 4.19 and table 4.5). The coefficients have features which are difficult to interpret physically.

ϕ_{1pc}s of the line source measurements

The effects of PCA on off-centered line source data set are presented in figure 4.21. The projections for the off-centered line source were chosen at one arbitrary incidence angle. Clearly, the PCA reduces the intensity of scatter tails. It is also observed that the peak regions were not changed and there are still scatter component left in the $\phi_{1pc}s$.

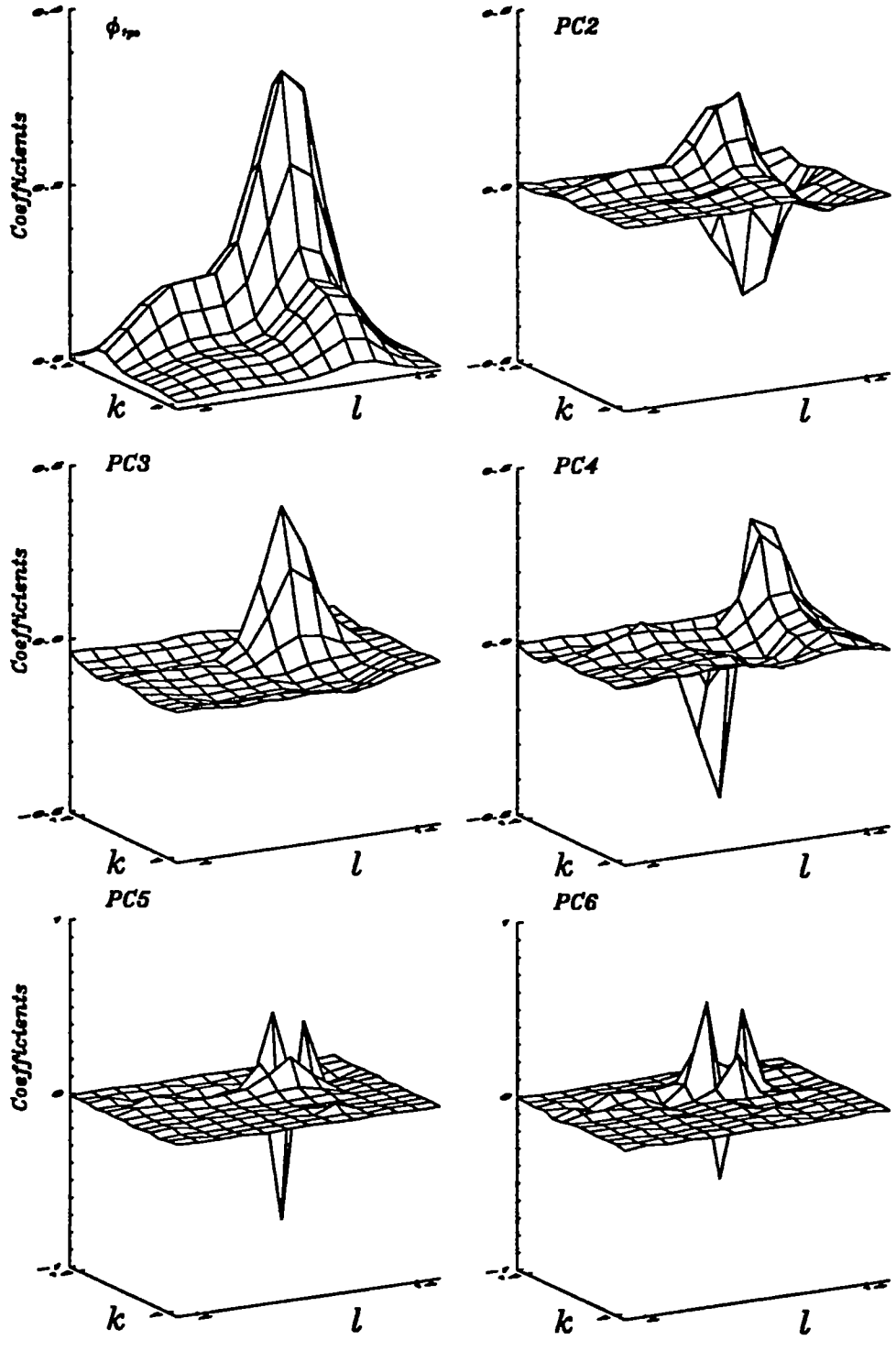

Figure 4.20. The transformation coefficient matrices for the first six principal components plotted as the function of 2D energy variables.

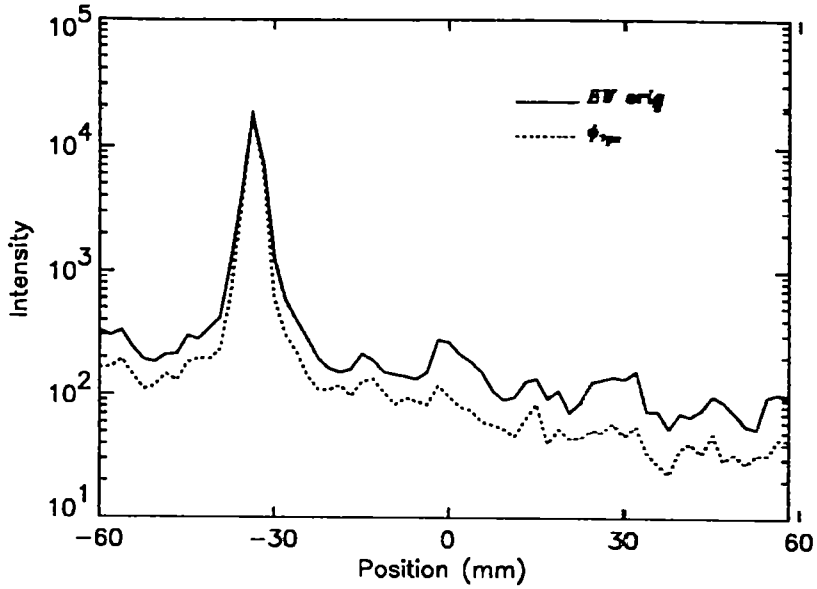

Figure 4.21. Comparing the original off-centered line source projection (BW orig) with its ϕ_{1pc} obtained by decomposing the original data by SVD. Both projections are from a incidence angle randomly selected.

ϕ_{1pc} of the hot-spot measurement

The projections shown in figure 4.22 was taken from one arbitrary angle of the hot spot phantom sinogram. Similar to the case of line sources, PCA has significantly reduced the counts in the background and the hot spot regions remains about the same. While the cold region of the projection indicates that scatter was not removed completely, it is necessary to use spatial scatter correction techniques to obtain the optimal result.

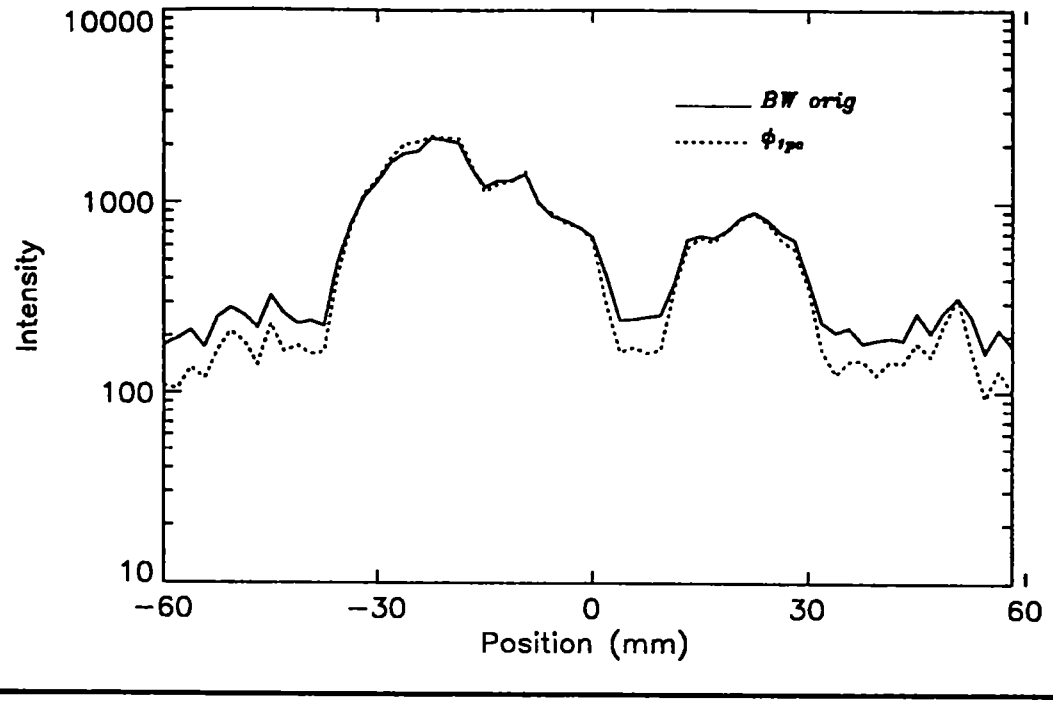

Figure 4.22. Comparing the projections of the Broad Window original (BW orig) data with the ϕ_{1pc} of the hot spot phantom measurement. The incidence angle was selected arbitrarily.

Comparison of GSC and other methods

The performance of the GSC method is assessed by comparing it with the OSDR scatter correction in both stationary and nonstationary modes with the Conventional Window (CW) and Broad Window (BW) settings. The scatter kernels extracted from ϕ_{1pc} of the multispectral line source measurement. Figure 4.23 shows hot spot phantom images processed by various correction protocols. The results from the original (orig) data in CW and BW modes are also shown as references. Since it is not easy to see differences from these images, the corresponding profiles at the location indicated in figure 4.23 are shown in figure 4.24. Several image indices will be employed for performance comparison.

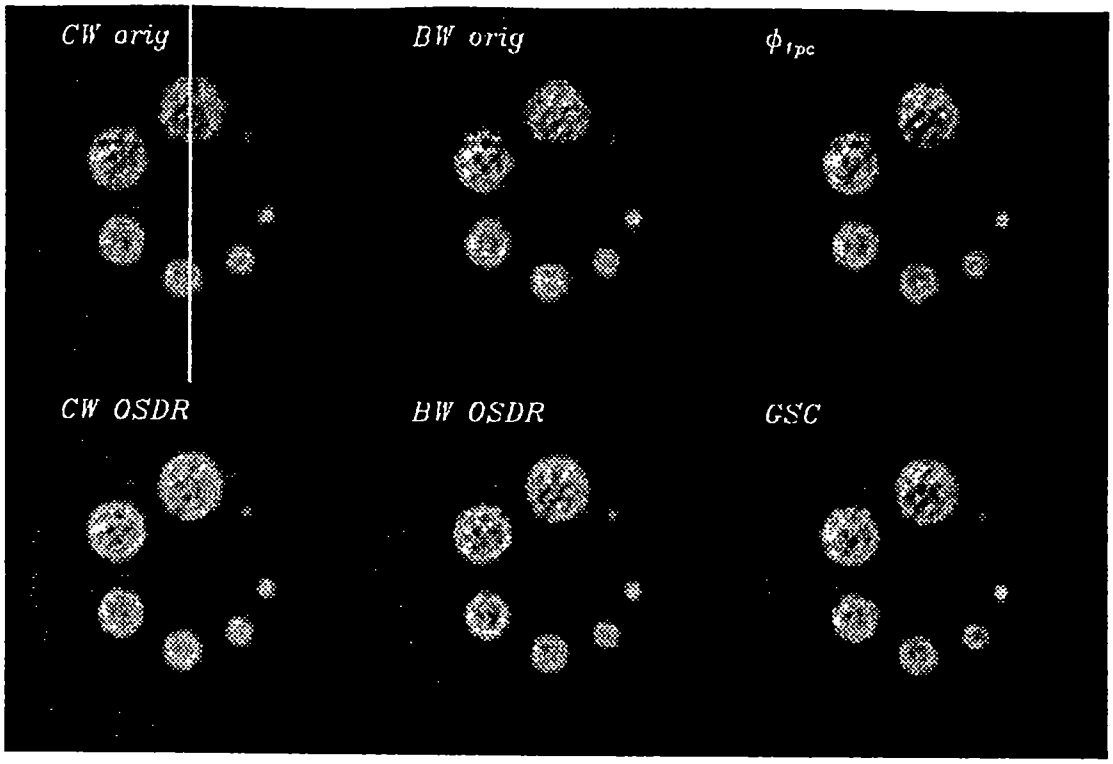

Figure 4.23. Comparison of the effects of various spectral and spatial scatter correction protocols on hot spot phantom data. Nonstationary kernel extracted from BW line source data was used for GSC. Normal BW and CW scatter kernels were used respectively for BW and CW OSDR algorithms. The original CW and BW images are shown as references. The image of the ϕ_{1pc} is also presented to show the result of spectral analysis by SVD.

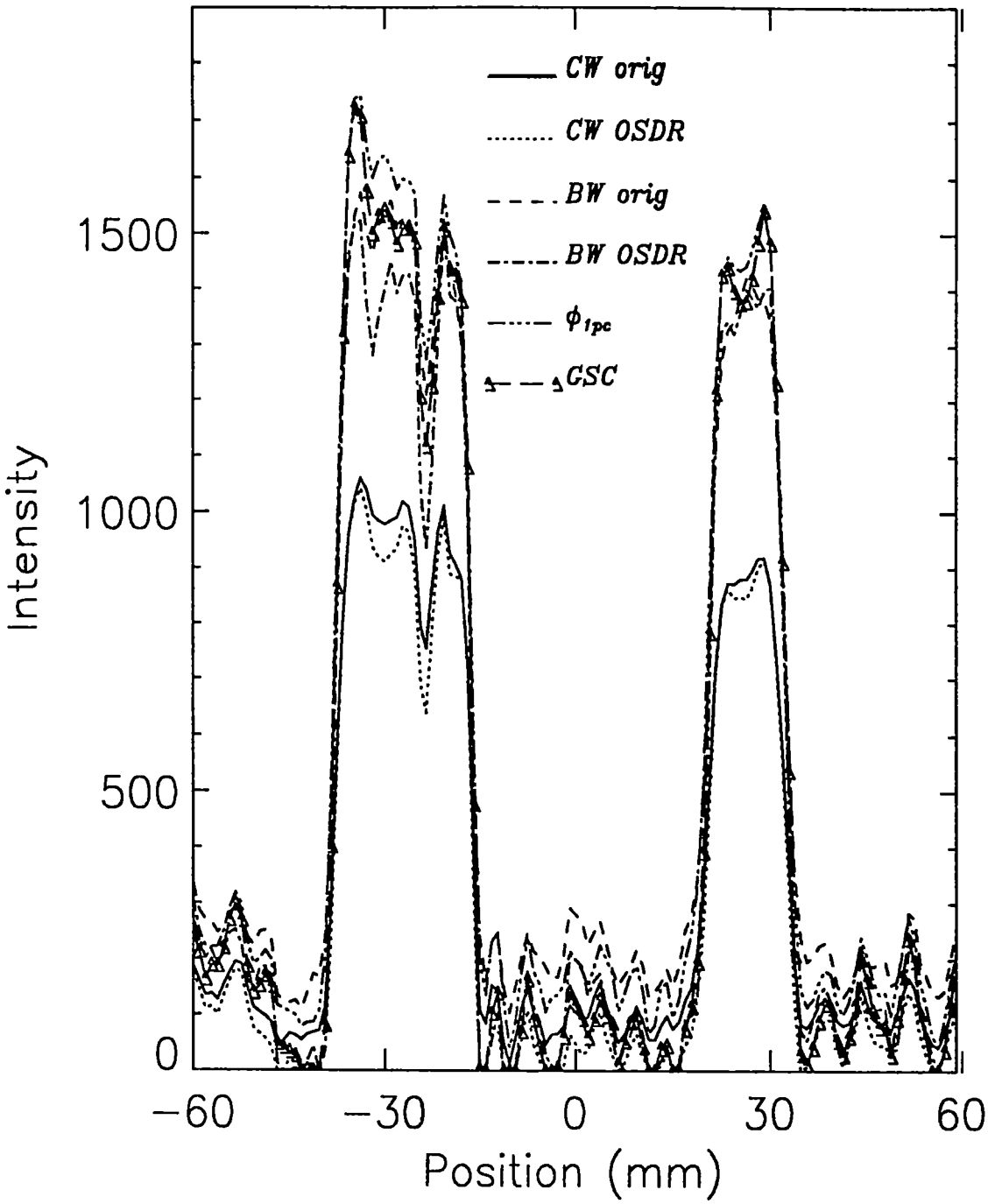

Figure 4.24. Image profiles through the 22.7 and 13.0 mm hot spots in the images of figure 4.23.

Spatial resolution, relative sensitivity and relative standard deviation

Table 4.6 shows the spatial resolution (FWHM and FWTM) evaluated by averaging over the radial and tangential profiles through the image of the line source at 10 mm from the center of the acrylic cylinder. It is apparent that all the scatter correction methods have about the same effect on resolution, the differences are negligible.

The effect of scatter correction protocols on sensitivity is also summarized in table 4.6. Similar to what reported in the MF protocol section, using events over a broader energy range in high resolution PET improves system sensitivity more than 50% before and after scatter correction. Similar results are obtained if the calculation is made by using the counts in the largest hot spot of the hot spot phantom image.

As one of the objective of this study was to test the effect of scatter correction on spatial resolution, the images were reconstructed using a ramp filter without low-pass filter. This has resulted in some amplification of the noise in the original images which amounts to relative standard deviation of about 7% in the 20.3 mm hot spot and 44% in the central cold region. These contributions add up to that generated by the scatter corrections. The total effects of reconstruction and scatter correction on the statistical noise were investigated by inspecting the changes in the texture of the noise in the 20.3 mm hot spot and the background ROI (see figure 3.2) in the images. It is observed that SVD slightly amplified noise in both hot and cold region because of its structure extraction feature. The nonstationary scatter correction schemes generally increased noise more than that of stationary schemes, but the GSC method shows about the same noise performance as the CW and BW OSDR algorithms. Looking at profiles of the largest hot spot in figure 4.24, we can see that the GSC causes less data fluctuation than the BW OSDR technique.

Table 4.6. Comparing the effect of GSC and conventional scatter correction methods on resolution, sensitivity and noise characteristics. Resolution (in mm) were measured from the reconstructed images of the line source at 10 mm from the center. The line source was in a scattering media of 110 mm diameter. The Relative sensitivity (%Sen, in percent) were obtained by comparing the hot spot phantom image of each data processing protocol with that of the corresponding CW protocol. The relative standard deviation (%STD) is calculated from the second largest hot spot (H) and the background ROI (C) of the hot spot phantom image.

	No OSDR			Stationary OSDR			Nonstationary OSDR		
	CW	BW	SVD	CW	BW	GSC	CW	BW	GSC
FWHM	2.87	2.90	2.86	2.82	2.81	2.80	2.81	2.78	2.81
FWTM	5.21	5.26	5.19	5.22	5.23	5.24	5.23	5.19	5.24
%Sen	100	172	161	100	157	163	100	159	163
%STD(H)	7.3	6.5	7.5	8.8	8.7	8.9	9.5	9.9	9.4
%STD(C)	44.4	33.0	41.7	84.0	81.4	82.9	108.4	111.2	106.2

Contrast

According to the profiles passing through the hot-spots of diameters 22.7 and 13.0 mm shown in figure 4.24, using BW acquisition increases counts in both the hot and cold regions compared to CW mode. The SVD (ϕ_{1pc}) enhances the counts in the hot region and removes counts in cold region. The OSDR step in GSC method removes counts in both the hot and cold region.

Figure 4.25 shows the contrast of the hot-spot phantom images evaluated according to (3.5) as a function of hot-spot diameter. Using nonstationary scatter correction consistently produces better results than using stationary kernels. While acquisitions by BW without scatter correction degrade contrast compared to CW, all the scatter correction protocols recovered the loss to a certain degree. The curves for CW original data and ϕ_{1pc} data are quite overlapped. This indicates that SVD improves data quality acquired in broad energy window to that of photopeak window acquisition. The GSC method finally achieves the contrast the same as using CW mode with a pure gain of sensitivity.

Activity Recovery

Similar to figure 4.25, the percentage activity recovery factors of hot spots calculated by (3.6) are presented in figure 4.26. Observation indicates that the effect of scatter correction is more efficient for middle sized spots and nonstationary kernels show better performance the their stationary counterparts. The SVD raises the count levels in hot regions compared to CW and BW original, GSC approaches the highest activity recovery ability among all the protocols. Because of amplifying the ditch on the plateau of the largest hot spot (figure 4.24), CW and BW OSDR scatter correction methods resulted in less counts in this region than in the second largest hot spot. This phenomenon is not seen for ϕ_{1pc} and GSC results.

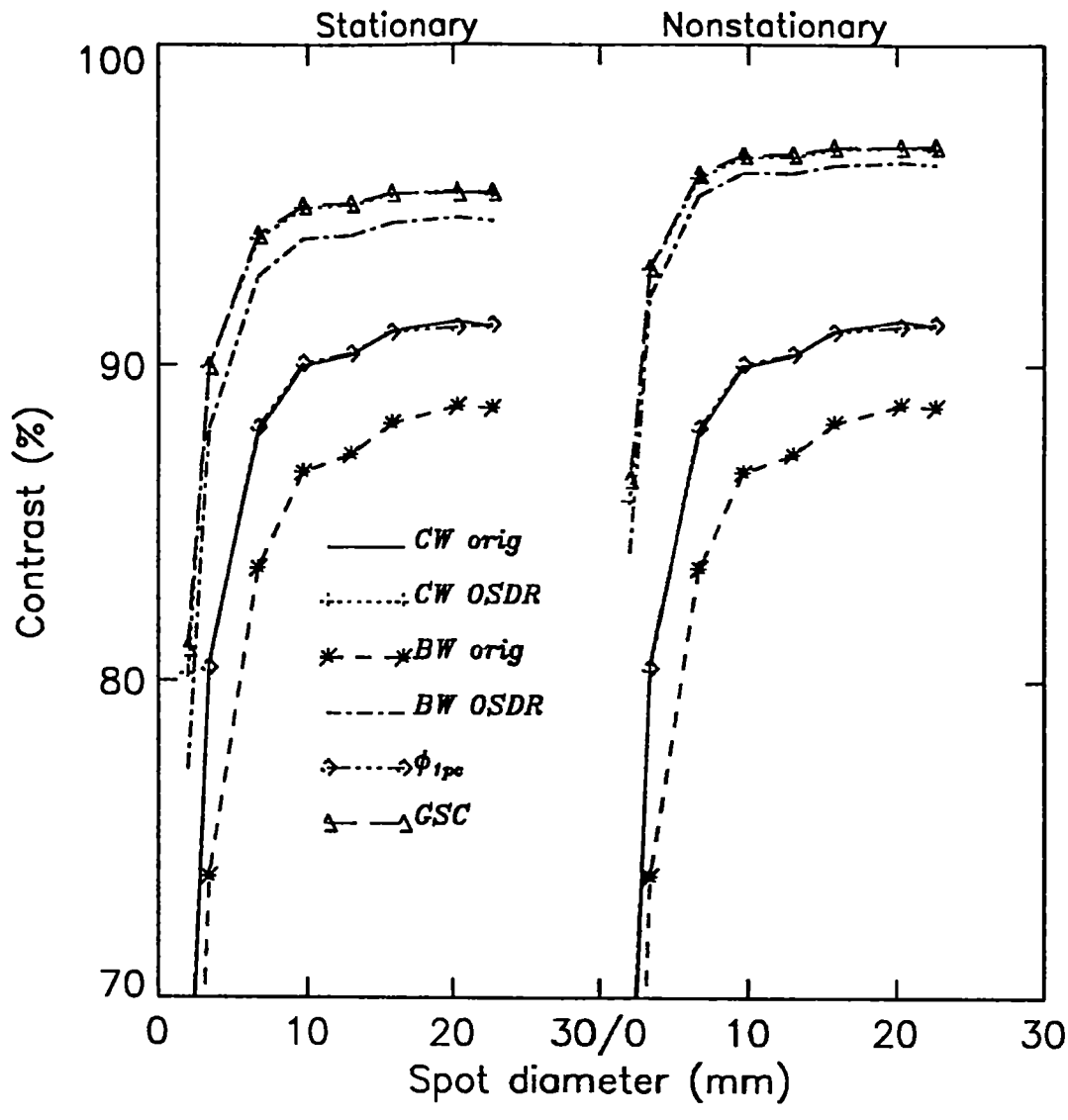

Figure 4.25. Comparison of contrast as a function of hot-spot diameter for images processed by the various stationary and nonstationary scatter correction protocols indicated in figure 4.23.

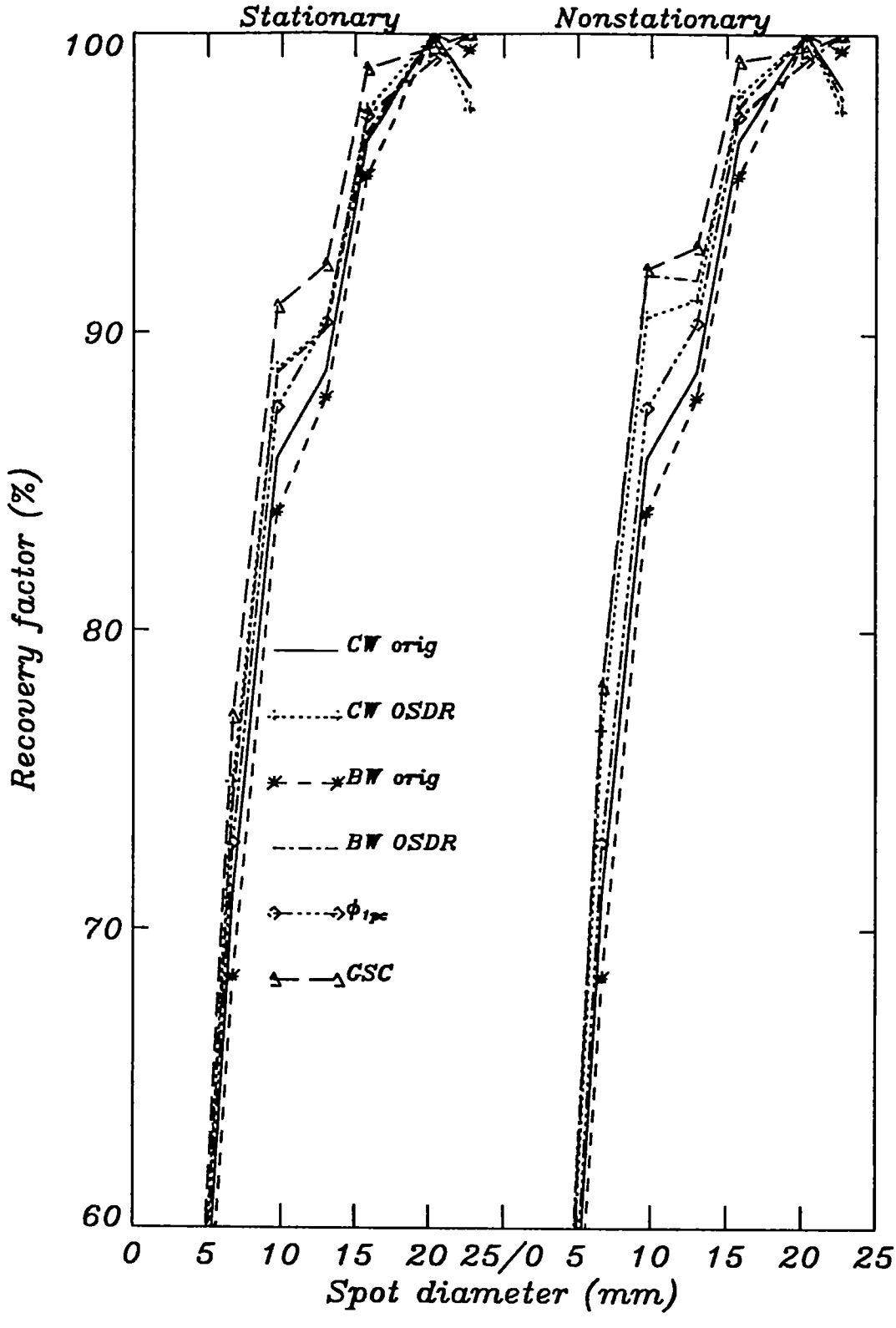

Figure 4.26. Same as figure 4.25 for the relative activity recovery factor.

Chapter 5 Discussion

Instrumentation and pre-processing considerations

The multispectral data acquisition imposes serious constraints on the detection system since photons over a broad energy range must be registered. For consistency of the multispectral data set, a number of technical problems must be addressed. First, the conversion gain for energy must be made identical in all detectors in order to have the photopeak in the same window for all detectors. To achieve this, the tuning of the pulse height and analog-to-digital conversion gain of all detectors is crucial (Cadorette *et al* 1993). Second, non-uniform detector efficiency as a function of energy must be compensated to have identical energy spectra in all detectors. The multispectral efficiency normalization (Msaki *et al* 1993) was developed to allocate photons to the proper energy window and correct for spectral symmetry before further processing the image data. This procedure ensures that the system response faithfully reflects the underlying physical interaction processes. A third requirement is that spatial distortions resulting from non-uniform detector energy responses must be avoided, i.e. the same primary image must be obtained in all windows. Needless to say that this last requirement is difficult to achieve with light sharing detector systems using array detectors. Therefore, utilizing independent individual detectors has been a definite advantage in assuring the integrity of multispectral data.

The number of windows is another important parameter to be considered for MSPET system. This number must be large enough for data acquisition to provide a sufficiently complete description of image behavior along the energy axis (Nyquist theorem). Too many windows, however, increase statistical uncertainty by distributing a limited number

of events over too many frames. In practice, a smaller number of energy windows reduces the requirements for data storage and calculation load. The Sherbrooke MSPET system uses 16 energy windows for each detector, thus generating a 256 2D energy spectrum for each coincidence detector pair. Due to electronic noise, only 13 windows above the noise threshold are used, thus reducing the useful energy space to 169 windows.

Photon spectral degradation model

The spectral photon degradation model was derived from its spatial counterpart, which can be used as a model for most spatial convolution scatter correction methods. On one hand, the more sophisticated energy-dependent expressions reflect the increased complexity of systems based on spectral analysis. On the other hand, it shows that the chance of successfully developing heuristic approaches without theoretical guidance is very small. Even so, as have been demonstrated by the analysis of the DEW and MF methods, the combination of the model and knowledge about the system response functions leads to deeper understanding of the acquisition and scatter correction processes. For example, it has been shown that R_{unsc} in the DEW method can be considered as a constant, independent of the imaging geometry, while R_{sc} is a function of several object and imaging system parameters. Using the additional knowledge provided by the spectral degradation model, approaches similar to the DEW technique but involving more relevant physical parameters can be derived. Such a model helps to bridge the gap between heuristic energy-based scatter correction hypotheses and the underlying physical assumptions, which is certainly critical in the development of new methods.

Multispectral Frame-by-frame (MF) scatter correction

& data pre-processing techniques

Multispectral data pre-processing

Requirements for variance reduction in multispectral data

The low statistics associated with multispectral data makes reduction of the statistical variance mandatory for subsequent efficient energy-dependent processing of multispectral PET images. Smoothing in the spatial domain is undesirable for this purpose since the process moves counts across LORs and would degrade spatial resolution. It is possible to overcome this drawback by processing the data in the energy space where count populations are associated with single LORs. However, the pre-processing algorithms must satisfy additional requirements if their ability to reduce variance is to be achieved without generating artifacts in the multispectral image series. Smoothing techniques must restore the spectral shape distortions due to low statistics and have little or no effect on the shape of distributions obtained in high statistics. This requirement was the basis for using high statistics distributions as reference. The second requirement is that the spectral variance suppression should be achieved without distorting the spatial distribution of the data within individual energy frames. As a third requirement, the above two conditions should be satisfied irrespective of the source distribution being processed. Finally, the variance reducing algorithms must have the ability to reduce all the sources of variance detailed by equation 2.32. In other words, the statistical variances as well as the systematic errors must be decreased concurrently.

Besides the spectral smoothing approach which works on a point-by-point basis in the projection space, Principal Component Analysis (PCA) is another way to realize noise reduction. Since PCA is initially designed for multidimensional data processing, it has great potential to be exploited.

Comparison of smoothing techniques

Four spectral smoothing techniques with different levels of constraints were evaluated in this work. All four techniques were capable of reducing substantially the spectral and the spatial variances of low statistics data, thereby producing distributions more comparable to the *expected* distributions obtained in high statistics (see figures 4.1, 4.7 and 4.12).

The *MM* smoothing technique involves no prior constraints. As a result, it has a tendency to overcorrect the photopeak value which causes some flattening of the distributions in energy space (see figures 4.1-3). Propagation of these spectral shape distortions into the spatial domain also results in some over correction of the statistical noise components (figure 4.7). By incorporating some prior information, the *PC* and *WS* techniques can be more successful in reducing the statistical variance, but they need to be used more cautiously. The relevance of the *ideal* distributions used as references in the *PC* technique is critical for its success. Inadequate references have been shown to be the source of aberrations in the energy space and artifacts in the multispectral projections. Since the relevance of the ideal distribution is not easy to meet in practice, the method is disqualified for its lack of reliability and high sensitivity to artifacts. The performance of *WS* smoothing is relatively good over the whole range of statistics. This was expected since the characteristics of the smoothing kernels were adjusted accordingly. However, the procedure to determine the kernel parameter b is not straightforward and is time consuming as it requires several prior acquisitions. In addition, the relevance of the prior acquisitions used to extract the optimum b values as a function of statistics cannot be guaranteed. In spite of its good performance, this lack of flexibility makes this technique unsuitable for the multispectral application.

The *ILF* technique is relatively insensitive to the spectral and source distributions. The cutoff frequency ν_c which is the only adjustable parameter is relatively easy to determine. In terms of simplicity, accuracy and modest computational time, the *ILF* smoothing was

considered as the method of choice for reducing the statistical variance in multispectral data. We note, however, that this technique would be difficult to implement with a smaller number of energy windows than used in this study.

Pre-processing protocols

The permutations of the pre-processing operations N, R and S in multispectral PET imaging leads to the three basic sequences and their variants shown in figure 2.3. The conventional RN (or NR) sequence is inefficient at reducing the overall variance of low statistics multispectral data in both the energy and projection spaces (see figures 4.6 and 4.9). Spectral smoothing was demonstrated to have the ability to reduce the statistical components of the variance in both the energy and spatial domains, while the systematic error component can be suppressed by normalization for detector efficiencies in the projection space. The trends observed in figure 4.9 suggest that these two sources of variance are weakly dependent on each other, as predicted by equation 2.32. For instance, spectral smoothing which is intended to reduce statistical variance is dependent on statistics, while normalization is not. Consequently, it should be possible to carry out these two processes independently. However, the discrepancies between results obtained with protocols involving the NS and SN sequences in figure 4.6, and to a less extent in figure 4.9, indicate that they are not completely independent. The latter sequence in which smoothing is performed before normalization appears to be affected by some systematic errors. The multispectral normalization procedure, which was designed to also restore spectral symmetry in the energy space as it compensates for detector efficiencies (Msaki *et al* 1993), is responsible for this disparity. Such spectral symmetry restoration was found necessary because it is virtually impossible to select and tune all detectors to have exactly the same output response in each window pair (Cadorette *et al* 1993). It is obvious that the correction for these spectral asymmetries which result from systematic differences in detectors should be carried out before further processing of the energy spectra. Therefore,

the NS sequence in which normalization for systematic fluctuations precedes spectral smoothing should be retained.

The use of optimized filters to smooth the random data set makes the reduction of statistical variance in random distributions very efficient (figures 4.1 and 4.7). This approach should be considered when the random contribution to total variance is dominant (e.g. first pass study after bolus injection, high rate dynamic studies). The marginal benefits observed in this study when using the S' and S" smoothing protocols result from the low fraction of randoms in data and, hence, the rather small contribution to variance resulting from the random subtraction. In such situations, the use of a different smoothing filter for the random data set is not necessary. Consequently, the RNS sequence in which the random corrected data is subsequently normalized and smoothed is the most convenient from the computational point of view.

MF convolution scatter correction

It has been pointed out that BW and MF methods are fundamentally different by comparing equation 2.11 and equation 2.26. A simple, workable MF algorithm has been derived by making approximations in each energy frame to incorporate spectral information into scatter correction scheme. This is in contrast with the BW approach, where the difference among energy frames is neglected. Considering the approximations made in each energy frame, it is not sure that the MF can achieve better result than using one window only. Although spectral smoothing alleviates the influence of low statistics, as shown by the performance of MF with RNS pre-processing, the MF approach yields inferior results than the CW and BW counterparts. Even reducing the numbers of energy windows to two in order to improve statistics, as was made for the nonstationary MF, does not produce better results than conventional scatter processing in a single CW or BW window.

It can be conjectured from these observations that: 1) the basic postulate of the multispectral frame-by-frame convolution scatter correction method may be deficient in the sense that the disadvantage of lower statistics overwhelms the advantage of more accurate energy discrimination; 2) the accumulated errors due to making approximation in each energy frame severely affect the accuracy of the final result; 3) the data pre-processing protocol developed is not efficient enough to fully remove noise. Considering the extra computation burden, it would appear to be more appropriate to consider different, global spectral scatter correction methods, such as principal component analysis (Gagnon *et al* 1988) and factor analysis (Buvat *et al* 1993, Mas *et al* 1990) in order to fully exploit the advantages of multispectral data.

Global Scatter Correction (GSC) method

Attempts at using Principal Component Analysis (PCA) or Factor Analysis (FA) to exploit the correlation which exists between dynamic image sequences (Barber 1980, Cavailloles *et al* 1987, Di Paola *et al* 1982) or spectral image series (Buvat *et al* 1993, Mas *et al* 1990, Gagnon *et al* 1988) have already been made by several groups. What distinguishes the GSC method proposed in this work from the others is: 1) only ϕ_{1pc} (first principal component) is preserved for further processing, all other components being discarded because they are shown to be negligible and/or to retain no useful information; 2) spatial analysis is introduced following the PCA spectral analysis; 3) all the processing are based on a photon spectral degradation model which provides for the physical justification for each processing step.

The justification for preserving ϕ_{1pc} only and the assumption of scatter and noise residuals in this component, has been analyzed in section 2.3. In summary, it is

postulated that the spectral information in multispectral data can be optimally extracted by PCA and that no further spectral manipulation is thus required on the ϕ_{1pc}. As demonstrated theoretically (equation 2.62) and experimentally (figure 2.8), scatter component still exists in ϕ_{1pc} , which can be best further processed with spatial scatter correction techniques. With most of the non-useful information removed, ϕ_{1pc} is closer to the desired primary data φ than the measured raw data p_m . So starting from the better quality data (ϕ_{1pc}), further spatial convolution scatter correction methods (equation 2.11) should achieve a better result. The results presented in figures 4.22-26 demonstrate that the combination of spectral and spatial processing improves image quality and yields the best results.

One disadvantage of the GSC method is the increased data processing time introduced by the extra spectral analysis (PCA) step. Using the SUN SPARC II in our lab, it spends about 40 minutes to obtain the first principal component while the spatial scatter deconvolution and restoration uses about 5 minutes. From the experience of processing the cylinder phantom measurement data, the performance of the technique has been stable and reproducible. However, to prove its general applicability and superiority for more complicated acquisition situation, extensive tests for phantoms with irregular geometry, nonsymmtric density and source distribution should be made. In addition, the source dependency of the scatter kernel used for spatial analysis needs to be investigated.

Comparison with other methods

Principal Component Analysis and Factor Analysis are powerful tools for multi-dimensional data analysis and have been widely used in many fields. One common difficulty to most of the existing applications is the physical interpretation of the output. In the case of GSC, a physical interpretation of ϕ_{1pc} can be given within the framework of

scatter degradation model (see section 2.3). However, it is more difficult to relate other components to a physical phenomenon.

Gagnon *et al* (1989) have also proposed an interpretation of PCA. They assumed that ϕ_{1pc} is the sum of primary and the scatter events and the second component is the sum of scatter and noise. This interpretation was used to deduce scatter and noise contributions in the data set. The scatter is then removed by subtracting a fraction of the second principal component from ϕ_{1pc} (Gagnon *et al* 1990). In this way, no further processing (spectral or spatial) is needed. However, no sound theoretical ground nor convincing experimental evidence has been provided to support the postulate.

Based on the application of factor analysis of medical image sequences (FAMIS), Mas *et al* (FADS, 1990, 1990b) and Buvat *et al* (FAMIS-TAS, 1993, 1995b) considered a purely mathematical orthogonal decomposition of the factor analysis. Since the resulting vectors of the decomposition can not be physically interpreted directly, this step is only used as a noise reduction algorithm. Further analysis is performed to determine the oblique vectors which convey the physical information such as the photopeak component and scatter components. As a few (typically two to four) vectors are preserved for ensuring no loss of useful information, the efficiency of the noise reduction is limited. To search for the physical factors from the orthogonal vectors, the specific knowledge about the factor functions is a prerequisite. This greatly restricts the applicability of the method. Most results reported to date are based on simulated data, and the approach has not received, as yet, confirmation from experimental data.

Physical interpretation of the third principal component

Since orthogonality among *Principal components* is only mathematical, the physical meaning of the higher order *Principal components* gets by transformation. It is

interesting, however, to observe the images of principal components (figure 4.18) and the corresponding transformation coefficients in different energy frames (figure 4.20). The third principal component has a very weak, but still hot-spot pattern. It can be conjectured that the event quality forming this component is very high, so even with very limited counts the image structure is still clear. This is further demonstrated by the corresponding transformation coefficients which are well concentrated in the photopeak region (figure 4.20). It would appear that this component is, in fact, a fraction of the geometric component. The reason for being separated ϕ_{1pc} can be explained by the orthonormality of the PCA vectors. Due to the oblique relationship between the geometric and scatter components, ϕ_{1pc} in the L dimensional space is a vector deviating from the original geometric vector. The projection of the geometric component on the first principal component constitutes its most prominent contribution, as discussed in Chapter 2. Another fraction of the geometric component, which is perpendicular to the ϕ_{1pc}, naturally forms another basis vector in the *Principal component* space. Depending on the relative proportion of scatter, geometric and noise components in this measurement, this perpendicular component is the third one in this case. The low intensity of the third principal component independently confirms that the loss of primary information due to PCA is very small.

Nonuniformity consideration for scatter kernel

It has been shown that the nonstationary OSDR algorithm used is successful in recovering contrast and activity. However, one important factor which has not been tested in this study is the object nonuniformity: the phantom used for extracting the scatter kernels was similar to the object to be corrected. As this condition is usually not satisfied in realistic situations, the discrepancies between kernels derived from a uniform phantom and the scatter characteristics of an arbitrary object can be the source of significant inaccuracies which the use of BW is expected to exacerbate. MS data

acquisition and PCA processing are expected to be less sensitive to such effects since the energy information is available to help scatter correction. Considering that the covariance between primary and scatter varies greatly with the object characteristics and source distribution, more phantom tests will be needed to warrant the relevance of the scatter kernel.

Chapter 6 Conclusion

Photon spectral degradation model

By introducing the energy variable into the conventional photon spatial degradation model, a new spectral degradation model is established. The model provides a complete spatial and spectral description of the physical processes of emission, scattering and detection in multispectral detection systems. It constitutes the theoretical basis for scatter correction methods exploiting the energy information and helps to bridge the gap between several heuristic spatial and spectral scatter correction approaches and the underlying physical processes. As the model describes physical acquisition process of multispectral system analytically, it opens opportunities in developing new energy-based scatter correction algorithms.

Using the model and knowledge of the energy dependent sub-system (object, detector etc.) response functions, the deficiency of the Dual Energy Window (DEW) method is analyzed. It is demonstrated that the ratio of scatter components in two energy windows, R_{sc}, a key factor used by DEW, is dependent on many parameters such as source position, object geometry, source distribution, etc. The over-simplified hypothesis made for DEW, i.e. assuming R_{sc} is constant or a simple function of source position, makes the method inaccurate in most real situations. To improve the performance and the applicability of the method, extensive experimental or simulation work will be needed to establish a suitable empirical ratio for various acquisition conditions.

The analysis of the multispectral frame-by-frame (MF) convolution scatter correction method is another example of the model's application. By comparing the approximations

made in the MF and BW convolution scatter algorithms, it is clearly shown that the MF algorithm allows the energy dependence of PET data to be used to improve scatter correction. On the other hand, the cumulative errors resulting from statistical noise in each energy frame and from the approximations of the MF algorithm still limit the accuracy of this approach. Results tend to demonstrate that the disadvantage of MF overwhelms its advantage even when used in combination with the spectral smoothing of multispectral data.

Multispectral data pre-processing and frame-by-frame scatter correction

Multispectral (MS) acquisition system provides an environment for studying the energy characteristics of PET data and for developing energy-dependent data processing techniques in high resolution PET. However, the use of multiple energy windows spreads data in a multidimensional space and dramatically increases systematic errors and statistical fluctuations. Furthermore, correction for efficiency and subtraction of random coincidence events augment statistical variance to a point where data is not usable anymore. Therefore, some pre-processing is mandatory to reduce the variance or the dimensionality of MS data. Suppression of the spectral variance was demonstrated to improve the statistical and systematic characteristics of data without detrimental effects on spatial resolution thereby making data smoothing in the energy space an additional necessary pre-processing procedure for further multispectral frame-by-frame processing of the data. The proposed pre-processing sequence, in which subtraction of random coincidence events (R), normalization of detector efficiency (N) and spectral smoothing (S, the *ILF* smoothing algorithm) are performed sequentially, successfully reduces variance from statistical and systematic origins in multispectral data and provides

improved data for energy dependence study and further energy-dependent image processing in PET.

Since making approximations in each energy frame accumulates errors in the final result, the energy-dependent multispectral frame-by-frame convolution scatter correction protocol shows inferior performance to that of BW mode. The multispectral data pre-processing technique developed in this work improves the statistical characteristics of data set to a certain level, but it can not fully recover energy spectrum shape for very low statistics data and introduces artifact for high statistics data. For this reason, the protocol which combines multispectral data pre-processing and MF techniques yields some performance improvement in scatter correction for multiple window acquisition, but degrades the performance for two energy window compared to using conventional data pre-processing technique. And most importantly, no matter with or without spectral smoothing, the MF protocols are not as good as using BW mode. Considering the heavy calculation burden of smoothing energy spectrum and making convolution in each energy frame, it is concluded that more suitable multispectral variance reduction and scatter correction concepts should be investigated in order to fully exploit the advantages of multispectral data. The data pre-processing protocol including the energy space smoothing technique can be used in studying the characteristics in certain energy frames.

Global Scatter Correction (GSC)

As indicated by its name, this method introduces the concept of combining spatial and spectral analysis in one scatter correction method. This method involves two steps. First, maximum noise and data dimensionality reduction is achieved by preserving only the first principal component (ϕ_{1pc}) of the output of the Singular Value Decomposition (SVD). While preserving most of the useful correlated information, this step removes

large amounts of non-correlated noise and some of the scatter contributions in the data. Second, a relevant spatial convolution scatter correction algorithm, the Object scatter Subtraction and Detector scatter Restoration (OSDR) model in this study, is used to correct the residue of scatter component. The theoretical basis of the method is demonstrated, including the rationale for preserving only the first component of PCA to achieve the maximum benefit from spectral analysis and the consideration of performing further spatial scatter correction. Results of processing multispectral hot spot phantom and line source measurement data show that the GSC method has superior performance in terms of image contrast and activity recovery, and has about the same effect on spatial resolution and noise characteristics compared to the conventional spatial convolution methods. To fulfill the need for high resolution, high sensitivity and high quantitative accuracy in nuclear medicine images, this method represents a promising direction of investigation .

It is worth noting that all the techniques developed in this work are readily applicable to multiple energy window acquisition in scintigraphic or SPECT systems.

References

Acchiappati D, Cerullo N and Guzzardi R 1989 Assessment of the scatter fraction evaluation methodology using Monte Carlo simulation techniques *Eur. J. Nucl. Med.* **15** 683-6

Adam L E, Bellemann M E, Brix G and Lorenz W J 1996 Monte Carlo-based analysis of PET scatter components *J. Nucl. Med.* **37** 2024-9

Allard C D, Strother S C and Evans A C 1987 Analytic scatter correction as a function of object size and spatial position *J. Nucl. Med.* **28** 695P

Alpert N M, Chesler D A, Correia J A *et al* 1982 Estimation of the local statistical noise in emission computed tomography *IEEE Trans. Med. Imag.* **1** 142-6

Axelsson B, Msaki P and Israelsson A 1984 Subtraction of Compton-scattered photons in single-photon emission computerized tomography *J. Nucl. Med.* **25** 490-4

Bailey D L and Meikle S R 1994 A convolution-subtraction correction method for 3D PET *Phys. Med. Biol.* **39** 411-24

Barney J S, Rogers J G, Harrop R and Hoverath H 1991 Object shape dependent scatter simulations for PET *IEEE Trans. Nucl. Sci.* **38** 719-25

Barney J S, Harrop R and Dykstra C J 1993 Source distribution dependent scatter correction for PVI *IEEE Trans. Nucl. Sci.* **40** 1001-7

Barney J S, Harrop R and Atkins M S 1994 Addition of noise by scatter correction methods in PVI *IEEE Trans. Nucl. Sci.* **41** 1551-5

Beck J W, Jaszczak R J, Coleman RE *et al* 1982 Analysis of SPECT including scatter and attenuation using sophisticated Monte Carlo modeling methods *IEEE Trans. Nucl. Sci.* **NS-29** 506-11

Bendriem B, Wong W H, Michel C *et al* 1989 Analysis of scatter deconvolution technique in PET using Monte Carlo simulation *J. Nucl. Med.* **28** 681

Bendriem B, Trébossen R, Frouin V and Syrota A 1993 A PET scatter correction using simultaneous acquisitions with low and high lower energy thresholds *Nucl. Sci. Symp. & Med. Imag. Conf. Rec.* **3** 1779-83

Bentourkia M, Msaki P, Cadorette J and Lecomte R 1995a Assessment of scatter components in high resolution PET correction by nonstationary convolution subtraction *J. Nucl. Med.* **36** 121-30

------- 1995b Energy dependence of scater components in multispectral PET imaging. *IEEE Trans. Med. Imag.* **14** 138-45

------- 1995c Object and detector scatter function dependence on energy and position in high resolution PET *IEEE Trans. Nucl. Sci.* **42** 1162-7

------- 1996 Nonstationary scatter subtraction-restoration in High Resolution PET *J. Nucl. Med.* **37** 2040-6

Bentourkia M and Lecomte R 1996 Energy dependence of non-stationary subtraction-restoration scatter correction in high resolution PET *IEEE Nucl. Sci. Symp. & Med. Imag. Conf. Rec.* (to be published)

Bergström M, Eriksson L, Bohm C *et al* 1983 Correction for scattered radiation in a ring detector positron camera by integral transformation of the projections *J. Comput. Assist. Tomogr.* **7** 42-50

Bevington P R 1969 *Data reduction and error analysis for the physical sciences* (New York: McGraw-Hill)

Bloomfield P M, Rajeswaran S, Spinks T J *et al* 1995 The design and physical characteristics of a small animal positron emission tomograph *Phys. Med. Biol.* **40** 1105-26

Bohm C, Kesselberg M and Eriksson L 1986 The use of an optimized coincidence time window in BGO positron cameras *IEEE Trans. Nucl. Sci.* **NS-33** 1078-80

Bowsher J E and Floyd C E 1991 Treatment of Compton scattering in maximum-likelihood, expectation-maximization reconstructions of SPECT images *J. Nucl. Med.* **32** 1285-91

Brooks R A, Sank V J, Friauf W S, *et al* 1980 Design considerations for Positron emission tomography *IEEE Trans. Biomed. Eng.* **BME-28** 158-76

Brownell G L and Sweet W H 1953 Localization of brain tumours with positron emitters *Nucleonics* **11**(11) 40-5

Buvat I, Benali H, Frouin F *et al* 1993 Target apex-seeking in factor analysis of medical image sequences *Phys. Med. Biol.* 1993;38 123-128.

Buvat I, Benali H, Todd-Pokropek A and Di Paola R 1995a Scatter correction in scintigraphy the state of the art *Eur. J. Nucl. Med.* **21** 675-94

Buvat I, Rodriquez-Villafuerte M, Todd-Pokropek A *et al* 1995b Comparative assessment of nine scatter correction methods based on spectral analysis using Monte Carlo simulations *J. Nucl. Med.* **36** 1476-88

Cadorette J, Rodrigue S and Lecomte R 1993 Tuning of avalanche photodiode PET camera *IEEE Trans. Nucl. Sci.* **40** 1062-6

Cadorette J, Rodrigue S, Rouleau D *et al* 1996 Performance Characteristics of Avalanche Photodiode PET Scanner (Abstract) *IEEE Nucl. Sci. Symp. & Med. Imag. Conf. Rec.* (to be published)

Carrier C, Martel C, Schmitt D and Lecomte R 1988 Design of a high resolution positron emission tomograph using solid state scintellation detectors *IEEE Trans. Nucl. Sci.* **35**(1) 685-90

Carson R E, Daube-Witherspoon M E and Green M V 1988 A method for post-injection PET transmission measurements with a rotating source *J. Nucl. Med.* **29** 1558-67

Casey M E and Hoffman E J 1986 Quantitation in positron emission computed tomography 7. A technique to reduce noise in accidental coincidence measurements and coincidence efficiency calibration *J. Comput. Assist. Tomogr.* **10** 845-50

Cavailloles F, Morvan D, Boudet F *et al* 1987 Factor analysis of dynamic structures as an aid for vesicoureteral reflux diagnosis *Contrib. Nephrol.* **56** 238-42

Chan B, Bergström M, Palmer M R *et al* 1983 Scatter distribution in transmission measurements with positron emission tomography *J. Comput. Assist. Tomogr.* **10**(2) 296-301

Chatziioannou A and Dahlbom M 1996 Detailed investigation of transmission and emission data smoothing protocols and their effects on emission images *IEEE Trans. Nucl. Sci.* **43** 290-4

Cherry S R, Shao Y, Silverman R W *et al* 1996 Micropet: a high resolution PET tomograph for imaging small animals *IEEE Nucl. Sci. Symp. & Med. Imag. Conf. Rec.* (to be published)

Cho Z H and Farukhi M R 1978 Bismuth germanate as a potential scintillator in positron cameras *J. Nucl. Med.* **19** 840-4

Cutler P D, Cherry S R, Hoffman E J *et al* 1992 Design features and performance of a PET system for animal research *J. Nucl. Med.* **33** 595-604

Cutler P D and Hoffman E J 1993 Limitations of a dual energy scatter correction technique results in 2D and 3D acquisitions from two commercial PET systems (Abstract) *J. Nucl. Med.* **34** 136P

Daghighian F, Lovelock DM, Eshaghian B *et al* 1994 Design considerations of an animal PET scanner utilizing LSO scintillators and position sensitive PMTs. *IEEE Nucl. Sci Symp & Med Imag conf rec* **3** 1343-6

Dahlbom M and Hoffman E J 1987 Problems in signal-to-noise ratio for attenuation correction in high resolution PET *IEEE Trans. Nucl. Sci.* **34** 288-93

Dahlbom M and Hoffman EJ 1988 An evaluation of a two-dimensional array detector for high resolution PET *IEEE Trans. Med. Imag.* **7** 264-72

Defrise M, Townsend D W, Bailey D *et al* 1991 A normalization technique for 3D PET data *Phys. Med. Biol.* **36** 939-52

deKemp R and Nahmias C 1994 Attenuation correction in PET using single photon transmission measurement *Med. Phys.* **21** 771-8

Di Paola R, Bazin J P, Aubry F *et al* 1982 Handling of dynamic sequences in nuclear medicine *IEEE Trans. Nucl. Sci.* **29** 1310-21

Derenzo S E 1986a Recent developments in position emission tomography instrumentation *SPIE* **671** 232-243

Derenzo S E 1986b Mathematical removal of positron range blurring in high resolution tomography *IEEE Trans. Nucl. Sci.* **NS-33** 565-9

Derenzo S E, Moses W W, Huesman R H and Budinger T F 1993 Critical instrumentation issues for resolution smaller than 2 mm, high sensitivity brain PET *Quantification of brain function, tracer kinetics and image analysis in brain PET* ed Uemura K *et al* (Elsevier Science Publishers B. V.) pp 25-37

DeVito R P, Hamill J J 1991 Determination of weighting functions for energy-weighted acquisition *J. Nucl. Med.* **32** 343-9

East L V, Philips R L and Strong A R 1982 A fresh approach to NaI scintillation detector spectrum analysis *Nucl. Instrum. Methods* **193** 147-55

Egbert S D and May R S 1980 An integral-transport method for Compton-scatter correction in emission computed tomogrphy *IEEE Trans. Nucl. Sci.* **NS-27** 543-8

Eriksson L, Dahlbom M and Widén L 1990 Positron emission tomography - a new technique for studies of the central nervous system *J. Microscopy* **157** 305-33

Evans R D 1955 *The Atomic Nucleus* (Florida: Malabar)

Floyd C E, Jaszczak R J, Harris C C and Coleman R E 1984 Energy and spatial distribution of multiple order Compton scatter in SPECT a Monte Carlo investigation *Phys. Med. Biol.* **29** 1217-30

Floyd C E, Jaszczak R J, Coleman R E 1985a Inverse Monte Carlo a unified reconstruction algorithm for SPECT *IEEE Trans. Nucl. Sci.* **32** 779-85

Floyd C E, Jaszczak R J, Harris C C *et al* 1985b Monte Carlo evaluation of Compton scatter subtraction in single photon emission computed tomogrphy *Med. Phys.* **12** 776-8

Floyd C E, Jaszczak R J, Greer K L and Coleman R E 1985c Deconvolution of Compton scatter in SPECT *J. Nucl. Med.* **26** 403-8

Frey E C, Tsui B M W 1990 Parameterization of the scatter response function in SPECT imaging using Monte Carlo simulation *IEEE Trans. Nucl. Sci.* **37** 642-6

------- 1993 A practical method for incorporating scatter in a projector-backprojector for accurate scatter compensation in SPECT *IEEE Trans. Nucl. Sci.* **37** 642-6

Frey E C, Ju Z W and Tsui B M W 1993 A fast projector-backprojector pair modeling the asymmetric, spatially varying scatter response function for scatter compensation in SPECT imaging *IEEE Trans. Nucl. Sci.* **40** 1192-7

Gagnon D, Todd-Pokropek A, Arsenault A and Dupras G 1989 Introduction to holospectral imaging in nuclear medicine for scatter subtraction *IEEE Trans. Med. Imag.* **8** 245-50

Gardner S F, Green J A, Bendnarczyk E M *et al* 1992 Principles and clinical applications of positron emission tomography *AJHP* **49** 1499-506

Gilardi M C, Bettinardi V, Todd-Pokropek A *et al* 1988 Assessment and comparison of three scatter correction techniques in single photon emission computed tomography *J. Nucl. Med.* **29** 1971-9

Gilland D R, Jaszczak R J, Greer K L and Coleman R E 1991 Quantitative SPECT reconstruction of iodine-123 data *J. Nucl Med.* **32** 527-33

Grootoonk S, Spinks T J, Jones T *et al* 1991 Correction for scatter using a dual energy window technique with a tomograph operated without septa *IEEE Nucl. Sci. Symp. & Med. Imag. Conf. Rec.* **3** 1569-73

Halama J R, Henkin R E and Friend L E 1988 Gamma camera radionuclide images improved contrast with energy-weighted acquisition *Radiology* **169** 533-8

Harrison R L, Haynor D R and Lewellen T K 1991 Dual energy window scatter corrections for positron emission tomography *IEEE Nucl. Sci. Symp. & Med. Imag. Conf. Rec.* **3** 1700-4

Harrison R L, Haynor D R and Lewellen T K 1992 Limitations of energy-based scatter correction for quantitative PET *IEEE Nucl. Sci. Symp. & Med. Imag. Conf. Rec.* **2** 862-4

Henze E, Huang S C, Ratib O *et al* 1983 Measurements of regional tissue and blood-pool tracer concentrations from serial tomographic images of the heart *J. Nucl. Med.* **24** 987-96

Héon M, Carrier C, Cadorette J *et al* 1993 A stationary sampling scheme for multilayer positron tomographs *IEEE Trans. Med. Imag.* **12** 293-8

Hoffman E J and Phelps E M 1986 *Positron emission tomography principles and quantitation* (Raven Press) pp 237-286

Hoffman E J, Guerrero T M, Germano G *et al* 1989 PET system calibrations and corrections for quantitative and spatially accurate images *IEEE Trans. Nucl. Sci.* **36** 1108-12

Hotelling H 1933 Analysis of a complex of statistical variables into principal components *J. Educ. Psychol.* **24** 417-41, 498-520

Hoverath H, Kuebler W K, Ostertag H J *et al* 1993 Scatter correction in the transaxial slices of a whole-body positron emission tomograph *Phys. Med. Biol.* **38** 717-28

Huang S C, Hoffman E J, Phelps M E and Kuhl D E 1979 Quantitation in positron emission computed tomography 2. Effects of inaccurate attenuation correction *J. Comput. Assist. Tomogr.* **3** 804-14

Huang S C, Carson R E, Phelps M E *et al* 1981 A boundary method for attenuation in positron emission computed tomography *J. Nucl. Med.* **22** 627-37

Huang S C and Phelps M E 1986 Principles of tracer kinetic modeling in positron emission tomography and autoradiography *Positron emission tomography and autoradiography: principles and applications for the brain and heart* ed Phelps M E, Mazziotta J C and Schelbert H R (Raven Press) 287-346

Ingvar M, Eriksson L, Rogers GA *et al* 1991 Rapid feasibility studies of tracers for positron emission tomography high-resolution PET in small animals with kinetic analyss *J. Cereb. Blood Flow Metab.* **11** 926-31

Jaszczak R J, Greer K L, Floyd C E *et al* 1984 Improved SPECT quantification using compensation for scattered photons *J. Nucl. Med.* **25**(8) 893-900

Jaszczak R J, Hoffman D C, DeVito R P 1991 Variance propagation for SPECT with energy-weighted acquisition *IEEE Trans. Nucl. Sci.* **38** 739-47

Johns H E and Cunningham J R 1983 *The physics of radiology.* (Illinois: Springfield) Chapter 5

Jolliffe I T 1986 *Principal component analysis* (New York: Springer-Verlag)

Jones T, Tilsley D W O, Wilson C B J H *et al* 1992 Positron emission tomography for tumor assessment *NMR in Biomedicine* **5** 265-9

King M A, Penney B C, Glick S J 1988 An image-dependent Metz filter for nuclear medicine images *J. Nucl. Med.* **29** 1980-9

King M A, Coleman M, Penney B C and Glick S J 1991 Activity quantitation in SPECT: a study of prereconstruction Metz filtering and use of the scatter degradatiion factor *Med. Phys.* **18** 184-9

King M A, Hademenos G J, Glick S J 1992 A dual-photopeak window method for scatter correction *J. Nucl. Med.* **33** 605-12

King P H, Hubner K, Gibbs W and Holloway E 1981 Noise identification and removal in positron imaging systems *IEEE Trans. Nucl. Sci.* **NS-28** 148-151

Koeppe R A and Hutchins G D 1992 Instrumentation for positron emission tomography tomographs and data processing and display systems *Seminars in Nucl. Med.* **XXII** 162-81

Koral K F, Clinthorne N H, Rogers W L 1986 Improving emission computed tomography quantification by Compton-scatter rejection through offset windows *Nucl Instrum Methods Phys Res* **A24** 610-614.

Koral K F, Wang X, Rogers W L *et al* 1988 SPECT Compton-scattering correction by analysis of energy spectra *J. Nucl. Med.* **29** 195-202

Kouris *et al* 1982 Coincidence time window, rign sampling and attenuation problem in positron emission tomography *Nucl. Instrum. Methods* **193** 215-222

Lecomte R, Schmitt D and Lamoureux G 1984 Geometry study of a high resolution PET detection system using small detectors *IEEE Trans. Nucl. Sci.* **31** 556-61

Lecomte R, Carrier C and Martel C 1989 Status of BGO-avalanche photodiode detectors for spectroscopic and timing measurements *Nucl. Instrum. Methods Phys. Res. A* **278** 585-97

Lecomte R, Cadorette J, Jouan A *et al* 1990 High resolution positron emission tomography with a prototype camera based on solid state scintillation detectors *IEEE Trans. Nucl. Sci.* **37** 805-11

Lecomte R, Martel C and Cadorette J 1991 Study of the resolution performance of an array of discrete detectors with independent readouts for positron emission tomography *IEEE Trans. Med. Imag.* **10** 347-57

Lecomte R, Bentourkia M, Msaki P *et al* 1992 Potentials of multispectral acquisition in positron emission tomography *IEEE Nucl. Sci. Symp. & Med. Imag. Conf. Rec.* **2** 856-8

Lecomte R, Cadorette J, Rodrigue S *et al* 1993 A PET camera simulator with multispectral data acquisition capabilities *IEEE Trans. Nucl. Sci.* **40** 1067-74

Lecomte R, Cadorette J, Richard P *et al* 1994 Design and engineering aspects of a high resolution positron tomograph for small animal imaging *IEEE Trans. Nucl. Sci.* **41** 1446-52

Lecomte R, Cadorette R, Rodrigue S *et al* 1996 Initial results from the Sherbrooke avalanche photodiode PET scanner *IEEE Trans. Nucl. Sci.* **43** 1952-7

Lewitt R M, Muehllehner G and Karp J 1994 Three-dimensional image reconstruction for PET by multi-slice rebinning and axial image filtering *Phys. Med. Biol.* **39** 321-39

Links J M, Loats H L, Loats P E *et al* 1990 Simultanous resolution recovery and noise reduction in positron tomography by Fourier filtering of 2-D projection data *J. Nucl. Med.* 30 863P

Links J M, Leal J P, Mueller-Gaertner H W and Wagner H N 1992 Improved positron emission tomography quantitation by Fourier-based restoration filtering *Eur. J. Nucl. Med.* **19** 925-32

Ljungberg M and Strand S E 1990a Attenuation correction in SPECT based on transmission studies and Monte Carlo simulations of buildup functions *J. Nucl. Med.* **31** 290-94

Ljungberg M, Msaki P and Strand S E 1990b Comparison of dual-window and convolution scatter correction techniques using the Monte Carlo method *Phys. Med. Biol.* **35** 1099-110

Ljungberg M and Strand S E 1990 Scatter and attenuation correction in SPECT using density maps and Monte Carlo simulated scatter functions *J. Nucl. Med.* **31** 1560-7

Logan K W and McFarland W D 1992 Single photon scatter compensation by photopeak energy distribution analysis *IEEE Trans. Med. Imag.* **11** 161-4

Maeda J and Murata K 1986 Local-statistics algorithm for smoothing noisy images with low signal-to-noise ratio *Optics Communications* **59** 11-6

Mandelkern M A 1995 Nuclear techniques for medical imaging positron emission tomography *Annu. Rev. Nucl. Part. Sci.* **45** 205-54

Maor D, Berlad G, Chrem Y *et al* 1991 Klein-Nishina based energy factors for Compton free imaging (CFI) (abstract) *J. Nucl. Med.* **32** 1000

Mardia K V, Kent J T and Bibby J M 1979 *Multivariate Analysis* (New York: Academic)

Marriott C, Cadorette J, Lecomte R *et al* 1994 High resolution PET imaging and quantitation of pharmaceutical biodistributions in a small animal using avalanche photodiode detectors *J. Nucl. Med.* **35** 1390-7

Mas J, Hannequin P, Ben Younes R *et al* 1990 Correction de la diffusion Compton en imagerie isotopique par analyse factorielle sous contraintes *Innov. Tech. Biol. Med.* **11** 641-55

Mascarenhas NDA, Furuie SS and Portal ALS 1993 Global projection estimation methods for the tomographic reconstruction of images with Poisson noise *IEEE Trans. Nucl. Sci.* **40** 2008-13

Mazoyer B M, Roos M S and Huesman R H 1985 Dead time correction and counting statistics for positron tomography *Phys. Med. Biol.* **30** 385-99

Meikle S R, Dahlbom M and Cherry S R 1993 Attenuation correction using count-limited transmission data in positron emission tomography. *J Nucl Med* **34** 143-150.

Melcher C L and Schweitzer J S 1992 A promising new scintillator: cerium-doped lutetium oxyorthosilicate *Nucl. Instr. and Meth. in Phys. Res.* **A314** 212-14

Michel C, Bol A, Spinks TJ *et al* 1991 Assessment of response function in two PET scanners w/o interplane septa *IEEE Trans. Med. Imag.* **10** 240-248

Moses W W, Derenxo S E, Nutt R *et al* 1993 Performance of a PET detector module utilizing an array of silicon photodiodes to identify the crystal of interaction *IEEE Trans. Nucl. Sci.* **NS-40** 1036-40

Msaki P, Axelsson B, Dahl C M and Larsson S A 1987 Generalized scatter correction method in SPECT using point scatter distribution functions *J. Nucl. Med.* **28** 1861-9

Msaki P, Bentourkia M, Cadorette J *et al* 1993a Normalization of multispectral data in positron emission tomography *Phys. Med. Biol.* **38** 1745-60

Msaki P, Erlandsson K, Svensson L and Nolstedt L 1993b The convolution scatter subtraction hypothesis and its validity domain in radioisotope imaging *Phys. Med. Biol.* **38** 1359-70

Msaki P, Yao R, Cadorette J, Bentourkia M and Lecomte R 1994 Methods for reducing statistical noise of multispectral data in positron emission tomography *Conf. Rec. 16th Annual International Conference IEEE Engineering in Medicine and Biology Society* part **1** pp 632-3

Msaki P, Bentourkia and Lecomte R 1996 Scatter degradation and correction models for high-resolution PET (Editorial) *J. Nucl. Med.* **37** 2047-9

Mukai T, Links J M, Douglass K H and Wagner H N 1988 Scatter correction in SPECT using non-uniform attenuation data *Phys. Med. Biol.* **33** 1129-40

Murthy K, Thompson C J, Weinberg I N and Mako F M 1994 Measurement of the coincidence response of very thin BGO crystals *IEEE Trans. Nucl. Sci.* **41** 1430-5

Naudé H, Aswegen A V, Herbst C P *et al* 1996 A monte carlo evaluation of the channel ratio scatter correction method *Phys. Med. Biol.* **41** 1059-66

Ollinger J M, Johns G C and Burney M T 1992 Model based scatter correction in three dimensions *IEEE Nucl. Sci. Symp. & Med. Imag. Conf. Rec.* **2** 1249-51

Ollinger J M 1994 Detector efficiency and Compton scatter in fully 3D PET *IEEE Nucl. Sci. Symp. & Med. Imag. Conf. Rec.* **2** 1280-4

Paans A M J, Rosenqvist G, Holte S *et al* 1989 Scatter fraction: measurement and correction *Eur. J. Nucl. Med.* **15** 727-31

Palmer MR, Rogers JG, Bergström M, Beddoes MP and Pate BD 1986 Transmission profile filtering for positron emission tomography *IEEE Trans. Nucl. Sci.* **33** 478-81

Paranjape RB, Rabie TF and Rangayyan RM 1994 Image restoration by adaptive-neighborhood noise subtraction *Applied Optics* **33** 2861-9

Pearson K 1901 On lines and planes of closest fit to systems of points in psace *Phil. Mag.* (6) **2** 559-572

Phelps M E, Hoffman E J, Huang S C *et al* 1979 Design considerations in positron computed tomography (PCT) *IEEE Trans. Nucl. Sci.* **NS-26** 2746-51

Phelps M E, Mazziotta J C and Schelbert H R 1986 *Positron emission tomography and autoradiography: principls and applications for the brain and the heart* (New York: Raven Press)

Prati P, Lanza P, Corvisiero P *et al* 1993 Verification of the integral transformation of the projections technique for scatter correction in positron tomography *Eur. J. Nucl. Med.* **20** 255-9

Precision Visual, Inc. 1991 *PV-Wave command language technical reference manual*

Press W H, Flannery B P, Teukolsky S A *et al* 1990 *Numerical recipes in C the art of scientific computing* (Cambridge: Cambridge University Press)

Pretorius P H, van Rensburg A J, van Aswegen A *et al* 1993 The channel ratio method of scatter correction for radionuclide image quantitation *J. Nucl. Med.* **34** 330-5

Sashin D, Spinks TJ, Grootoonk S and Jones T 1992 Smoothing of random data to reduce noise in 3D PET *Conf. Rec. 1992 IEEE Nuclear Science Symposium & Medical Imaging Conference*, vol. 2 973-5.

Schmitt D, Lecomte R and LeBel E 1986 Wedge-shaped scintillation crystals for positron emission tomography *J. Nucl. Med.* **27** 99-104

Seber G A F 1984 *Multivariate observations* (John Wiley & Sons)

Shao L and Karp J S 1991 Cross-plane scattering correction point source deconvolution in PET *IEEE Trans. Med. Imag.* **10** 234-9

Shao L, Karp J S and Countryman P 1994a Practical considerations of the Wiener filtering technique on projection data for PET *IEEE Trans. Nucl. Sci.* **41** 1560-5

Shao L Freifelder R and Karp J S 1994b Triple energy window scatter correction technique in PET *IEEE Trans. Med. Imag.* **13** 641-8

Shao Y, Cherry S R, Siegel S and Silverman R W 1996 A study of inter-crystal scatter in small scintillator arrays for PET *IEEE Trans. Nucl. Sci.* **43** 1938-44

Snyder D L, Miller M I, Thomas L J and Pllitte D G 1987 Noise and edge artifacts in maximum-likelihood reconstrctions for emission tomography *IEEE Trans. Med. Imag.* **MI-6** 228-38

Sossi V, Barney J S, Oakes T R and Ruth T J 1995 Comparison of energy window choice and parameter implementation in dual energy window scatter correction performance in 3D PET *IEEE Nucl. Sci. Symp. & Med. Imag. conf. rec.* **2** 1060-3

Sorensen J A and Phelps M E 1987 *Physics in Nuclear Medicine* (Second Edition) (Philadephia: W.B. Saunders Company)

Spinks T J, Jones T, Bailey D L *et al* 1992 Physical performance of a positron tomograph for brain imaging with retractable spta *Phys. Med. Biol.* **37** 1637-55

Stazyk M W, Sossi V, Ruckley K R and Ruth T J 1994 Normalization measurement in septa-less PET scanners *J. Nucl. Med.* **35**(5) 41P

Stearns CW and Wack DC 1993 A noise equivalent counts approach to transmission imaging and source design *IEEE Trans. Med. Imag.* **12** 287-92

Sweet W H 1951 Uses of nuclear disintergrations in the diagnosis and treatment of brain tumors *N. Engl. J. Med.* **245** 875-80

Ter-Pogossian M M, Raichle M E and Sobel B E 1980 Positron-emission tomography *Scientific Am.* **243**(4) 171-81

Thompson C J 1988 The effect of collimation on scatter fraction in multislice PET *IEEE Trans. Nucl. Sci.* **35** 598-602

Thompson C J, Ranger N T and Evans A C 1989 Simultaneous transmission and emission scans in positron emission tomography *IEEE Trans. Nucl. Sci.* **36** 1011-15

Thompson C J, Moreno-Cantou J and Picard Y 1992 PETSIM: Monte Carlo simulation of all sensitivity and resolution parameters of cylindrical positron imaging system *Phys. Med. Biol.* **37** 731-49

Thompson C J and Picard Y 1993 Two new strategies to increase the signal to noise ratio in positron volume imaging *IEEE Trans. Nucl. Sci.* **40** 956-61

Townsend D, Spinks T, Jones A *et al* 1989 Three dimensional reconstruction of PET data from a multi-ring camera *IEEE Trans. Nucl. Sci.* **36** 1056-65

Waggett D J and Wilson B C 1978 Improvement ofscanner performance by subtraction of Compton scattering correction by analysis of energy spectra *Br. J. Radiol.* **51** 1004-10

Wang X and Koral K F 1992 A regularized deconvolution-fitting methods for Compton-scatter correction in SPECT *IEEE Trans. Med. Imag.* **11** 351-60

Watanabe M, Uchida H, Okada H *et al* 1992 A high resolution PET for animal studies *IEEE Trans. Med. Imag.* **11** 577-80

Waterson C C, Newport D and Casey M E 1995 A single scatter simulation technique for scatter correction in 3D PET *1995 International Meeting on fully three-dimensional image reconstruction in radiology and nuclear medicine*

Watson C C 1996 A technique for measuring the energy response of a PET tomograph using a compact scattering source *IEEE Nucl. Sci. Symp. & Med. Imag. Conf. Rec.*

Wienhard K, Eriksson L, Grootoonk S *et al* 1992 Performance evaluation of the positron scatter ECAT EXACT *J. Comput. Assist. Tomogr.* **16** 804-13

Wilson D and Tsui B M W 1993 Noise properties of filtered-backprojection and ML-EM reconstructed emission tomographic images *IEEE Trans. Nucl. Sci.* **40** 1198

Wilkinson J H 1965 *The algebraic eigenvalue prolem.* (Oxford: Oxford University Press)

Wu R K and Siegel J A 1984 Absolute quantification of radioactivity using the buildup factor *Med. Phys.* **11** 189-92

Yao R, Msaki P, Bentourkia M and Lecomte R 1996a Effects of energy space smoothing and projection space normalization on multispectral PET image quality *IEEE Trans. Nucl. Sci.* **43** 1988-94

Yao R, Bentourkia M and Lecomte R 1996b Study of multispectral convolution scatter correction in high resolution PET *IEEE Nucl. Sci. Symp. & Med. Imag. Conf. Rec.*